

In-situ studies of protein-resistant
self-assembling monolayers

Dissertation

zur Erlangung des Grades eines Doktors

der Naturwissenschaften

der Mathematisch-Naturwissenschaftlichen Fakultät

der Eberhard-Karls-Universität zu Tübingen

vorgelegt von

Stefan Zorn

aus: Plauen

2010

Tag der mündlichen Prüfung: 1. Oktober 2010

Dekan: Prof. Dr. Wolfgang Rosenstiel

1. Berichtstatter: Prof. Dr. Frank Schreiber
2. Berichtstatter: Prof. Dr. Günter Gauglitz

Meinen Eltern

Contents

1	Deutsche Zusammenfassung	v
1.1	Motivation	v
1.2	Ergebnisse	vi
1.2.1	Berechnung und Optimierung der PMIRRAS-Signalstärke	vi
1.2.2	Normierung und Basislinienkorrektur für PMIRRAS-Spektren	vii
1.2.3	Messung von PMIRRAS-Spektren auf dielektrischen Substraten	viii
1.2.4	Konformationsänderung von EG ₆ OMe-SAMs während ihres Wachstums	ix
1.2.5	Langzeitstabilität von EG ₆ OMe-SAMs und Degradation	x
1.2.6	Verhalten von EG ₆ OMe SAMs bei erhöhten Temperaturen	xi
1.3	Schlussfolgerungen	xii
2	Introduction and literature review	1
2.1	General Introduction	1
2.2	Motivation and scope of the thesis	2
2.3	Literature review	3
2.3.1	Self assembling monolayers	3
2.3.2	<i>Poly</i> (ethylene-glycol) SAMs	4
2.3.3	<i>Oligo</i> (ethylene-glycol) SAMs	4
2.3.4	Crystalline structure of alkanethiols on Au(111)	6
2.3.5	Oxidative Degradation of <i>Poly</i> (ethylene-glycols)	7
2.3.6	Protein interaction with surfaces	8
2.4	<i>In-situ</i> measurements – motivation and challenge	11
3	Experimental methods	13

CONTENTS

3.1	Sample preparation	13
3.1.1	Angle dependence of PMIRRAS signal strength	13
3.1.2	Measurement of specific protein binding on PEG SAMs on dielectric substrates	14
3.1.2.1	Thin film deposition	14
3.1.2.2	Wet chemistry	14
3.1.3	Measurement of specific protein binding on PEG SAMs on dielectric substrates as a function of PEG chain length	15
3.1.3.1	Materials	15
3.1.3.2	Wet chemistry	15
3.1.4	<i>In-situ</i> growth, temperature behaviour and stability of OEG SAMs	16
3.1.5	Surface Plasmon resonance measurements	16
3.1.6	In-plane grazing incidence X-ray scattering	16
3.2	Optical calculation and simulation	16
3.3	Infrared spectroscopy	21
3.3.1	Theoretical background	21
3.3.2	Fourier transform infrared spectrometry	23
3.3.3	Infrared transmission measurements	26
3.3.4	Infrared reflection absorption spectroscopy (IRRAS)	27
3.3.5	Polarisation modulation infrared spectroscopy (PMIRRAS)	30
3.3.6	Experimental normalization procedure with additional polarizer	32
3.3.7	Experimental setup	33
3.3.7.1	Liquid cell	34
3.3.7.2	Temperature controllable liquid cell	36
3.3.8	Data processing and analysis	37
3.3.8.1	Baseline correction	37
3.3.8.2	Baseline correction for the angle dependent PMIRRAS measurements	38
3.3.9	Data analysis program multifit	38
3.3.10	Plot and normalization of the fit results	39
3.4	X-ray reflectivity	40
3.4.1	Theoretical background	40
3.4.2	Experimental setup	42

3.5	Grazing incidence X-ray diffraction	43
3.5.1	General remarks	43
3.5.2	Experimental setup	44
3.6	Spectroscopic ellipsometry	45
3.6.1	Experimental Setup	46
3.7	Surface plasmon resonance	46
3.7.1	Experimental setup	47
3.8	Complementary techniques	47
3.8.1	Electron microscopy	48
3.8.2	X-ray photoelectron spectroscopy (XPS)	48
4	Results and discussion	49
4.1	Technical development of the PMIRRAS method	50
4.1.1	Simulation and optimization of PMIRRAS signal strength	50
4.1.1.1	Mathematical framework and implementation	50
4.1.1.2	Optimization of experimental parameters	51
4.1.1.3	Comparison of calculations and experiments	54
4.1.1.4	Conclusion	57
4.1.2	Estimation of the water layer thickness for <i>in-situ</i> measurements	57
4.1.2.1	Conclusion	60
4.1.3	Normalization of spectra	60
4.1.3.1	Conclusion	63
4.1.4	Specific protein binding on PEG-Biotin functionalized surfaces	63
4.1.4.1	Characterization of Si-Ti-SiO _x substrates	63
4.1.4.2	Simulations of PM-IRRAS on Si-Ti-SiO _x substrates	67
4.1.4.3	PM-IRRAS measurements on Si-Ti-SiO _x substrates	68
4.1.4.4	Surface loading as a function of PEG length	71
4.1.4.5	Transmission measurements of PEG2000 SAMs on silicon substrates	72
4.1.4.6	Conclusion	72
4.2	<i>In-situ</i> growth of <i>oligo</i> (ethylene glycol)	73
4.2.1	Identification and significance of the vibrational modes	73
4.2.2	Evolution of the modes	74

CONTENTS

4.2.3	Interaction with water	78
4.2.4	Conclusion	81
4.3	Conformation as a function of surface coverage	81
4.3.1	SPR measurements	81
4.3.2	Mixed SAMs	83
4.3.3	Conclusion	86
4.4	Stability of OEG-SAMs	88
4.4.1	Degradation with UV-light	88
4.4.2	Stability in air	90
4.4.3	Degeneration effects in air at 60 °C	94
4.4.4	Stability during repeated drying and reimmersion	99
4.4.5	Stability in solution over long time period	101
4.4.6	Conclusion	103
4.5	Temperature behaviour of EG ₆ OMe SAMs in solution	103
4.5.1	Temperature range up to 40 °C	104
4.5.2	Temperature range above 40 °C	107
4.5.3	Temperature dependence for different coverage	107
4.5.4	Measurements in air	108
4.5.5	Reversibility of conformational change in air	109
4.5.6	In plane structure measured with grazing incidence X-ray scattering	110
4.5.7	Conclusion	113
5	Outlook	114
6	Conclusion	116
	List of abbreviations	120
	Bibliography	123

Chapter 1

Deutsche Zusammenfassung

1.1 Motivation

Mit Hilfe von Beschichtungen lassen sich die Eigenschaften von Oberflächen maßgeblich beeinflussen, was vielfältige Anwendungen ermöglicht. Aufgrund dieser großen Bedeutung sind zahlreiche Techniken entwickelt worden um dünne Molekülschichten auf Oberflächen aufzubringen: von der Langmuir-Blodgett-Technik, Spincoating und Molekularstrahlepitaxie bis hin zu selbst-aggregierenden Monolagen. Insbesondere selbst-aggregierende Monolagen (SAMs) haben in den letzten Jahren stark an Bedeutung gewonnen [1–6]. SAMs können mit Hilfe von verschiedenen Ankergruppen auf diversen Oberflächen wachsen. Die größte Verbreitung haben SAMs, die mit einer Silangruppe auf Siliziumoxid binden [7] und solche, die mit einer Thiolgruppe an Gold binden [8]. Diese beiden Systeme dienen als Modellsysteme. Aufgrund ihrer wohldefinierten kristallinen Struktur und der vergleichsweise einfachen Kontrolle ihrer chemischen Eigenschaften, wie Hydrophilie, Schichtdicke und Oberflächenladung haben SAMs neue Anwendungsbereiche erschlossen. Sie finden im technischen Bereich Verwendung als Gleitmittel [9] und werden in der Nanolithografie [10] und der molekularen Elektronik [11] eingesetzt. Auch im medizinischen und biologischen Bereich finden SAMs Anwendung. Diese reichen von weichen Unterlagen für auf Oberflächen immobilisierten Biomembranen [12], über Plattformen für spezialisierte Moleküle [13] bis hin zu ihrem wichtigsten Einsatzgebiet: der Verhinderung unspezifischer Proteinadsorption. Dies ermöglicht es Schiffsrümpfe gegen unerwünschten Algenbewuchs zu schützen [14] oder Zellwachstum auf Implantaten zu verhindern [15]. In Kombination mit Molekülgruppen, die selektiv binden [16], und mit Techniken zur Bestimmung der Oberflächenbedeckung wie Oberflächenplasmonresonanz [13], reflektometrische Interferenzspektroskopie [17] und Quarzmikrowägung [18], können Sensorelemente zum Nachweis von spezifischen Proteinen konstruiert werden.

Um die proteinresistenten Eigenschaften von SAMs und damit auch das Signal-Rausch-Verhältnis von Biosensoren zu verbessern ist es wichtig den Mechanismus der Proteinresistenz zu verstehen. Außerdem kann das Verständnis der zugrunde liegenden Zusammen-

hänge Rückschlüsse auf die Wechselwirkung von Biomolekülen untereinander ermöglichen. Es hat sich herausgestellt, dass nicht nur die hydrophilen Eigenschaften der Endgruppe des SAMs für dessen Proteinresistenz entscheidend sind, sondern auch eine neutrale Gesamtladung sowie das Vorhandensein von polaren Gruppen und die Verfügbarkeit von Protonendonatoren [19]. Insbesondere spielt die Einlagerung und Bindung von Wassermolekülen in der Ethylenglycol-Domäne und an ihrer Grenzfläche zur Wasserschicht eine große Rolle [20–22].

Im Mittelpunkt der vorliegenden Arbeit steht die Untersuchung des Hexaethylenglykolterminierten Thiols $\text{HS}(\text{CH}_2)_{11}(\text{OCH}_2\text{CH}_2)_6\text{OMe}$ (EG_6OMe) in wässriger Umgebung (*in-situ*). Es wird der Einfluss des Wassers auf das Wachstum der Monolagen, ihre Struktur, ihr Temperaturverhalten und ihre Langzeitstabilität untersucht um damit Erkenntnisse über die Art der Wechselwirkung mit Wassermolekülen zu gewinnen. Besonders geeignet ist hierfür Polarisations-Modulations-Infrarot-Reflexions-Absorptions-Spektroskopie (PMIRRAS), es liefert strukturelle Informationen und hat im Zusammenspiel mit geeigneten Messzellen für dünne Wasserschichten ein exzellentes Signal-Rausch-Verhältnis [22], was die Technik sensitiv für sehr kleine Änderungen im untersuchten System macht.

1.2 Ergebnisse

Für das Verständnis des Mechanismus der Proteinresistenz anhand des Modellsystems EG_6OMe spielt die Wechselwirkung mit Wassermolekülen und deren Bindung im OEG Bereich eine besondere Rolle. Ein Weg um diese Wechselwirkung mit Wasser besser zu verstehen ist die Änderung von Parametern des SAMs wie Temperatur und Packungsdichte und die Beobachtung der Strukturänderung des SAMs in Lösung. Solche *in-situ*-Messungen sind wesentlich komplexer als einfache Messungen an der Luft und erfordern eine Optimierung des experimentellen Aufbaus und der Datenauswertung.

Der erste Abschnitt des Ergebnisteils behandelt die Berechnung der Signalstärke von Infrarotspektren in Abhängigkeit der Wasserschichtdicke und deren experimentelle Überprüfung. Weiterhin wird gezeigt, wie PMIRRAS-Spektren normiert werden können, wie die Basislinie korrigiert werden kann und wie Moleküle auf dielektrischen Substraten mit PMIRRAS gemessen werden können. Es folgt die Beschreibung der Konformationsänderung von SAMs während des Wachstums in Lösung, der Einfluss der Wechselwirkung mit Wasser auf die SAM-Struktur, die Langzeitstabilität von SAMs in Lösung und an der Luft sowie Effekte bei wiederholter Reimmersion. Abschließend wird der Einfluss von erhöhter Temperatur auf die Struktur von SAMs untersucht.

1.2.1 Berechnung und Optimierung der PMIRRAS-Signalstärke

Mit Hilfe der Fresnel-Gleichungen ist es möglich die Reflektions- und Transmissionskoeffizienten beim Übergang von elektromagnetischen Wellen zwischen zwei Medien zu berech-

nen. Mit Hilfe des Matrixformalismus von Hansen lässt sich für jeden Übergang eine Matrix erstellen [23, 24]. Im Falle eines Mehrschichtsystems erhält man durch Multiplikation dieser Matrizen eine Gesamtübergangsmatrix, aus der sich Reflexion und Transmission des Gesamtsystems berechnen lassen. Der Algorithmus wurde in ein Programm in der Software IgorPro implementiert, das es ermöglicht, diese Berechnungen für verschiedene Schichtsysteme, Winkel und Wasserschichtdicken durchzuführen. Die Berechnungen wurden über einen Winkelbereich von $45 - 82,5^\circ$ mit PMIRRAS-Messungen experimentell überprüft. Dazu wurde die Signalintensität der C-O-C-Streckschwingung eines EG₆OMe Thiol-SAMs auf Gold an Luft und in einer *in-situ* Zelle unter Wasser gemessen. Bis auf einen konstanten Vorfaktor stimmen die Ergebnisse von Theorie und Experiment überein [23]. Dies macht das Programm zu einem wichtigen Werkzeug um optimale Messbedingungen zu bestimmen. Um unter *in-situ* Bedingungen mit PMIRRAS gemessene Daten quantitativ miteinander vergleichen zu können, ist die Bestimmung der Wasserschichtdicke über der Probe entscheidend. Dies ist mit Ellipsometriemessungen möglich sowie mit IRRAS-Messungen und anschließendem Vergleich mit simulierten IRRAS-Reflexionsspektren. Es konnte gezeigt werden, dass das im PMIRRAS-Spektrum enthaltene Signal ($\frac{1}{2}(R_s + R_p)$) im Spektralbereich von $4000 \text{ cm}^{-1} - 2800 \text{ cm}^{-1}$ auch mit dem berechneten Reflexionssignal übereinstimmt. Somit kann direkt aus dem normalen Spektrum die Schichtdicke bestimmt werden. Besonders interessant ist dies für Echtzeitmessungen, die keine Zeit für Probenwechsel zwischen den Messungen lassen.

1.2.2 Normierung und Basislinienkorrektur für PMIRRAS-Spektren

Mit einer von Buffeteau et al. [25] entwickelten Kalibrationsmethode kann man mit Hilfe von Referenzspektren in zwei Schritten ein PMIRRAS-Signal in ein IRRAS-Signal umwandeln. Im ersten Schritt werden zwei Referenzspektren aufgenommen, indem hinter der Probe ein zusätzlicher Polarisator eingesetzt wird. Dieser wird so eingestellt, dass nur p-polarisierte bzw. s-polarisierte Strahlung passieren kann. Mittels dieser beiden Referenzspektren wird der zweite Term der Besselfunktion (J_2) aus dem Spektrum entfernt. Im zweiten Teil der Methode wird das erhaltene Spektrum mit Hilfe eines ebenfalls korrigierten Spektrums vom blanken Substrat normiert. Es konnte gezeigt werden, dass die Referenzspektren für verschiedene metallische Substrate nicht unterscheidbar sind und somit nicht für jede Probe neu gemessen werden müssen. Dies reduziert die Anzahl der nötigen Messungen von sechs pro Spektrum auf zwei. Es muss lediglich zusätzlich zur normalen Messung ein PMIRRAS-Spektrum vom blanken Substrat gemessen werden, da dieses für den zweiten Schritt der Kalibrierung benötigt wird. Diese Methode kann eingesetzt werden, wenn Spektren auf verschiedenen Substraten miteinander quantitativ verglichen werden sollen. Für die Bestimmung der Modenpositionen bringt sie nur den Vorteil der Basislinienkorrektur.

Diese Kalibrationsmethode ist leider nur für Messungen an Luft anwendbar. Für *in-*

situ Messungen wurden deshalb mit Hilfe von optischen Rechnungen (siehe Abschnitt 1.2.1) Bedingungen gesucht, bei denen die Signalstärke trotz Änderung der Wasserschichtdicke konstant bleibt. Dies kann mit einem Einfallswinkel von 70° erreicht werden. Bei diesem Winkel bleibt die Signalstärke für Wasserschichtdicken von $1 \mu\text{m} - 2 \mu\text{m}$ nahezu konstant [23]. Die Basislinienkorrektur erfolgt reproduzierbar und automatisiert mit einem Programm unter IgorPro bei dem die Basislinie durch feste Stützpunkte interpoliert wird. Diese Stützpunkte werden außerhalb der Absorptionsmoden gewählt und es wird sichergestellt, dass keine Moden durch die Korrektur verändert werden.

1.2.3 Messung von PMIRRAS-Spektren auf dielektrischen Substraten

Silane sind neben Thiolen die gebräuchlichste Ankergruppe von SAMs. Am häufigsten werden Siliziumoxidoberflächen mit ihnen funktionalisiert [3]. PMIRRAS beruht auf den Auswahlregeln für die elektrische Feldstärke für s- und p-polarisiertes Licht an leitenden Oberflächen. Für s-polarisiertes Licht verschwindet das elektrische Feld nahe der Oberfläche. Für p-polarisiertes Licht wird es verstärkt. Streng genommen gilt dies nur für metallische Oberflächen, was PMIRRAS-Messungen auf dielektrischen Substraten erschwert [26]. Wenn die Dicke der dielektrischen Schicht im Vergleich zur Ausdehnung des evaneszenten Feldes über der Metalloberfläche (für mittleres IR im Bereich von 100 nm) klein ist, wird die Auswahlregel nicht signifikant gestört. Eine 200 nm dicke Titanschicht wurde auf Siliziumsubstrate gesputtert, gefolgt von einer 5-10 nm dicken Siliziumoxidschicht. Die Rechnungen und die Experimente zeigten übereinstimmend, dass die Signalstärke durch die dünne Siliziumoxidschicht nur geringfügig abgeschwächt wird. Durch die Si-O-Si-Streckschwingung des Siliziumoxids [27] in der dünnen Oberflächenschicht wird der Bereich von 1000 cm^{-1} bis 1250 cm^{-1} verdeckt. Es ist jedoch möglich anhand der Wippschwingung bei 1350 cm^{-1} und der Deformationsschwingung bei 1463 cm^{-1} PEG2000 SAMs zu identifizieren sowie anhand der Amid-I-Bande (1664 cm^{-1}) und der Amid-II-Bande (1540 cm^{-1}) Proteinabsorption festzustellen. Mit Hilfe von biotinierten PEG-Molekülen konnten wir feststellen, dass unspezifische Proteinadsorption verhindert wird, Streptavidin jedoch spezifisch bindet. Dies zeigt, dass die Methode gut geeignet ist um PMIRRAS-Spektren von Molekülen auf dielektrischen Schichten aufzunehmen. In Zusammenarbeit mit N. Schweizer (AK Gauklitz Institut für Physikalische und Theoretische Chemie Tübingen) konnte auch gezeigt werden, dass die Beladung von PEG-Biotin Molekülen mit Streptavidin von der Kettenlänge der PEG-Moleküle abhängig ist. Während PEG900 und PEG2000 in etwa eine gleiche Beladung haben, nimmt diese für PEG6000 stark ab. Dieses Ergebnis wurde auch mit RifS und AFM Messungen bestätigt [17]. Es wird angenommen, dass PEG6000-SAMs aufgrund der großen Kettenlänge kollabieren und die Biotinmoleküle am Kettenende, quasi im Inneren des SAMs, verborgen und für Streptavidin nicht zugänglich sind. Es ist auch möglich Infrarotspektren dünner Molekülschichten auf Siliziumsubstraten per Transmission zu messen. Es stellte sich jedoch heraus, dass das Signal-Rausch-Verhältnis für diese Messungen sig-

nifikant schlechter ist als für die vorgestellte Methode mit PMIRRAS. Die charakteristischen Wipp- und Deformations-Schwingungsmoden von PEG2000 sind gerade noch über dem Rauschlevel messbar. Zusätzlich muss für Transmissionsmessungen zur Normierung des Spektrums das blanke Substrat gemessen werden. Jede Messung benötigt lange Warte- und Messzeiten. Dies unterstreicht die Bedeutung der Möglichkeit PMIRRAS-Messungen auf dielektrischen Substraten durchzuführen.

1.2.4 Konformationsänderung von EG₆OMe-SAMs während ihres Wachstums

Einen Schwerpunkt dieser Arbeit bildet die Beobachtung der Konformationsänderung von EG₆OMe-SAMs während ihres Wachstums in wässriger Umgebung und deren Interpretation. Der Anteil der OEG-Moleküle in helikaler Konformation kann anhand der C-O-C-Streckschwingung bei 1116 cm⁻¹, der EG-CH₂-Drehschwingung bei 1244 cm⁻¹ und der EG-Wippschwingung bei 1350 cm⁻¹ beobachtet werden. Der Anteil der Moleküle in all-*trans*-Konfiguration ist sichtbar im hochfrequenten Teil der C-O-C-Streckschwingung bei 1144 cm⁻¹ und im niederfrequenten Teil der EG-Wippschwingung bei 1325 cm⁻¹. Die CH₃-Schaukelschwingung bei 1200 cm⁻¹ ist unabhängig von der Konformation und kann somit zur Abschätzung der Oberflächenbedeckung genutzt werden. Dieser Zusammenhang konnte mit SPR-Experimenten und unter Verwendung gemischter SAMs bestätigt werden. Während dem beobachteten Zeitraum ändert sich die Konformation des SAMs von gemischt helikal-all-*trans* zu überwiegend helikal. Die Änderung der Modenintensität folgt einem einfachen exponentiellen Zusammenhang. Außerdem kommt es während dem Wachstumsprozess zu einer Rotverschiebung der Modenposition und einer Verringerung der relativen Breite der Moden. Beides deutet auf eine Verbesserung des kristallinen Charakters hin.

Um die Änderung der Moden richtig zu interpretieren, ist es wichtig die Wechselwirkung zwischen OEG-Bereich und Wassermolekülen zu verstehen. Dies wird besonders deutlich, vergleicht man die SAM-Struktur in wässriger Umgebung mit der SAM-Struktur an Luft. Während für mittlere Oberflächenbedeckungen in beiden Umgebungen eine eher amorphe Struktur vorliegt, haben bei größerer Oberflächenbedeckung OEG-SAMs an der Luft eine überwiegend helikale Konformation und kristalline Struktur, während ihre Struktur in Wasser starke amorphe Züge aufweist. Dies deutet auf eine Wechselwirkung mit Wassermolekülen hin, die in den OEG-Bereich des SAMs eingedrungen sind. Dies deckt sich mit den Beobachtungen von SFG-Untersuchungen [28, 29] an OEG-SAMs. Für sehr hohe Oberflächenbedeckungen hingegen unterscheiden sich die Spektren in Wasser und an Luft kaum, was ein starkes Indiz dafür ist, dass Wasser aufgrund der dichten Oberflächenbedeckung und hohen Kristallinität des SAMs nicht in den OEG-Bereich eindringen kann [21, 30] und somit nicht mit den Ethylenglykol-Einheiten wechselwirken kann. Vanderah et al. beobachteten, dass SAMs mit sehr langen Wachstumszeiten eine perfekte helikale Struktur einnahmen, jedoch ihre proteinresistenten Eigenschaften ver-

lieren [31]. Gemeinsam betrachtet legen diese Beobachtungen nahe, dass die Fähigkeit Wassermoleküle im OEG-Bereich zu binden und die Proteinresistenz von OEG-SAMs miteinander zusammenhängen. Wenn Wasser nicht mehr in die OEG-Einheit eindringen kann und dort gebunden wird, verliert der SAM seine proteinresistenten Eigenschaften.

1.2.5 Langzeitstabilität von EG₆OMe-SAMs und Degradation

Die Konformation von EG₆OMe-Thiol-SAMs ist sehr sensitiv gegenüber kleinen Änderungen. Deshalb ist es wichtig Parameter, die EG₆OMe-SAMs beeinflussen zu identifizieren und systematisch zu untersuchen. Ein erster Punkt hierbei ist die Reinigung der Goldsubstrate. Es ist bekannt, dass Alkan-SAMs keine morphologischen Unterschiede zeigen, wenn man sie auf frisch aufgedampften Substraten wächst oder auf solchen, die schon mit einem SAM bedeckt waren, mit Ozon erzeugendem UV-Licht bestrahlt und danach gründlich in Ethanol gespült wurden [32]. Die vorliegende Arbeit zeigt, dass dies auch für EG₆OMe-SAMs gilt. Ein weiterer wichtiger Punkt ist die Langzeitstabilität von OEG-Thiol-SAMs und die daraus folgenden Änderungen in Konformation und chemischer Zusammensetzung. Es wurde unterschieden zwischen Lagerung in Luft unter Einstrahlung natürlichen Lichts und im Dunkeln sowie im Dunkeln in einem wässrigen Medium. Die SAMs an Luft wurden über 120 Tage beobachtet. Von Langzeituntersuchungen mit langkettigen PEG-Molekülen ist bekannt, dass sie durch thermische Anregung (ab 50 °C) sowie durch photochemische Anregung über radikalische Reaktionen degenerieren [33–35]. Dabei kommt es zur Bildung von Estern und Formiaten, bei letzteren zudem zu einer Abspaltung von der PEG-Kette. Bei Lagerung der SAMs in Luft unter Einstrahlung natürlichen Lichts konnte beobachtet werden, dass die Intensität der Moden, die eine helikale Struktur zeigen ebenso wie die Intensität der CH₃-Schaukel-Schwingung, die die Existenz der CH₃-Gruppe am äußeren Ende des SAMs anzeigt, abnahmen. Währenddessen nahmen die Moden die von den Ester- und Formiat-Abbauprodukten stammen zu. Beide Prozesse folgen einem einfach exponentiellen Zusammenhang mit vergleichbaren Zeitkonstanten. Nach dem Spülen der Substrate mit Ethanol am Ende des Langzeit-Experiments unter Lichteinstrahlung verringerte sich die Intensität aller Absorptionsmoden signifikant. Dies wird darauf zurückgeführt, dass Thiolgruppen durch den UV-Anteil im Licht oxidierten und die zugehörigen Moleküle nur noch auf der Oberfläche physisorbiert waren [32]. Bei Lagerung der SAMs im Dunkeln war der Abbauprozess signifikant langsamer, was darauf hindeutet, dass Licht die maßgebliche Rolle für die Aktivierung des Degradationsprozesses bei Raumtemperatur spielt [34]. Die SAMs unter wässrigen Bedingungen wurden 6 Tage lang in der *in-situ*-Zelle beobachtet. Es wurde keine signifikante Änderung des Absorptionsspektrums festgestellt. Dies lässt auf eine noch bessere SAM-Stabilität schließen als bei Lagerung im Dunkeln. Es wird angenommen, dass dies auf den radikalischen Charakter der Abbaureaktion zurückzuführen ist. In Lösung können Radikale leichter diffundieren und somit dem System entzogen werden [1, 36]. Die hohe Stabilität steht auch in Einklang mit experimentellen Beobachtungen, die zeigen, dass auch nach 28 Tagen in Lösung SAMs ihre proteinresistenten Eigenschaften vollständig behalten [36]. Ein weit-

erer wichtiger Punkt ist der Einfluss von wiederholter Trocknung und Reimmersion von EG₆OMe-SAMs. Es konnte gezeigt werden, dass sich bereits nach einem Spülzyklus mit Ethanol für 3 s und anschließender Trocknung die Intensität der Moden, die die helikale Konformation des SAMs anzeigen, signifikant verringert hat. Nach nur 10 Zyklen hat sich das Spektrum stark verändert und deutet auf einen überwiegend amorphen SAM hin. Das Spülen mit Wasser hat den gleichen Effekt. Langzeituntersuchungen zeigen, dass die Strukturänderung irreversibel ist.

1.2.6 Verhalten von EG₆OMe SAMs bei erhöhten Temperaturen

SAMs werden oft bei höheren Temperaturen als Raumtemperatur eingesetzt. Eine Untersuchung von Änderungen in Konformation und Struktur kann Hinweise auf funktionelle Veränderungen geben. Thiol-SAMs, deren Moleküle sich von EG₆OMe hauptsächlich durch eine zusätzliche Amidgruppe unterscheiden, die sie zusätzlich stabilisieren, wurden von Valiokas et al. im Vakuum bei schrittweise erhöhter Temperatur untersucht [37]. Während sich die Moleküle im SAM bei Raumtemperatur in überwiegend helikaler Konformation befanden, änderte sich ihre Anordnung nach schrittweiser Temperaturerhöhung bis 70 °C zu einer überwiegenden all-*trans*-Konformation, der Prozess war vollständig reversibel. Das Experiment wurde in der vorliegenden Arbeit mit EG₆OMe in wässriger Umgebung wiederholt. Ziel war es den Einfluss von Wassermolekülen auf den Umordnungsprozess zu bestimmen.

Die Temperatur wurde von 25 °C schrittweise um jeweils 5 °C erhöht. Bis zu einer Temperatur von 40 °C kam es zu einer Änderung der Konformation von überwiegend helikal zu gemischt all-*trans* helikal, vergleichbar mit dem Experiment von Valiokas et al. [37]. Während sich die Intensität der entsprechenden Absorptionsbanden änderte, blieben deren Position und Breite nahezu konstant. Die Konformation bei der jeweiligen Temperatur war stark abhängig von der Kristallinität des SAMs bei Zimmertemperatur, die wiederum von der Oberflächenbedeckung abhängt. Eine Verringerung der Temperatur auf die Ausgangstemperatur von 25 °C führte nicht zu einer Regenerierung der ursprünglichen Konformation. Allerdings konnte der Ausgangszustand nach einer Trocknung des SAMs und anschließender Reimmersion fast vollständig wieder hergestellt werden. Das lässt darauf schließen, dass keine Degeneration des SAMs stattgefunden hat. Die Nichtreversibilität zeigt, dass Wassermoleküle, welche im SAM verankert sind, diesen ohne eine treibende Kraft (wie zum Beispiel die Bindung neuer Thiole beim Wachstum) nicht wieder verlassen. Dies ist ein weiteres Indiz für die starke Wechselwirkung und Stabilisierung von Wassermolekülen, die im OEG-Bereich des SAMs gebunden sind.

Bei Erhöhung der Temperatur über 40 °C kam es zu einer sprunghaften Änderung der relativen Position der Absorptionsmoden des OEG-Bereichs. Dies betraf sowohl die Moden, die der all-*trans*-Konformation zugeordnet sind als auch die Moden, die mit der helikalen Konformation verknüpft sind. Es kam zu einer weiteren Verschiebung und zu einem höheren Anteil an Molekülen in all-*trans*-Konformation. Je nach Kristallinität

des gemessenen SAMs bei 25 °C, löste sich bei verschiedenen Temperaturen die kristalline Struktur auf. Die unterschiedliche Übergangstemperatur - als Funktion der Oberflächenbedeckung - ist im Einklang mit Messungen des Temperaturverhaltens von Alkan-SAMs [3]. Der Prozess ist nicht reversibel. Weder durch Verringerung der Temperatur auf 25 °C noch durch Trocknung des SAMs und anschließende Reimmersion ließ sich der Ausgangszustand des SAMs wieder herstellen. Die Beobachtungen lassen auf Degenerationseffekte der SAM-Moleküle schließen. Dies stimmt mit experimentellen Ergebnissen für lange PEG-Ketten überein. Diese degenerieren bei 50 °C [33]. Bei den Messungen in wässriger Umgebung lassen sich keine Abbauprodukte nachweisen. Dies kann daran liegen, dass sich diese vom SAM lösen und in die Lösung diffundieren. Vergleichsmessungen des Temperaturverhaltens an Luft zeigen Absorptionsmoden, die Ester- und Formiatgruppen zugeordnet werden können. Die Messungen zeigen ebenfalls eine Amorphisierung des SAMs im Anschluss an die gemischte helikale und *all-trans* Konformation anstelle eines Übergangs zu einer überwiegenden *all-trans*-Konformation. Die Unterschiede zu den Messungen von Valiokas [37], die im Vakuum mit amidstabilisierten OEG-Molekülen durchgeführt worden sind, sind ein Zusammenspiel aus folgenden Faktoren: der geringeren Stabilität der EG₆OMe-Moleküle, der Interaktion in Lösung mit Wassermolekülen und bei Temperaturen über 40 °C der Degeneration der SAM-Moleküle.

1.3 Schlussfolgerungen

Es wurde gezeigt, wie sich durch Simulationen ideale Messbedingungen bestimmen lassen. Des Weiteren wurde ein Verfahren vorgestellt, mit dem PMIRRAS-Messungen reproduzierbar ausgewertet und normiert werden können. Zudem wurde ein Substrat entwickelt, mit dessen Hilfe Moleküle mit PMIRRAS auf dünnen dielektrischen Schichten gemessen werden können. Dessen praktische Anwendbarkeit wurde anhand spezifischer Proteinabsorption mit dem PEG-Biotin-System gezeigt.

Der Schwerpunkt der Arbeit lag auf der Untersuchung von EG₆OMe-Thiol-SAMs, ihrem Wachstum in Lösung sowie ihrem Temperatur- und Langzeitverhalten. Dabei stand die Wechselwirkung der Thiolmoleküle mit den sie umgebenden Wassermolekülen im Mittelpunkt. Es konnte gezeigt werden, dass das Eindringen von Wassermolekülen in den SAM und damit die Stärke der gegenseitigen Wechselwirkung mit der Oberflächenbedeckung des SAMs in Verbindung steht. Der Zusammenhang zwischen SAM-Kristallinität und Proteinresistenz deutet darauf hin, dass SAMs, die so gut kristallin geordnet sind, dass kein Wasser eindringen kann, auch nicht in der Lage sind Wasser in ihrem Inneren zu binden und somit ihre proteinresistenten Eigenschaften verlieren. Durch Temperaturerhöhung kann die kristalline Struktur gelockert werden und Wassermoleküle können in den OEG-Bereich eindringen. Die Bindung der Wassermoleküle ist so stark, dass sie sich ohne treibende Kraft nicht wieder aus dem SAM lösen lassen. Durch Temperaturerhöhung über 40 °C bzw. durch den Einfluss von Licht kommt es zu einer Degeneration von EG₆OMe-SAMs. Abbauprodukte sind Ester und Formiate. Dies kann durch Anwen-

dung bei geringeren Temperaturen und durch den Schutz vor Lichteinwirkung verhindert werden. In wässriger Umgebung sind OEG-SAMs besonders stabil, jedoch ist der OEG-Bereich des SAMs empfindlich gegen mehrmalige Trocknung und Reimmersion. Diese Erkenntnisse können dabei helfen den Mechanismus der Proteinresistenz von OEG-SAMs besser zu verstehen und den Umgang mit SAMs reproduzierbarer zu machen.

Chapter 2

Introduction and literature review

2.1 General Introduction

Customized surface properties are very important for a variety of applications. In the last decades various techniques have been used to modulate surfaces for specific applications, including the Langmuir-Blodgett technique, spin-coating, molecular beam epitaxy and self-assembled monolayers (SAMs). The importance of the utilization of surfaces functionalized with SAMs increased enormously over the last years [1–6]. Their spontaneous organization into well ordered crystalline structures allows systematical changes of the chemical properties of surfaces and therefore an enormous bandwidth of applications. SAMs have become important tools in the field of engineering as lubricants [9], for nanolithography [10] and molecular electronics [11, 38]. Additionally, they are used in the biomedical field as tethering layers for biomembranes [12] and platform for specialized molecules. Most important are SAMs, which are able to passivate surfaces against unspecific protein binding [39]. They can be used as coating for ships inhibiting alga growth [14] and in medical applications hindering the irreversible adsorption of proteins with surfaces. In combination with specific headgroups protein resistant SAMs are also able to bind specifically proteins, DNA and other biomolecules, which is useful for biosensors [40] based on techniques like surface plasmon resonance (SPR), quartz microbalance (QCM) or reflectometric interference spectroscopy (RIfS).

SAMs can be distinguished by their anchoring groups. In addition to the model systems of silane based SAMs first introduced by Sagiv [7] and thiol SAMs introduced by Nuzzo and Allara [8], there are also anchor groups enabling the functionalization of silicon, titanium oxide, zinc oxide, indium tin oxide and diamond with SAMs. Another way to classify SAMs is their functional end group exhibiting the greatest impact of the SAMs surface properties.

With their ability to customize reproducibly surface properties like hydrophilicity, surface charge and surface softness, SAMs are ideal tools to investigate the response to biological

samples like proteins [2], tissue [15], biomembranes [12] and DNA [13]. Knowledge about the surface interaction in controlled systems allows to characterize the same interaction in more complex systems, such as cell-cell interaction or antigen antibody interaction. Moreover, surfaces can be patterned with SAMs, allowing selective placement of proteins and cells [41]. An popular way for this patterning is nano imprinting [42].

In order to improve the biofouling properties of SAMs, the signal to noise ratio of bio-sensing methods and the contrast of bio-patterning techniques, it is important to understand the mechanisms leading to protein resistance. This mechanistic understanding may shed light the interaction of biomolecules. Ethylene glycol SAMs have been established as a model system for these investigations. It has turned out that the surface hydrophilicity of the SAM is important for protein resistance, but also a neutral net charge as well as the presence of polar groups and the availability of proton donors [19, 43]. The ability of the SAM to bind water molecules at their surface and in their interior plays a critical role as well. An detailed overview of the current state of research can be found in Sec. 2.3.2 and Sec. 2.3.3 of the literature review.

To characterize SAMs a variety of methods have been used. There are methods sensitive to surface coverage as SPR [13], RfS [17], X-ray reflectivity [44] and QCM [18], which can be used under aqueous conditions and provide information about the surface coverage in real time. Their drawback, however, is the lack of structural information. Also spectroscopic methods like X-ray photoelectron spectroscopy (XPS) [45], sum frequency generation (SFG) [28] and reflection absorption infrared spectroscopy (IRRAS) [46] have been used extensively to characterize SAMs. However, while SFG has a weak signal to noise ratio for measurements in solution, XPS can only applied in vacuum IRRAS is a well suited technique for the identification of molecules and the interaction with their environment. Due to the strong absorption of water in the fingerprint region it is challenging to measure molecules in aqueous environment (*in-situ*). This problem can be overcome by the polarisation modulation infrared reflection absorption spectroscopy (PMIRRAS) technique in combination with a thin liquid layer *in-situ* cell allowing to perform *in-situ* measurements with a very high signal-to-noise ratio [47].

2.2 Motivation and scope of the thesis

This thesis is focused on *in-situ* studies exploiting the benefits of the PMIRRAS technique. With its help, the interaction of SAMs with water molecules can be studied under various conditions in terms of surface coverage (during SAM growth) and temperature without interfering with the setup during the measurement of the real-time series.

One goal of this work is the measurement of the growth of *oligo*(ethylene glycol) (OEG) SAMs in solution in real time and the investigation of the influence of the surrounding solvent on the SAM structure as a function of surface coverage. Furthermore, the structural changes at elevated temperatures and the longtime stability of OEG SAMs in solution

should be elucidated. Moreover, the influence of repeated reimmersion on the SAMs structure should be explained and the *in-situ* results regarding longtime and temperature behaviour are compared with measurements in air. In order to get reliable and high quality data an optimization of the PMIRRAS setup for real-time *in-situ* measurements was performed. The focus of the methodological efforts was 1) On the development and experimental validation of a program to simulate the PMIRRAS signal strength and calculating optimal experimental conditions. Moreover, on their control during the real-time measurements. 2) On the programming of routines for reproducible handling of large data sets and automated baseline correction. 3) On the design of suitable sample cells enabling reproducible measurements with high quality data.

The thesis is organized in the following way: In Sec. 2.3 the current research status in terms of SAMs, protein interaction with surfaces, mechanistic views about prevention of biofouling and waveoptics is discussed, as well as the necessity and benefits of *in-situ* measurements. In Chap. 3 a brief description of the methods used in this thesis is presented, focusing on the PMIRRAS method, its development and the automatizing of the related data analysis. In Chap. 4 the results are presented and discussed, starting with Sec. 4.1 which deals with the optimization of the PMIRRAS setup, including the calculation of ideal conditions for PMIRRAS measurements, especially in water. Section 4.1.3 covers the normalization of the spectra and Sec. 4.1.4 measurement with PMIRRAS on dielectric substrates. The second part of Chap. 4 focuses on measurements of OEG SAMs. It is starting with their growth and reordering in solution and the influence of the solvent on their structure in Sec. 4.2. Moreover, SAM degeneration effects are investigated and compared regarding their storage in solution or in air as well as their exposure to light and to heat (Sec. 4.4). The results and discussion part concludes with the study of the structural and conformational behaviour of SAMs at elevated temperature in Sec. 4.5. Finally, an outlook for future experiments is given in Chap. 5 and the results are summarized in Chap. 6.

2.3 Literature review

2.3.1 Self assembling monolayers

Self assembling monolayers (SAMs) are molecules which are able to bind and order on a surface independently from solution or gas phase. There are numerous publications, which cannot all be reviewed here. It is referred to several reviews [1–5, 40, 48–51]. Normally molecules forming a SAM consist of three parts, a anchor group binding to the substrate, a linker group connecting anchor- and head group. Very common are alkane chain linkers and a head group on top of the molecule determining the SAMs surface properties. There are various anchor groups, suitable for different substrates and purposes. Prevalent is also the silane group, introduced by Sagiv in 1980 [7], being used as so-called model system. It can form covalent siloxane bonds on silicon oxide and related structures.

Another widespread anchor group used as model system is the thiol group, forming very stable bonds on coinage metals, such as gold, silver and copper. Introduced by Nuzzo and Allara in 1983 [8], thiol bonds have a lateral mobility to some degree, which helps to form a regular surface pattern, which is systematically investigated for alkanethiols. On Au(111), they adopt a $(\sqrt{3} \times \sqrt{3})R30^\circ$ structure with a possible superlattice termed “c(4x2)”, corresponding to a $\sim 5\text{\AA}$ spacing in between the molecules and an area per molecule of 21.6\AA^2 . In siloxanes, the hexagonal structure is distorted for sterical and mobility reasons, octadecyltrichlorosilane takes an area per molecule of 20.2\AA^2 [52].

2.3.2 *Poly(ethylene-glycol) SAMs*

Poly(ethylene-glycol) (PEG) SAMs can be used to render surfaces resistant against un-specific protein adsorption. This makes them a valuable tool for biomedical applications. In 1990, Jeon and coworkers proposed a mechanism for the repulsion of proteins from surfaces covered with PEG [53]. They considered the free energies of steric repulsion, hydrophobic interactions and van der Waals attraction. Proteins diffusing into the PEG water interface are attracted by van der Waals interactions. When penetrating the PEG chains, a repulsive force, initiated by compression of the PEG chains, is taking effect on the proteins. Additionally, there is an attractive van der Waals interaction between the hydrophobic substrate and the protein. For long PEG chains and a high surface coverage, this attractive van der Waals interactions decrease, enhancing the protein repellent properties of the SAM.

By coupling of special head groups to PEG chains, it is possible to bind specifically proteins. Stressing the prevention of un-specific bio fouling and specific binding, the surface can be used for a selective binding, which is very helpful for various biomedical applications e.g. the construction of labs on a chip, analysing liquids for specific proteins and tailored binding of cells to surfaces. A common system uses biotin linkers binding specifically to streptavidin [16].

2.3.3 *Oligo(ethylene-glycol) SAMs*

Whitesides and co-workers [54,55] showed that not only *poly* (ethylene glycols) are able to render surfaces resistant against un-specific protein adsorption but also short chained *oligo* (ethylene glycols) (OEGs). They can also be used as a spacer for tethering various groups enabling specific binding of proteins [56] or DNA [13] and so be applicable for biosensors. They are also useful as a supporting layer of lipid films, which are able to retain their crystalline-liquid structure due to the soft underlayer [12], which makes them a valuable tool in biotechnology. Due to their smaller length they have a higher surface coverage and strongly interact with each other. Therefore, they form better defined and smoother surfaces than *poly* (ethylene glycols). However, due to the short chains and highly ordered conformation, the proposed mechanism of Jeon et al. [53] cannot be applied to explain

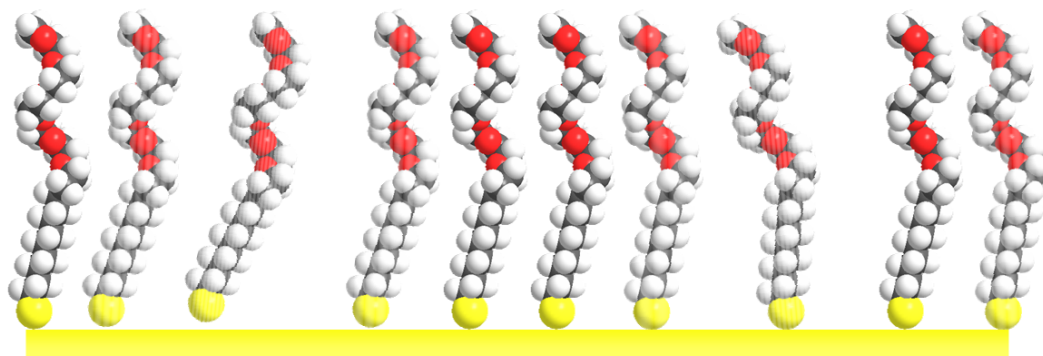


Figure 2.3.1: Schematic of the protein resistant hexa(ethylene glycol) SAM. The molecules consist of a thiol anchor group, an alkane spacer and the OEG moiety. The molecules adopt on Au substrates a helical conformation after an adequate immersion time.

their protein resistant properties. Owing to their importance, there has been extensive work in order to understand the underlying mechanisms of the protein resistance and the structural behaviour of OEGs. It was shown that OEGs containing three ethylene glycol (EG) units adopt different conformations on Ag and Au substrates due to different lattice spacing which allows control of their protein resistance [46]. Theoretical work suggested that a perfect helical conformation is most favourable for SAMs with 6 EG units (compare Fig. 2.3.1), that small distortions, however, increase the energy of the system only slightly [57]. By increasing the temperature it is possible to change the structure of OEG SAMs with 6 EG units from a predominant helical conformation to an all-trans conformation [37]. Vanderah et al. [31] showed that the protein resistance of SAMs with 6 EG units depends on the surface coverage due to its impact on the conformation and crystallinity of the SAM and concluded that perfect ordered helical SAMs with 6 EG units with full surface coverage are not completely resistant against protein adsorption (see also Ref. [21]), while such with about 80-90% surface coverage are. Generally, there are many conflicting reports concerning the order and protein resistance of OEG SAMs, implying that the SAMs structure is very sensitive towards different preparation conditions e.g. regarding surfactant concentration and growth time [31, 45, 58]. A deeper understanding of the growth process may shed light on this and may lead to a higher reproducibility of SAM growth. Another important point in understanding the structural behaviour and protein resistant properties of OEG SAMs is their interaction with the water molecules. In an *in-situ* PMIRRAS study with OEG SAMs containing 3 EG units, Skoda et al. [47] showed that there is a red-shift in the C-O-C stretching region of SAMs in solution with respect to spectra in air, which indicates an interaction with water. Also sum frequency generation (SFG) studies showed that there is a distortion of the structure of SAMs with 3 EG units [28] and 6 EG units [29] due to the interaction with water. Wang et al. reported that not only the upper EG units are affected but also interior ones and that their conformational freedom is increased by the interaction with water. Wang et al. [20]

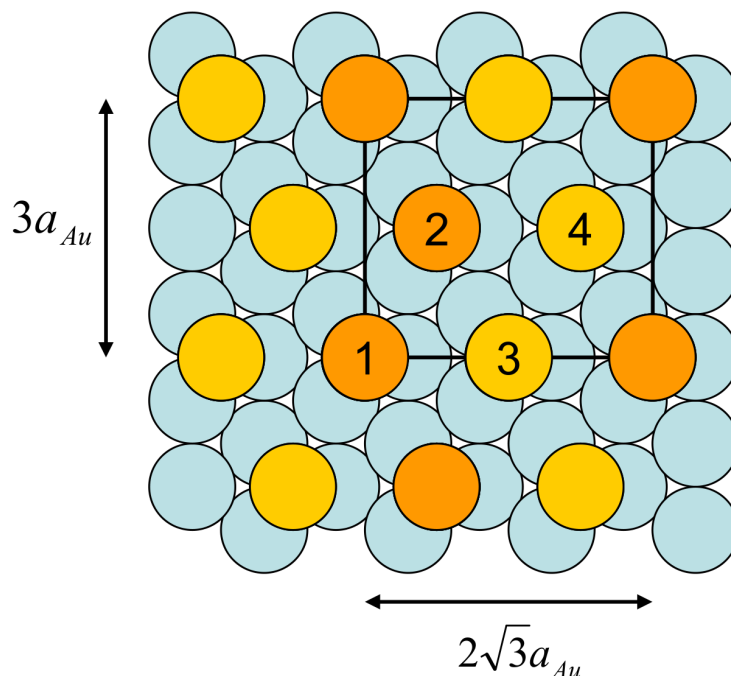


Figure 2.3.2: Scheme of the crystalline structure of alkane thiols on a Au(111) surface, the figure is adapted from Ref. [3]. The thiol molecules adopt an $(\sqrt{3} \times \sqrt{3})R30^\circ$ structure on the (111) surface. Infrared results indicated, that there are two inequivalent thiol chain's per unit cell. Therefore, a $c(4 \times 2)$ superlattice is proposed, taking a unit cell containing 2 different pairs of thiol molecules. as indicated in the scheme.

gave a possible explanation of this strong perturbation using density functional theory (DFT) calculations. In air, perfect helical structures are most favourable and especially conformers with gauche rotations of opposite directions around neighbouring EG units are most unfavourable due to the capability forming intramolecular hydrogen bonds. Based on the formation of intra- and intermolecular hydrogen bridged structures with water molecules, these conformers with gauche defects are more favourable than perfect helical structures, in an aqueous environment. This leads to amorphization if water can penetrate the EG layer [28, 29].

2.3.4 Crystalline structure of alkanethiols on Au(111)

In the following section a brief overview of the in-plane structure of alkane thiols on Au(111) substrates is given. The Au(111) surface is the lowest energy surface and therefore this orientation is preferred for thin evaporated Au films as the substrates used in this work. As mentioned in Sec. 2.3.1, alkane thiols on Au(111) adopt a $(\sqrt{3} \times \sqrt{3})R30^\circ$ structure, with a $\sim 5\text{\AA}$ spacing in between the thiol molecules [59–61]. Further, the alkane molecules are in all-*trans* conformation and tilted by $\sim 34^\circ$ towards the surface

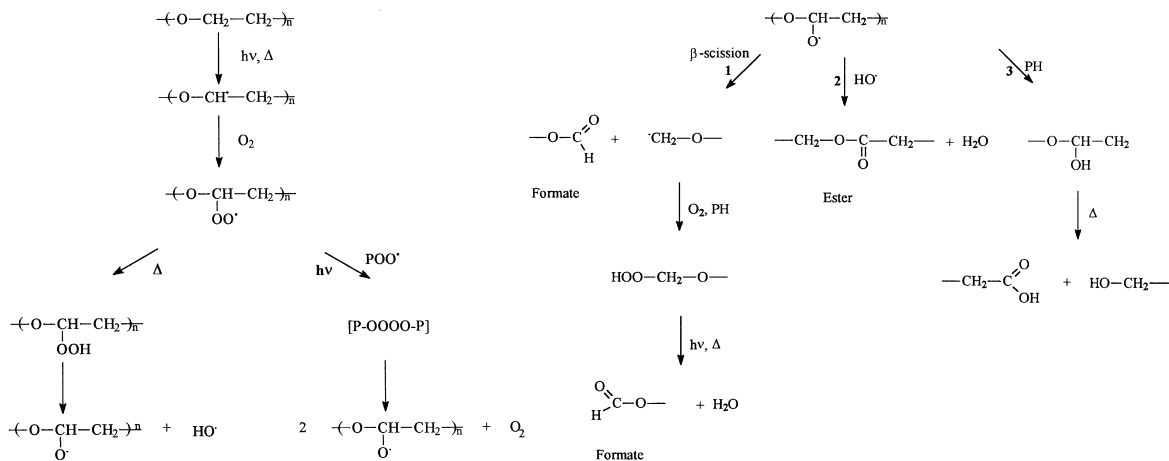


Figure 2.3.3: Scheme of the mechanism of the oxidation of *poly*(ethylene glycols). On the left hand side pathways for the formation of alkoxy radicals from ethylene-glycol molecules activated by heat and light are shown and on the right hand side the reaction pathways of alkoxy radicals to esters and formates. The scheme is taken from Morlat et al. [33].

normal [62]. Splitting of the methylene (CH_2) scissors mode at 1467 cm^{-1} in the IR spectra of cooled down alkane SAMs suggested that there are two inequivalent chains per unit cell. This could be confirmed by grazing incidence X-ray diffraction (GIXD) measurements [63], further it could be elucidated that 2 pairs of these inequivalent thiol molecules form a $c(4 \times 2)$ superlattice, as shown in Fig. 2.3.2. For a detailed overview see Ref. [3].

2.3.5 Oxidative Degradation of *Poly*(ethylene-glycols)

An important issue in the application of chemical compounds is their stability during usage and storage. Due to their chemical structure, PEGs are very sensitive towards oxidation. Based on their widespread application as detergents especially in nutrition and daily chemicals, there is a great demand in the investigation of their oxidation, its mechanism and products. It is well known that the oxidation of *poly* ethers involves radical reactions [34]. They can be triggered by radiation, elevated temperature, chemicals and mechanical stress. The major reasons for the degradation of *Poly*(ethylene glycols) during application are light and heat exposure. The distribution of end products and the exact mechanism of oxidation caused by these effectors is different, however for both the degradation is following the subsequent scheme.

In a first step, activated by heat or light, a hydrogen radical is abstracted from a carbon atom in α -position to an oxygen atom in the PEG molecule, leaving a radical, compare to Fig. 2.3.3. It further reacts with oxygen forming a peroxy radical, which is then converted to a hydroperoxide. By thermal or photochemical activation, a hydroxy radical is abstracted and an alkoxy radical is formed [33, 34]. For light induced oxidation, an alter-

native mechanism is proposed. Two peroxy radicals recombine to an unstable tetroxide intermediate, which dissociates in two alkoxy radicals and an oxygen molecule [33].

The alkoxy radicals are mainly transformed into formates and terminal radicals by β -scission, compare to Fig. 2.3.3. The radicals can further react to primary hydroperoxides which decompose to formates and water. Besides β -scission, a cage reaction of alkoxy radicals with hydroxy radicals can occur, leading to ester functions. A third way is a cage reaction of the alkoxy radical leading to the formation of a thermally unstable hemiacetal, which decomposes into alcohols and carboxylic acids [33].

A quantitative examination of the composition of molecules after the degeneration reveals the rate of oxidation and the preferred reaction pathway. It turned out that formates and esters are the main products. Their distribution depends on how the oxidation is activated. A photochemical activation leads to a ratio of formates and esters of 5 to 1, whereas thermal activation yields an equal distribution [33]. A possible reason for this different behaviour is that more hydroxy radicals are present in thermally induced oxidation, since they are formed during the reaction from hydroperoxides to alkoxy radicals. The reaction of these radicals lead to ester functions [33], compare Fig. 2.3.3.

2.3.6 Protein interaction with surfaces

A tremendous number of applications in bio related science involves interactions of proteins with surfaces. Surfaces in narrower sense as in the case of biosensors detecting specific proteins [40], functionalized surfaces preventing biofouling [54] and implants or in wider sense surfaces which are themselves complex compositions of biomolecules as in case of the interaction and incorporation of proteins in cell membranes [64] or cell-cell interactions [65]. For a dealing with those interactions it is useful to have a deeper understanding of protein structure, especially concerning the physical properties of protein surfaces and interaction potentials. Proteins are complex biopolymers and one can distinguish four levels of order, primary, secondary, tertiary and quaternary structure. The primary structure is the sequence of amino acids attached to each other by peptide bonds. The amino acid building blocks can be classified by their chemical properties, they can be rather hydrophobic nonpolar or hydrophilic polar as well as containing positive and negatively charged groups. The secondary structure depicts the organisation of the lined up amino acids into structures stabilized by hydrogen bonds as alpha helices, beta-sheets or random coils. These elements are combined to the three dimensional protein tertiary structure. Protein subunits can assemble and form the so-called quaternary structure, a prominent example is hemoglobin consisting of four myoglobin subunits. Due to the composition of numerous amino acids, containing different groups concerning polarity and charge, proteins are amphiphilic macromolecules whose properties depends strongly on the properties of the surrounding solvent.

Protein interaction in solution can be roughly described with the Derjaguin, Landau, Verwey and Overbeek theory (DLVO-theory), quantifying electrostatic and van der Waals

forces. Forces induced by hydrogen bridges formed between polar molecules are important as well, especially the ones from water molecules, which are the reason for hydrophobic interactions.

Electrostatic forces in proteins are generated from ionizable sites in amino acids, laying near the protein surface. In the following paragraph the electrostatic potential of a protein seen as a charged colloid and a planar surface with a homogeneous charge is estimated [66]. With the help of the Boltzmann equation one can describe the electrostatic potential ϕ^i in a protein:

$$\nabla^2 \phi^i = -\rho^i / \epsilon^i \quad (2.3.1)$$

Here ρ^i is the charge distribution and ϵ^i the dielectric permittivity in the protein. The charge distribution ρ^i can be written as the sum of the charges q_k located at the ionized amino acids at the position x_k :

$$\rho^i = \sum_k q_k \delta(x - x_k) \quad (2.3.2)$$

For an electrolyte with equally charged ions the exterior potential is described by a linearized Poisson-Boltzmann equation:

$$\nabla^2 \phi^e = \kappa^2 \phi^e \quad (2.3.3)$$

Here $\kappa^2 = 2e^2 z^2 \rho^\infty / \epsilon^e kT$, where e is the electronic charge, z the valency, k the Boltzmann constant, T the temperature and ρ^∞ the concentration of the electrolyte in the bulk. The boundary condition on the planar surface is a constant charge density, giving the following normal potential gradient σ in direction of the unit vector n perpendicular to the surface in outwards direction:

$$\sigma = -\epsilon^e \frac{\partial \Phi^e}{\partial n} \quad (2.3.4)$$

For a continuous transition at the dielectric boundary in between electrolyte and protein, the following boundary conditions have to be fulfilled:

$$\Phi^i = \Phi^e, \quad \epsilon^i \frac{\partial \Phi^i}{\partial n} = \epsilon^e \frac{\partial \Phi^e}{\partial n} \quad (2.3.5)$$

With the help of these equations the potential can be calculated numerically and from the potential the free energy F of the double layer system can be calculated:

$$F = \frac{1}{2} \int_{\partial P} \sigma \Phi^e dA + \frac{1}{2} \sum_{k=1}^n q_k \Phi^i(x_k) \quad (2.3.6)$$

The planar charged surface is represented by ∂P . Finally the change in free energy can be computed with this equation for a protein going from solution in the vicinity of the surface.

The second important contribution comes from the van der Waals Interactions, it is attractive in most of the cases. Compared to the electrostatic interaction the van der Waals interaction is very short ranged due to its arising from dipole-dipole interaction. For two bodies with the volumes V_1 and V_2 , the energy contribution of the Hamaker potential is defined as [67]:

$$\Delta F = -\frac{A_{12}}{\pi^2} \int_{V_1} \int_{V_2} \frac{1}{r_{12}^6} dV_1 dV_2$$

Assuming the protein as a sphere and the surface as a infinite plane the change in energy contribution ΔF can be calculated to [67]:

$$\Delta F_{sphere/plane} = -\frac{A_{123}}{6} \left[\frac{R}{z} + \frac{R}{2R+z} + \ln\left(\frac{z}{2R+z}\right) \right] \quad (2.3.7)$$

The Hamaker constant A_{123} , dependent on the polarizability and the number density of atoms in the media describes the interaction of compounds 1 and 2 in medium 3, can be derived from the pairwise Hamaker constants A_{12} , A_{13} and A_{23} .

The third major contribution to the interaction forces, the hydrophobic effect, cannot be calculated straight forward. It appears in mixtures of hydrophilic and hydrophobic components. Water molecules are strongly interacting via hydrogen bridges. If a particle with a polar surface is immersed in water, also hydrogen brides are formed. However, if a body with a non-planar surface is dissolved, it is not able to form hydrogen bridges with water molecules, resulting in an entropic cost. This cost is decreasing with the non-polar surface exposed to water, resulting in an aggregation of the non-polar components. For amphiphilic molecules such as proteins or lipids, it is energetic favorable to expose their hydrophilic part to the surface towards water and cover the hydrophobic part inside [68].

The understanding of protein folding to their unique biofunctional structure is subject of large research activity. A driving force in the folding process is the minimization of the free energy [69], which is determined by the forces characterized above. A major process to lower the free energy in solution is the minimisation of hydrophobic surfaces accessible to the solvent, thus lowering hydrophobic effects. Therefore, most of the non polar amino acid residues are buried in the interior of the proteins, while polar and charged ones are mainly at the surface where they interact with the aqueous surrounding via hydrogen bonds. This separation is not complete, implying that the protein surface consists of patches with different physico-chemical properties. The protonation state of the charged amino acid residues is highly dependent on the pH-value of the solution, having a major impact on the surface properties. The pH-value leading to an effective protein surface charge of zero is called isoelectric point.

The adaption of the lowest energy state plays also an important role in protein interaction with surfaces. If the surface provides a different environment to the proteins than the surrounding solvent, major structural changes in the protein can occur. A good example are hydrophobic surfaces, the interplay of electrostatic forces, van-der-Waals forces and

hydrophobic interactions led to an attraction of the proteins to a surface followed by a structural reorganisation with the goal of energy minimisation. Often, this reorganisation is irreversible and the protein is not able to re-immers in solution by rinsing with buffer, also a loss in protein functionality can occur. Here the mechanism of protein resistant coatings come in the focus [68]. As pointed out in Sec. 2.3.3, a key characteristic of protein resistant coating is to provide a hydrophilic surface and interior, in a way that the protein can remain in the structure it adapts in solution and does not recognise the different environment in terms of polarity. In addition, the protein has to be hindered to overcome this layer, else it may adsorb at the hydrophobic substrate. If both conditions are fulfilled, the protein is hindered to change its structure and to adsorb on the surface, as it is the case for PEG chains [53].

2.4 *In-situ* measurements – motivation and challenge

This work focuses on the characterisation of protein and SAM behaviour and their interaction in an aqueous environment, called *in-situ* in the following sections. It is much easier and more established to measure ultra thin organic layers in air rather than under a thick water layer, therefore it should be elucidated why *in-situ* measurements are so important and what can be learned in addition to the observations achieved from measurements in air.

Protein surface interaction is in most of the applications the interaction of proteins in solution with surfaces. What changes, if the solvent is out in the system? Two cases can be distinguished. First, there are reversible changes. The molecular conformation of polymers is strongly affected by the surrounding solvent. As mentioned in Sec.2.3 several forces contribute to the structural and conformational behaviour of the biopolymers. Two forces with a very high impact on structure are hydrogen bonding and hydrophobic interactions. Both can act intramolecular and intermolecular, however their biggest contribution arises from the surrounding solvent. In Sec. 4.2.3 the transformation of a highly crystalline SAM to a rather amorphous one by immersion in water will be shown. Second there are irreversible changes. Molecular groups are stabilized in water, if the water is removed molecules need to change their conformation to stabilize in other ways. In some cases these changes are not reversible and after reimmersion in water the structure has changed significantly. In Sec.4.2.3 it will be shown, that this is not only the case for proteins but also for oligo ethylene glycols bound on gold.

The question remains, why the majority of published measurements of SAM behaviour is done in air, if its that important to monitor these molecules in an aqueous environment. A simple answer could be: *in-situ* measurements are difficult. To answer this question a bit more thoroughly, a brief look is taken on infrared reflection absorption spectroscopy (IRRAS) measurements of thin organic layers on gold. Measurements in air are quite easy, the gold substrate is measured in reflection mode as a reference and again after immersion in SAM solution and the spectrum is normalized with the reference. To perform

in situ measurements one has to take a lot of things into account. First one has to choose a suitable solvent to be able to monitor the spectral region of choice. Water is suited for the fingerprint region ($1000 - 1500 \text{ cm}^{-1}$) but its absorption is shadowing the region of amid modes ($1500 - 1700 \text{ cm}^{-1}$) as well as the region of CH stretching vibrations ($2900 - 3300 \text{ cm}^{-1}$). For the monitoring in these spectral regions, deuterium oxide (D_2O) is the appropriate solvent. Even with the right solvent one will not get a reasonable signal if measuring through a big bulk solution since water and D_2O are highly absorbing in the infrared region. One has to simulate the layer system with the Fresnel formalism to determine the optimum layer thickness, a few microns. In order to compare mode intensities of different experiments, one needs to obtain reproducible thick layers or measure their thickness and calculate the corresponding attenuation of the signal. Since with IRRAS one measures the thin layer and the bulk solution, the surface sensitive polarisation modulation infrared spectroscopy technique (PMIRRAS) is highly recommended, in order to get a reasonable signal to noise ratio. The next problem is the baseline correction, a quite easy procedure for IRRAS measurements on gold substrates in air, which becomes challenging for PMIRRAS in aqueous environment. In addition to these technical problems, one has to take care for irreversible changes in the SAM structure during drying and reimmersion discussed in Sec. 4.4.4, which can be even more challenging.

Despite of these challenges, it is worth doing measurements in aqueous environment. However, one has to plan experiments very carefully, since they are much more complex than measurements in air.

Chapter 3

Experimental methods

This chapter is intended to give an overview over the sample preparation and the main experimental techniques used in this work. A focus is on infrared spectroscopy. The chapter is organised in the following way. First, the sample preparation of all experiments of this work is summarized in Sec. 3.1, this makes it easy to compare the procedures. In Sec. 3.2 an overview of the fundamental mathematical framework is given, which is necessary to understand the physical background of infrared reflection absorption spectroscopy and is also the basis of the optical calculations relating to the PMIRRAS signal in Sec. 3.3.6 and Sec. 4.1.1. In the following Sec. 3.3 which is the main part of this chapter, the theoretical basics of infrared spectroscopy are given, followed by a description of the experimental setup and the PMIRRAS method. Additionally, home-built thin liquid layer sample cells, the baseline correction and data analysis and a normalisation procedure for PMIRRAS data are described. In the remaining part additional methods used in this work are briefly illustrated, namely X-ray reflectivity in Sec. 3.4, in-plane X-ray Diffraction in Sec. 3.5, spectroscopic ellipsometry in Sec. 3.6 and SPR in Sec. 3.7.

3.1 Sample preparation

3.1.1 Angle dependence of PMIRRAS signal strength

Prime grade wafers (Si-Mat, Germany) were coated with a 5 nm layer of chromium as an adhesion promoter and then with 100 nm of gold by thermal evaporation. Absolute ethanol purissimum pro analysi was purchased from Riedel-de Haën and used as received. 1-Mercapto-11-undecyl hexa(ethylene glycol), a molecule consisting of a thiol anchor group, an alkane spacer with 11 carbon atoms and a headgroup consisting of 6 ethylene glycol units (EG₆OMe) (see Fig. 3.1.1) was purchased from ProChimia, Poland, and was used as received. Monolayers were obtained by self-assembly from a 0.5 mM solution of the thiol in ethanol (EtOH). The immersion time for self-assembly was ap-

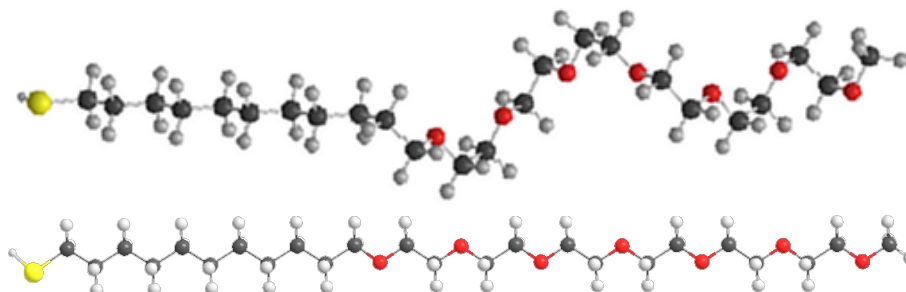


Figure 3.1.1: EG₆OMe molecule, consisting of a thiol anchor group, an alkane linker and an *oligo* (ethylene glycol) group in crystalline structure. The upper schematic shows the helical conformation, the lower one the all-*trans* conformation.

proximately 20 h.

3.1.2 Measurement of specific protein binding on PEG SAMs on dielectric substrates

3.1.2.1 Thin film deposition

Novel substrates consisted of a supporting crystalline silicon wafer (<100> surface, native oxide layer not removed) onto which titanium followed by silicon oxide layers were direct current sputtered (Ti target, 99.995% pure, FHR Anlagenbau GmbH, Germany, magnetron power 100 W, argon pressure 3×10^{-3} mbar and SiO₂ target, 99.995% pure, Kurt J. Lesker Company, U.S.A., magnetron power 100 W, argon pressure 6×10^{-3} mbar). The vacuum system was home-built. The vacuum was not broken between the sputtering of the two layers. Layer thicknesses were nominally 200 nm for the titanium layer and 20 nm for the silicon oxide layer, as estimated from *in-situ* quartz crystal micro balance measurements. For PM-IRRAS measurements, wafers thus produced were cut into suitable pieces (Disco DAD-321 saw, Disco Corp., Tokyo, Japan), cleaned in an ultrasonic bath with 5% surfactant solution (Extran MA02 neutral, Merck, Darmstadt, Germany), copiously rinsed with ultrapure water, cleaned in an ultrasonic bath in EtOH and dried in an argon stream.

3.1.2.2 Wet chemistry

Selectively protein-resistant monolayers were made from biotin-NH-CH₂-CH₂(OCH₂-CH₂)_n-NHCONH(CH₂)₃-Si(OEt)₃ (silane-PEG-biotin, (O-CH₂-CH₂)_n section has Mw = 2000 Da), which was obtained by custom synthesis from Rapp Polymere GmbH (Tübingen, Germany) and stored under argon. Proton nuclear magnetic resonance (1H-NMR) measurements suggested that the sample may be contaminated with biotin-NH-CH₂-CH₂(O-CH₂-CH₂)_n-NH-biotin, which is a likely byproduct of synthesis; as these

molecules lack surface-anchoring triethoxysilane groups, they should be readily rinsed away and should not affect the properties of the eventual self-assembled monolayer. To form self-assembled monolayers, dry toluene (10 ml, 99.85%, extra dry, water <30 ppm, Acros Organics, Geel, Belgium) was added to a flask containing the substrate in a glove box under nitrogen (water < 0.1 ppm), followed by silane-PEG-biotin (1 - 3 mg), before the flask was transferred to a Schlenk line where triethylamine (a few drops, previously distilled under an inert atmosphere) was added also under an inert atmosphere. The flask was sealed and heated briefly to between 80 and 150 °C, allowed to stand at room temperature for 24 hours, and then incubated at 80 °C for 24 hours, then rinsed successively with ethyl acetate, methanol and EtOH (all analytical grade) before being dried in a nitrogen stream and stored under nitrogen (water < 0.1 ppm). Solutions for protein adsorption experiments were made using bovine serum albumin (Sigma Aldrich, St Louis, U.S.A.), streptavidin (from *Streptomyces avidinii*, lyophilized, Serva Electrophoresis, Heidelberg, Germany), and Dulbecco's phosphate buffered saline solution (pH 7.45, Gibco/Invitrogen, Carlsbad, U.S.A., solid tablets made up with ultrapure water (MilliQ Gradient A10 18.2 MWcm, Millipore, Billerica, USA). Glassware for these experiments was cleaned with surfactant (Hellmanex II, Hellma GmbH & Co. KG, Müllheim, Germany), rinsed with ultrapure water and then EtOH and dried in an argon stream.

3.1.3 Measurement of specific protein binding on PEG SAMs on dielectric substrates as a function of PEG chain length

3.1.3.1 Materials

Common organic compounds and bio-chemicals were purchased either from Fluka, Neu-Ulm/Germany, Sigma-Aldrich, Deisenhofen/Germany or Merck, Darmstadt/Germany. 3-Glycidyloxypropyl-trimethoxysilane (GOPTS) and Diisopropylcarbodiimide (DIC) were purchased from Fluka, Neu-Ulm/Germany. Di-amino-*poly*(ethylene glycol) (DAPEG) with molecular masses 900 Da, 2000 Da, 3000 Da, and 6000 Da were purchased from Rapp Polymere, Tübingen/Germany. d-Biotin and (2-(1H-benzotriazol-1-yl)-1,1,3,3-tetramethyluronium tetrafluoroborate) (TBTU) was purchased from Sigma-Aldrich, Deisenhofen/Germany.

3.1.3.2 Wet chemistry

15 µL GOPTS were pipetted onto an activated dry slide and covered with another slide ('sandwich-technique'). After silanisation for 1 h the slides were rinsed with dry acetone and dried in a nitrogen stream. For immobilisation of diamino-*poly*(ethylene glycol), 10 µL of the a DAPEG/methylene chloride solution was pipetted onto a slide in the concentration of 4 mg/mL. Subsequently, the slides were transferred into an oven where immobilisation took place in an open-topped vessel overnight at 70 °C. Afterwards, the

slides were rinsed with Milli-Q water and dried in a nitrogen stream. For pure PEG layers only one length of PEG molecules was used.

3.1.4 *In-situ* growth, temperature behaviour and stability of OEG SAMs

As substrates gold coated glass slides (Arrandee) were used. The slides were successively sonicated in MilliQ water (18.2 MW cm, Millipore) and EtOH (99.9%, Riedel de Haën), then dried in an argon stream, treated with an ozone producing UV-light for 20 min and rinsed with MilliQ water. The cleaning treatment was done directly before each experiment. For the SAM growth the *in-situ* cell a 1.25 mM solution of C₁₁EG₆OMe thiol (Prochimia, Gdansk, Poland) in MilliQ water with 0.1 M NaF was used. For the SAMs grown in bulk solution a 0.5 mM solution of C₁₁EG₆OMe in MilliQ water was used, if other thiol concentrations are used it is indicated in the results part.

3.1.5 Surface Plasmon resonance measurements

Cleaned glass slides (Menzel GmbH, Braunschweig) were coated with 5 nm of titanium as adhesion layer and 50 nm of gold by thermal evaporation. After the coating, slides were cut into suitable pieces (Disco DAD-321 saw, Disco Corp., Tokyo, Japan), cleaned by successively copiously rinsing with ultrapure water and EtOH and dried in an argon stream. For the SAM growth in the SPR cell a 10 μ M solution of C₁₁EG₆OMe thiol (Prochimia, Gdansk, Poland) in MilliQ water was used.

3.1.6 In-plane grazing incidence X-ray scattering

Prime grade wafers (Si-Mat, Germany) were coated with a 5 nm layer of chromium as an adhesion promoter and then with 20 nm of gold by thermal evaporation. Absolute ethanol purissimum pro analysi was purchased from Riedel-de Haën and used as received. Monolayers were obtained by self-assembly from a 0.5 mM solution of C₁₁EG₆OMe thiol (Prochimia, Gdansk, Poland) in EtOH. The immersion time for self-assembly was approximately 15 h.

3.2 Optical calculation and simulation

The following paragraph is intended to provide a basic understanding of the theory of wave propagation at the interface of media with different optical properties and show, how this can be used to simulate optical data. In order to get a quantitative understanding the

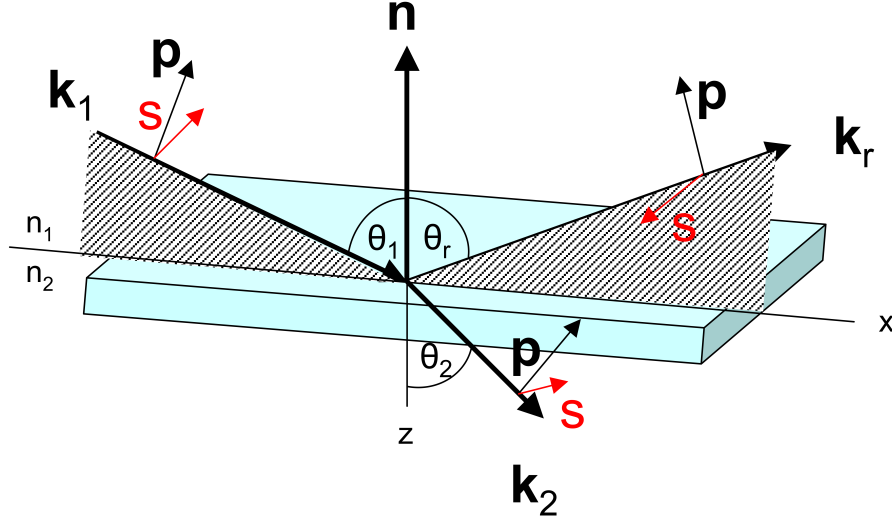


Figure 3.2.1: Reflection and refraction at a phase boundary

wave equations are regarded, first without considering absorption effects:

$$\Delta E - \epsilon_0 \epsilon \mu_0 \mu \ddot{E} = 0 \quad (3.2.1)$$

$$\Delta H - \epsilon_0 \epsilon \mu_0 \mu \ddot{H} = 0 \quad (3.2.2)$$

E and H represent the electrical field and the magnetic field, ϵ_0 and μ_0 the permittivity and permeability of free space and ϵ and μ stand for the dielectric constant and the magnetic permeability. The planar waves:

$$E = E_0 \exp [i (\omega t - kr)] \quad (3.2.3)$$

$$H = H_0 \exp [i (\omega t - kr)] \quad (3.2.4)$$

are solutions of the wave equations, ω is the angular frequency of the wave, substituting them into the wave equation gives a relation of the wave vector k :

$$k^2 = \frac{\omega^2}{c^2} \epsilon \mu \quad (3.2.5)$$

The refractive index n is defined as:

$$n = \frac{c}{v} = \frac{ck}{\omega} = \sqrt{\epsilon \mu} \quad (3.2.6)$$

with c and v being the velocities of electromagnetic radiation in vacuum and in media respectively.

Considering absorption in media, one has to introduce a damping term into 3.2.1 and 3.2.2, leading to solutions with complex values of n and k .

If electromagnetic radiation passes through a boundary between two different media a part of it is reflected. The angle of incidence θ_1 equals the angle of reflection θ_r , compare to Fig. 3.2.1. An other part is refracted due to Snell's law:

$$\frac{\sin(\theta_1)}{\sin(\theta_2)} = \frac{n_2}{n_1} \quad (3.2.7)$$

It relates the angle of refraction θ_2 as a function of the angle of incidence θ_1 and the refractive indices in both media n_1 and n_2 , compare to Fig.3.2.1. For a quantitative understanding of the intensities of the transmitted and reflected beam, one can use Eq. 3.2.3 for the incident, reflected and refracted component of the beam. It is convenient to resolve the electromagnetic wave in a linear polarized component with an electrical field vector laying in the plane of incidence, called p-component (compare to Fig. 3.2.1) and a component with an electrical field vector orthogonal to the plane of incidence called s-component. At the boundary between two media the tangential component of the electrical field E and the normal component of the dielectric displacement $D = \varepsilon E$ are continuous. Using the Maxwell equations and these boundary conditions, one can derive the Fresnel formulas:

$$r_p = \frac{E_r}{E_1} = \frac{n_2 \cos \theta_1 - n_1 \cos \theta_2}{n_1 \cos \theta_2 + n_2 \cos \theta_1} \quad (3.2.8)$$

$$r_s = \frac{E_r}{E_1} = \frac{n_1 \cos \theta_1 - n_2 \cos \theta_2}{n_1 \cos \theta_1 + n_2 \cos \theta_2} \quad (3.2.9)$$

$$t_p = \frac{E_2}{E_1} = \frac{2n_1 \cos \theta_1}{n_1 \cos \theta_2 + n_2 \cos \theta_1} \quad (3.2.10)$$

$$t_s = \frac{E_2}{E_1} = \frac{2n_1 \cos \theta_1}{n_1 \cos \theta_1 + n_2 \cos \theta_2} \quad (3.2.11)$$

r_p and r_s are the amplitudes of reflection of the p- and s-component, t_p and t_s are the amplitudes of transmission of the components. For absorbing materials, the refractive indices and angles become complex. From the Fresnel coefficients the reflection and transmission can be derived:

$$R_{12}^{s,p} = |r^{s,p}|^2 \quad (3.2.12)$$

$$T_{12}^{s,p} = |t^{s,p}|^2 \frac{n_2 \cos \theta_2}{n_1 \cos \theta_1} \quad (3.2.13)$$

For reasons of energy conservation:

$$T_{12}^{s,p} + R_{12}^{s,p} = 1 \quad (3.2.14)$$

The calculations above describe the light propagation at one single phase boundary, in experiments systems where more than two layers are used, thus a more general approach is needed in order to calculate the optical properties of these systems. The following section including a brief description of the matrix formalism by Hansen is taken from [23],

note that complex values for the refractive index are used. The Fresnel equations can be re-written for the interface between two layers j and $j + 1$ in the stack:

$$r_p^j = \frac{\hat{n}_{j+1}^2 \xi_j - \hat{n}_j^2 \xi_{j+1}}{\hat{n}_{j+1}^2 \xi_j + \hat{n}_j^2 \xi_{j+1}} \quad t_p^j = \frac{2\hat{n}_{j+1} \hat{n}_j \xi_j}{\hat{n}_{j+1}^2 \xi_j + \hat{n}_j^2 \xi_{j+1}} \quad (3.2.15)$$

$$r_s^j = \frac{\xi_j - \xi_{j+1}}{\xi_j + \xi_{j+1}} \quad t_s^j = \frac{2\xi_j}{\xi_j + \xi_{j+1}} \quad (3.2.16)$$

where $\xi_j = \hat{n}_j \cos \Theta_j = \sqrt{\epsilon_j - \epsilon_1 \sin^2(\Theta_1)}$ and $\epsilon_j = \hat{n}_j^2$. Care has to be taken when calculating the square root of the complex expression for ξ , since the resulting hyperbolic functions are periodic and only the positive values of the real and imaginary parts must be used for the calculation. If the thickness of layer j is denoted by d_j and the complex variables

$$q_j = \frac{\xi_j}{\hat{n}_j^2} \quad \beta_j = \frac{2\pi d_j}{\lambda} \xi_j \quad (3.2.17)$$

are defined for convenience, then the optical matrices for layer j for parallel (p) and perpendicular (s) polarization take the form:

$$M_j^p = \begin{pmatrix} \cos \beta_j & -\frac{i}{q_j} \sin \beta_j \\ -iq_j \sin \beta_j & \cos \beta_j \end{pmatrix} \quad (3.2.18)$$

$$M_j^s = \begin{pmatrix} \cos \beta_j & -\frac{i}{\xi_j} \sin \beta_j \\ -i\xi_j \sin \beta_j & \cos \beta_j \end{pmatrix} \quad (3.2.19)$$

In general for an N-layer system, $N - 1$ matrices can be defined, since the ambient medium is semi-infinite. For the above-mentioned four-layer system, three matrices are needed. In order to calculate the reflectivity of the whole stack, the characteristic matrix:

$$M^{s,p} = \prod_{j=1}^{N-1} M_j^{s,p} = \begin{pmatrix} m_{11}^{s,p} & m_{12}^{s,p} \\ m_{21}^{s,p} & m_{22}^{s,p} \end{pmatrix} \quad (3.2.20)$$

has to be computed. Then the reflection coefficients for the whole stratified medium can be expressed using the following relations:

$$r_p = \frac{(m_{11}^p + m_{12}^p q_N) q_0 - (m_{21}^p + m_{22}^p q_N)}{(m_{11}^p + m_{12}^p q_N) q_0 + (m_{21}^p + m_{22}^p q_N)} \quad (3.2.21)$$

$$r_s = \frac{(m_{11}^s + m_{12}^s \xi_N) \xi_0 - (m_{21}^s + m_{22}^s \xi_N)}{(m_{11}^s + m_{12}^s \xi_N) \xi_0 + (m_{21}^s + m_{22}^s \xi_N)} \quad (3.2.22)$$

The relations can be used to calculate the infrared reflection absorption intensity (see Sec. 4.1.1) and to calculate the mean square electrical field (MSEF) within a layered system. This is especially useful at the position of the absorbing thin film. The calculations are

done with the Hansen matrix formalism [24] [27] using the optical terms 3.2.17 and matrices 3.2.18 and 3.2.19 as well as the reflectivity coefficients 3.2.21 and 3.2.22 from above. In the following paragraph it is shown how to calculate the electrical and magnetical fields in the first two layers, for the complete algorithm see Ref. [27].

The first step is the calculation of the so-called column vectors, characterising the tangential components of the electric and magnetic field:

$$Q_1^s = \begin{bmatrix} E_{y1}^0 \\ H_{x1}^0 \end{bmatrix} = \begin{bmatrix} 1 + r^s \\ \beta_1(1 - r^s) \end{bmatrix} \quad (3.2.23)$$

$$Q_1^p = \begin{bmatrix} H_{y1}^0 \\ E_{x1}^0 \end{bmatrix} = \begin{bmatrix} 1 + r^p \\ q_1(1 - r^p) \end{bmatrix} n_1 \quad (3.2.24)$$

For the layer, containing the position of the chosen electrical field calculation, the following matrices have to be determined:

$$N_k^s(z) = \begin{bmatrix} \cos [2\pi\nu\xi_k(z - z_{k-1})] & \frac{i}{\beta_k} \sin [2\pi\nu\xi_k(z - z_{k-1})] \\ i\beta_k \sin [2\pi\nu\xi_k(z - z_{k-1})] & \cos [2\pi\nu\xi_k(z - z_{k-1})] \end{bmatrix} \quad (3.2.25)$$

$$N_k^p(z) = \begin{bmatrix} \cos [2\pi\nu\xi_k(z - z_{k-1})] & \frac{i}{q_k} \sin [2\pi\nu\xi_k(z - z_{k-1})] \\ iq_k \sin [2\pi\nu\xi_k(z - z_{k-1})] & \cos [2\pi\nu\xi_k(z - z_{k-1})] \end{bmatrix} \quad (3.2.26)$$

with $z_{k-1} = \sum_{h=2}^{k-1} d_h \leq z \leq z_k = \sum_{h=2}^k d_h$. Now the electrical field above the layered system at $-\infty < z \leq 0$ can be calculated:

$$Q_1^{s,p}(z) = N_1^{s,p}(z)Q_1^{s,p} \quad (3.2.27)$$

as well as inside the first layer at $0 \leq z \leq d_1$.

$$Q_2^{s,p}(z) = N_2^{s,p}(z)Q_1^{s,p} \quad (3.2.28)$$

Assigning the following elements to the vectors $Q_k^{s,p}(z)$

$$Q_k^{s,p}(z) = \begin{bmatrix} U_k^{s,p}(z) \\ V_k^{s,p}(z) \end{bmatrix} \quad (3.2.29)$$

and the value $W_k(z) = n_1 \sin \varphi_1 U_k^p(z) / \hat{\epsilon}_k$, with the dielectric function $\hat{\epsilon}_k$ of the corresponding layer, the resulting MSEF can be expressed as:

$$\langle E_k^{s2}(z) \rangle = \langle E_{yk}^2(z) \rangle = |U_k^s(z)|^2 \quad (3.2.30)$$

$$\langle E_{xk}^2(z) \rangle = |V_k^p(z)|^2 \quad (3.2.31)$$

$$\langle E_{zk}^2(z) \rangle = |W_k(z)|^2 \quad (3.2.32)$$

$$\langle E_k^{p2}(z) \rangle = \langle E_{xk}^2(z) \rangle + \langle E_{zk}^2(z) \rangle^2 \quad (3.2.33)$$

The magnitudes are corresponding to the ratio of the electrical field at position z with the incident electrical field. With the algorithm above it is possible to simulate signal strength and electrical field for a given layer system. This can be used to choose optimized experimental conditions. A program code in Igor Pro can be found in the appendix, a standalone program to calculate the MSEF is also available from Vlad Zamlini [70].

Table 3.3.1: Infrared energy range

region	wavenumber (cm^{-1})	excitations
near infrared	12800 - 4000	combination vibrations, overtones
mid infrared	4000 - 200	molecular normal modes
far infrared	< 200	lattice - and backbone vibration

Table 3.3.2: Conversion between common spectroscopic units

unit	formula	conversion from wavenumber [cm^{-1}]
frequency [s^{-1}]	$f = c \cdot \tilde{\nu}$	$f [\text{Hz}] = \tilde{\nu} [\text{cm}^{-1}] \cdot 3 \cdot 10^{10}$
energy [eV]	$E = h \cdot c \cdot \tilde{\nu}$	$E [\text{eV}] = \tilde{\nu} [\text{cm}^{-1}] / 8065.5$
wavelength [μm]	$\lambda = 1/\tilde{\nu}$	$\lambda [\mu\text{m}] = 10000/\tilde{\nu} [\text{cm}^{-1}]$

3.3 Infrared spectroscopy

3.3.1 Theoretical background

Molecules can be excited to vibrations by infrared light. By measuring the part of light adsorbed by the sample one can determine the energies of excitation. Since these energies are characteristic for each molecule and also affected by the molecules' environment, infrared spectroscopy is a valuable tool to elucidate molecular structure.

One can distinguish three energy ranges per definition (see Tab.3.3.2). In the low wavenumber region, called far infrared, one can find absorption modes due to lattice vibrations in crystals and some backbone vibrations. In the mid infrared region, which is most important for detecting molecules and their conformations, one can find the majority of molecular normal modes. The near infrared region, addressing the high energy range, contains mostly combination vibrations and overtones. This work focuses on infrared spectroscopy in the mid infrared region.

There are different units to describe radiation energy, most common in spectroscopy is the unit wavenumber. Since in this work all numbers are described with this unit, in Tab. 3.3.2 the conversion from wavenumber into frequency, energy and wavelength is given. Note that c is the velocity of light in vacuum and h is Planck's constant.

To excite a vibration several conditions have to be fulfilled. First, the molecule needs to be polar, resulting in a dipole moment. Second, this dipole moment has to change during vibration, also called transition dipole moment μ_{el} . Third, the electrical field of the radiation exciting the molecule E needs to have a component colinear with the dipole moment. The resulting absorption is:

$$\Delta I \sim \frac{\partial \mu_{el}}{\partial r} \cdot E \quad (3.3.1)$$

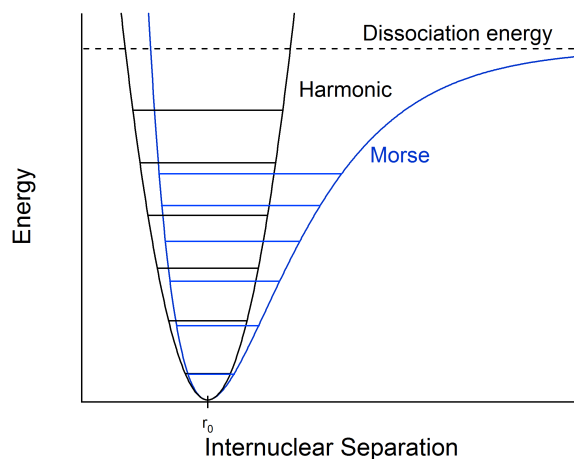


Figure 3.3.1: Comparison of the Potentials and Energies of the harmonic- and the anharmonic oscillator

As a simple model for vibration in a molecule with two atoms one can assume a harmonic oscillator. With a spring constant k , describing the forces between the atoms and μ being the reduced mass one gets for the eigenfrequency of the vibration:

$$\nu = \frac{1}{2\pi} \sqrt{\frac{k}{\mu}} \quad (3.3.2)$$

$$\mu = \frac{m_1 \cdot m_2}{m_1 + m_2} \quad (3.3.3)$$

In a Quantum mechanic framework one can calculate the different energies resulting from Eq. 3.3.2:

$$E = h\nu \left(n + \frac{1}{2} \right); n = 0, 1, 2, 3, \dots \quad (3.3.4)$$

In the harmonic oscillator, there can be transitions between equidistant energy levels with $\Delta\nu = \pm 1$. However, there are two real molecule properties not consistent with this simple model. Strong repulsive forces act if atoms come too close to each other, according to the Pauli principle and dissociation occurs if molecules are too far away from each other. So, vibrations can be better described by the non symmetric anharmonic oscillator model characterized by a Morse potential and energy levels converging towards the dissociation energy (compare to Fig. 3.3.1). This allows also transitions between energy levels with $\Delta\nu = \pm 2, \pm 3, \pm 4, \dots$. However, these transitions are very unlikely, resulting in strongly reduced intensities of the corresponding absorption modes.

Molecules have a defined number of degrees of freedom. Considering that each atom can move in three orthogonal directions, a molecule with N atoms has $3N$ degrees of freedom.

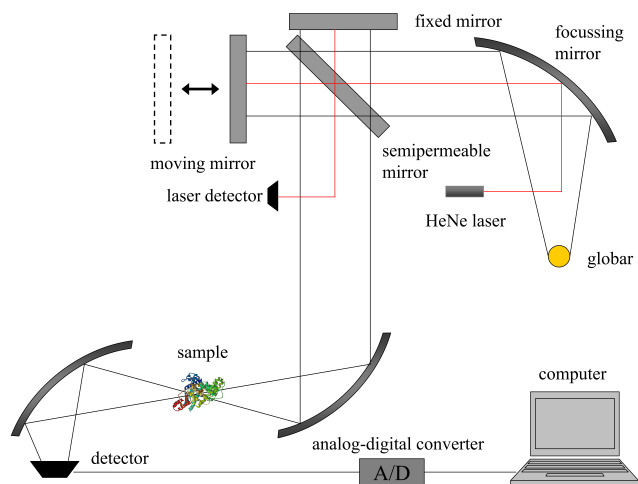


Figure 3.3.2: Schematic setup of a FTIR spectrometer. Infrared light is produced by a globar, interfering at the core of the spectrometer, a Michelson interferometer and measured by the detector after passing the sample. After performing a Fourier transformation an absorption spectrum is obtained.

Since its centre of mass can translate and rotate in three directions keeping the positions of the atoms to each other constant there are $3N - 6$ degrees of freedom left for vibration called normal modes. Linear molecules such as carbon dioxide can only rotate in two directions leaving them $3N - 5$ normal modes. A normal mode is a vibration characterized by a vibration of all contributing atoms in phase and with the same frequency.

One can distinguish two kinds of vibrations. The first kind are stretching vibrations (also called valence vibrations), in which the atoms are moving on an axis colinear to their bond. If the vibrating atomic group is symmetrical and this symmetry is preserved during vibration, it is called symmetric stretching vibration. If the symmetry changes it is called asymmetric stretching vibration. The second type are vibrations, in which the bond angles between the atoms are changing. Important examples are rocking, twisting, wagging and scissoring vibrations. They can be rather symmetric or asymmetric similar to stretching vibrations.

3.3.2 Fourier transform infrared spectrometry

An obvious way to measure a vibrational spectrum would be a stepwise collection for every single wavelength. However, there is a method called Fourier transform infrared spectroscopy (FTIR spectroscopy), being much more efficient especially in terms of time consumption and signal to noise ratio. In the following paragraph the essential parts of an FTIR spectrometer, namely the radiation source, the beam splitter and the detector, are described, compare to Fig. 3.3.2. Full radiators are used as radiation source. Their spec-

tral characteristics are determined by Planck's law, featuring a temperature dependent maximum which has a smooth slope to higher wavenumbers and a steep slope to smaller ones, respectively. There are two common sources. One is the Nernst rod, a small stick mainly consisting of zirconium oxide. Its working temperature of about 1900 K results in a emission maximum at $\lambda = 1 - 2\mu m$. At low temperature it is insulating and so it has to be heated and ignited when switched on. The other one is the globar, it features a rod of siliciumcarbide and can be ignited directly, due to its electrical conductivity in the cold state. Due to its working temperature of about 1500 K, its emission maximum is slightly higher than for the Nernst rod. There are two major kinds of detector systems. 1) Thermal detectors using the heating induced by the infrared radiation. Most common are DTGS-detectors containing perdeuterated triglycerine sulphate which electrically polarises spontaneously below the Curie temperature. Changes in spectral intensity change this polarisation and lead to a detection. This kind of detector can be used in the whole infrared spectral range and needs to be cooled down only to $-40\text{ }^\circ\text{C}$ which can be achieved with Peltier elements. 2) Photoelectric detectors exploiting the direct interaction with the photons. A widely-used type is the MCT detector photo diode consisting of mercury, cadmium and telluride. It needs to be cooled with liquid nitrogen and covers only a small spectral region. However, its signal-to-noise ratio is two orders of magnitudes higher than the one of DTGS-detectors, making it essential for the measurement of monolayers.

The core piece of FTIR spectrometers is the beam splitter incorporating a Michelson interferometer. The incoming infrared light is split into two equal parts with a semitransparent mirror. They are interfering after passing their path in the mirror system. In Fig. 3.3.2 one can see that one of the paths has a fixed distance, the other one can be varied by a moving mirror. Depending on the path difference in relation to the wavelength the interference pattern can be either constructive or destructive. First, the monochromatic interference on the sample of the He-Ne laser coupled into the beam path should be illustrated. The interference can be described by:

$$I = \frac{1}{2}I_0 \left[1 + \cos \left(2\pi \frac{\delta}{\lambda} \right) \right] \quad (3.3.5)$$

I is the intensity of the HeNe source. If the deflection δ is zero or a multiple of the wavelength λ , the amplitudes are co added, for δ equal to $\frac{\lambda}{2}$ or multiples they cancel out. The laser beam is coupled in and detected with a particular optic. Its purpose is to trigger the measurements at equal distances along the mirror translation. This leads to a determination of the mirror position with a accuracy of less than $0.005\ \mu m$ and therefore in a wavenumber accuracy better than 0.01 cm^{-1} .

In case of continuous wavelength the intensity has to be integrated over the whole spectral range. At zero path difference, the amplitudes of the radiation of all wavelength co add, this is called centerburst. For any other point constructive interference is achieved for only one wavelength:

$$I(\delta) = \int_{-\infty}^{+\infty} \frac{1}{2} I_0(\lambda) \left[1 + \cos 2\pi \frac{\delta}{\lambda} \right] d\lambda \quad (3.3.6)$$

In terms of wavenumbers $\tilde{\nu}$ one gets:

$$I(\delta) = \int_{-\infty}^{+\infty} \frac{1}{2} I_0(\tilde{\nu}) [1 + \cos 2\pi \tilde{\nu} \delta] d\tilde{\nu} \quad (3.3.7)$$

In order to get real intensities the spectral characteristic of the spectrometer $B(\tilde{\nu})$ and the subtraction of the average signal have to be taken into account:

$$I(\delta) = \int_{-\infty}^{+\infty} B(\tilde{\nu}) \cos 2\pi \tilde{\nu} \delta d\tilde{\nu} \quad (3.3.8)$$

This equation is exactly the Fourier cosine transformation. With the inverse transformation the single channel spectrum can be calculated from the interferogram:

$$I(\tilde{\nu}) = \int_{-\infty}^{+\infty} B(\delta) \cos 2\pi \tilde{\nu} \delta d\delta \quad (3.3.9)$$

Which can, due to the even function, finally be written as:

$$I(\tilde{\nu}) = \int_{-\infty}^{+\infty} B(\delta) \exp(-2\pi i \tilde{\nu} \delta) d\delta \quad (3.3.10)$$

For signal processing one has to taken into account a few points:

- In real spectrometers, the maximal mirror movement is limited to a few centimeters, so it cannot be integrate to infinity, but there are finite limits. Thus, the signal can be fold with a $\frac{\sin x}{x}$ function and introduce secondary maxima to every absorption mode. To prevent this, one performs a apodisation, i.e. a folding of the interferogram with a function dependent on δ , which is smoothing the interferogram out to the borders. The easiest function is a triangle attenuating the interferogram linearly from $\delta = 0$ to $\delta = max$. This results in a $\frac{\sin^2 x}{x^2}$ function, defining the formal limit of the resolution $\Delta\tilde{\nu} = 1/\delta$.
- Due to the limited number of points measured in the interferogram, the sampling intervals in the spectra are not dense enough, resulting in the so-called picket fence effect. To prevent this and smooth the spectra, it is extended by zero-values. Since

this adds no real information the spectral resolution is not enhanced and also there is no change in line shape, however the spectrum looks smoother due to interpolated points in between the measured ones.

- At this point, a single channel spectrum, containing all information regarding spectral characteristic of the global, optical characteristic of the spectrometer and background absorption has been calculated. Those can be much higher than the measured signal. To get rid of those effects the spectrum is normalized with a single channel spectrum of a background measurement. The absorption A is calculated by:

$$A = \lg \frac{1}{T} = \lg \frac{I_0}{I} \quad (3.3.11)$$

T is the normalized transmission, I the single channel spectrum and I_0 the single channel reference spectrum.

3.3.3 Infrared transmission measurements

An easy way to obtain spectra of thin films on silicon substrates are measurements in transmission mode. The spectrum is normalized by a spectrum of the bare substrate. In this Sec. the experimental implementation of this method is elucidated. The results are compared with PMIRRAS measurements in Sec. 4.1.4.

For infrared measurements of the absorption of liquid layers of about 25 μm the sensitivity of a TGS-detector (equipped in the Bruker Vertex70 spectrometer by default) is good enough. For molecular monolayers, however, a MCT detector is needed, offering a signal to noise ratio two orders of magnitude higher. In Fig. 3.3.4A and C single channel transmission spectra of a silicon substrate mounted in the standard Bruker transmission sample holder and the resulting transmission spectra after normalisation are shown. Due to remounting of the sample in the holder, the single channel spectra differ in intensity over a broad range and it is not possible to normalise them suitably. If two spectra, however, are measured without touching the sample in the holder the intensity of the single channel spectrum remained constant, even if the whole sample holder was removed and the substrate was incubated in a protein solution remaining in the holder, see Fig. 3.3.4A. This led us to the idea for the construction of a transmission cell, holding the substrate in a way, that it is forced to adopt exactly the same position after remounting (see Fig. 3.3.3). As shown in Fig. 3.3.4C and D, the single channel spectrum remained constant after remounting of the sample, enabling functionalization of the bare sample and a normalization of the spectra of the thin film with the spectrum of the bare substrate measured before. For a suitable normalisation with a reference spectra it proved to be necessary to measure this reference spectra with the same substrate functionalized with the thin film.

Another problem is the background correction of the spectra. As can be seen in Fig. 4.1.21, there are strong absorption bands of water vapor. Even if the biggest part of them is

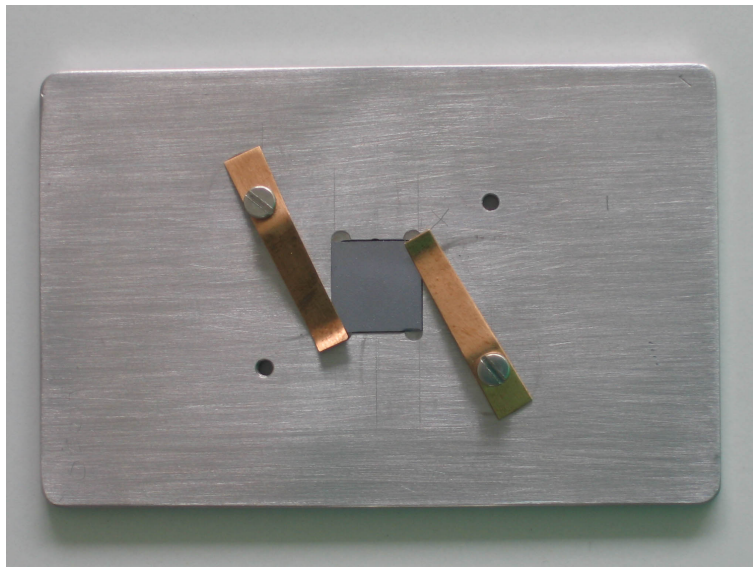


Figure 3.3.3: Home-built sample holder, enabling a mounting of the substrate in a fixed position and so the measurement of thin films on silicon substrates in transmission mode.

suppressed by purging the system with dry air and a waiting period of 60 min per measurement for equilibration, the intensity of the water vapor bands is of the same order as a monolayer signal. If this spectral region is of interest, as for example the case for a test of biofouling of functionalized surfaces, these bands can make a conclusion nearly impossible. The standard method would be a measurement under vacuum conditions. With an dry air purged setup, however, also a solution is possible. To this end a transmission spectra of a substrate in an open chamber was measured (normal air composition, including a big fraction of water vapor) and the measurement normalized with a spectra collected with a closed chamber purged with dry air for 60 min. The fraction of this spectra, added to the spectra which should be corrected was matched in such a way that the absorption bands due to water vapor vanished, enabling the detection of protein monolayers, see Fig. 4.1.21 in Sec. 4.1.4.

3.3.4 Infrared reflection absorption spectroscopy (IRRAS)

For the characterisation of monolayers, the signal-to-noise ratio of infrared transmission spectroscopy is not good enough. However, there are specialised infrared methods to overcome this problem. For the characterisation of molecules on metal surfaces infrared reflection absorption spectroscopy has been proven as a useful tool. For an basic understanding of the wave propagation at the interface of media with different optical properties see Sec. 3.2. When infrared light is reflected at metal surfaces the surface selection rule has to be taken into account (see Fig. 3.3.5). The electrical field inside a conductor is zero and the electrical field outside a conductor is perpendicular to its surface. To fulfill

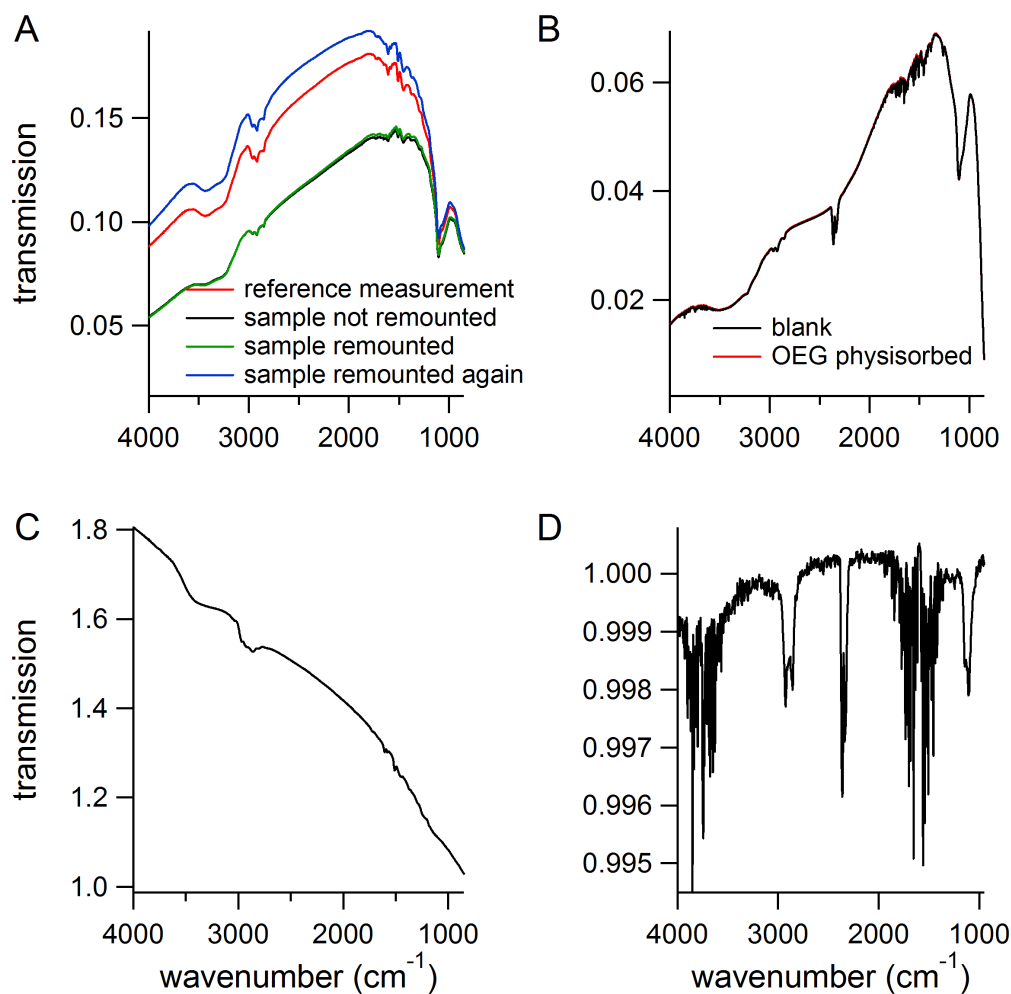


Figure 3.3.4: A comparison of transmission spectra measured with a standard transmission sample holder and a home-built sample holder. In A single channel spectra are shown, which are measured with a standard sample holder. Note, that the intensity of the same sample strongly varies for each measurement when the sample is remounted in the holder. The corresponding normalised transmission spectra (C) varies over a very big range, preventing a suitable analysis of the absorption modes. B shows single channel spectra measured with the new sample holder, the intensity of the spectra signal is virtually the same after manipulation and remounting of the sample, enabling a analysis of the absorption modes of the thin layer on the substrate. In this case a OEG solution in EtOH is vaporised on the substrate, the thin film is formed by OEG molecules laying amorphous on the substrate. Note, the absorption modes in the C-O-C region and in the CH₃ region, also note the big absorbing due to water vapor.

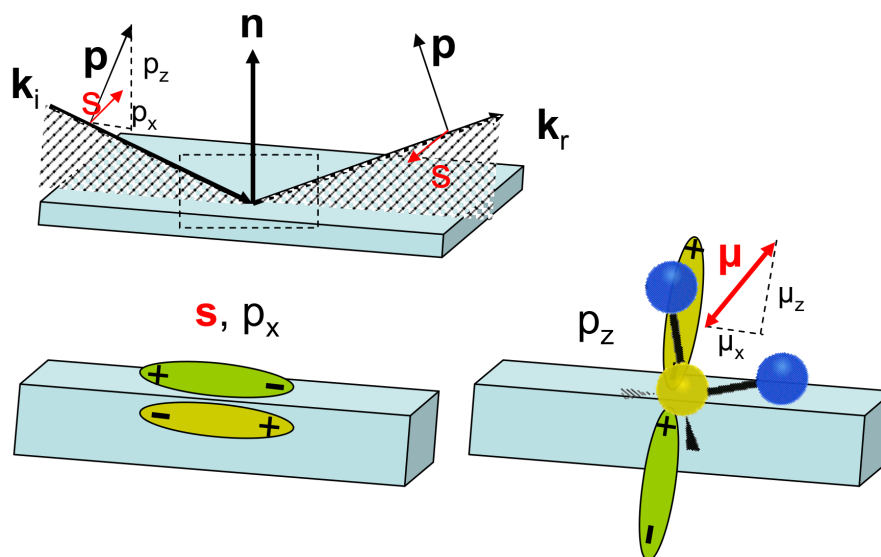


Figure 3.3.5: Surface selection rules for electrical fields at metallic interfaces. The z-component of the perpendicular component of the electrical field (p-polarized light) induces an electrical field parallel to the external field, inducing an enhancement. In contrast, the parallel component of the electrical field induces an antiparallel field, cancelling out the external field in the vicinity of the surface. Thus, only the z-component of a dipole moment can be measured, which can be used for orientation analysis of molecules on the surface.

this condition, for the tangential components (s-polarized light, compare Fig. 3.2.1) of an external electrical field, an field inside the conductor is induced in antiparallel orientation cancelling out the external field in the vicinity of the conductor surface. Also, the perpendicular component (p-polarized light) of the external electrical field is inducing an electrical field, which is parallel to the external field and leads to an enhancement. Therefore our thin substrate on top of the metal layer is only excited by the perpendicular component of the electrical field. According to Eq. 3.3.1 only dipole moments oriented perpendicular to the surface can be excited. This can be used for a determination of the orientation of molecules, if the orientation of the corresponding dipole moments within the molecule are known. The signal strength of IRRAS also depends on the angle of incidence of the incoming beam:

$$I \sim \frac{d}{\cos \theta_1} \quad (3.3.12)$$

where d is the film thickness and θ_1 the angle of the incoming beam. According to Eq. 3.3.12 the signal strength is notably enhanced at grazing incidence.

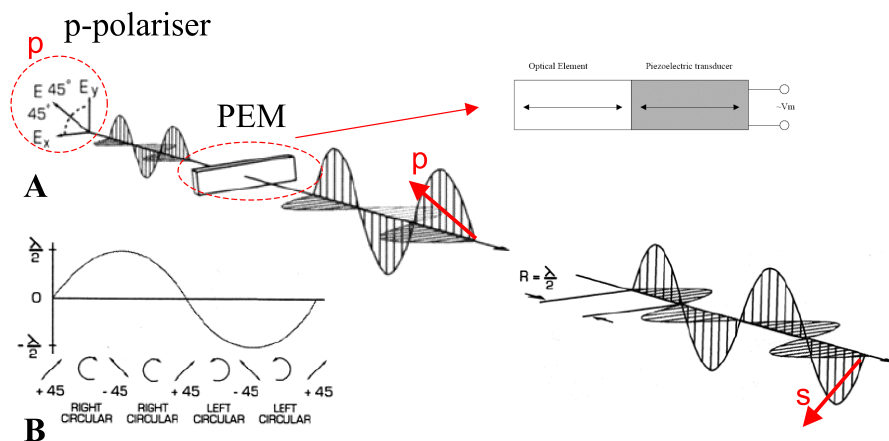


Figure 3.3.6: Principle of operation of a photoelastic modulator. A shows the change of polarisation due to a phase shift of the x-component of the electromagnetic field. B shows the polarisation status as a function of time.

3.3.5 Polarisation modulation infrared spectroscopy (PMIRRAS)

With polarisation modulation infrared spectroscopy (PMIRRAS) it is possible to improve the signal to noise ratio in comparison to IRRAS significantly. Also the spectrum is corrected for the background and no reference measurement is required. The following section will explain the principles of PMIRRAS.

The PMIRRAS technique exploits the surface selection rules of polarized electrical fields at metal interfaces (see Sec. 3.3.4). The electrical field components parallel to the interface are cancelled out by the induced dipole moment, while the components perpendicular to the surface are enhanced. In PMIRRAS the polarisation of the beam is periodically changed from s to p. The s-polarized beam is attenuated due to absorption, while passing the bulk media, but not in the vicinity of the surface due to the missing electrical field, a p-polarized beam is attenuated by bulk media and surface absorption. By subtracting these signals and normalizing them with the average signal one obtains a surface sensitive signal without bulk contribution.

Technically the beam is modulated in the following way. The infrared light is p polarized and coupled into a photoelastic crystal with an angle of 45 degrees. The crystal is periodically compressed and expanded with an piezo element and changes its refractive index. The component of the electrical field in the direction of birefringence is periodically retarded and accelerated. At maximal retardation and acceleration, the electrical field leaving the crystal has changed its polarisation from p to s (see Fig. 3.3.6). The absolute phase change is frequency dependent:

$$\varphi_0 = \frac{GV_{PEM}}{\lambda} \quad (3.3.13)$$

The following optimal relations are strictly valid only for a single wavelength. One has to

adjust this number in the center of the spectral region of interest and has to limit this area ideally to a few hundred wavenumbers. The change in polarisation is time dependent, the polarisation of the beam leaving the PEM crystal is:

$$I_D(\varphi) = \frac{I_P + I_S}{2} + \frac{I_P - I_S}{2} \cos \varphi \quad (3.3.14)$$

$$\varphi = \varphi_0 \cos(\omega_{PEM}t + \phi_{PEM}) \quad (3.3.15)$$

Note, that the phase φ is determined by a double cosine relation. This can be expanded in a Bessel series [24]:

$$\cos(\varphi) = J_0(\varphi_0) + 2 \sum_{k=1}^{\infty} (-1)^k J_{2k}(\varphi_0) \cos(2k\omega_{PEM}t + \phi_{PEM}) \quad (3.3.16)$$

Since the Bessel terms are decreasing rapidly with increasing order, only the terms J_0 and J_2 are relevant for a demodulation of the signal:

$$\cos(\varphi) \approx J_0(\varphi_0) + 2J_2(\varphi_0) \cos(2\omega_{PEM}t + \phi_{PEM}) \quad (3.3.17)$$

The signal is demodulated with the help of a lock-in amplifier. In short, it deconstructs the signal and noise into its Fourier components. By multiplying the signal with a reference signal with a fixed frequency (in this case the PEM frequency $U_0 \cos(2\omega_{PEM}t + \phi_{PEM})$, the periodically changing difference signal, which is modulated by the second order Bessel term, is extracted:

$$\Delta I_{sample} = (I_P - I_S) J_2(\phi_0) \quad (3.3.18)$$

With the help of a low pass filter the average signal modulated by the zero order Bessel term is extracted:

$$\langle I \rangle_{ref} = \frac{1}{2} [I_P + I_S + (I_P - I_S) J_0(\varphi_0)] \quad (3.3.19)$$

For metallic substrates the intensities of the p and s polarized electrical field are virtually equal, so this equation can be simplified to:

$$\langle I \rangle_{ref} = \frac{1}{2} [I_P + I_S] \quad (3.3.20)$$

Finally the measured reflectivity signal can be written as:

$$\frac{\Delta R}{R} = \frac{\Delta I_{sample}}{\langle I \rangle_{ref}} \approx \frac{I_P - I_S}{\frac{1}{2}(I_P + I_S)} J_2(\varphi_0) \quad (3.3.21)$$

It is the normalized difference signal of s and p polarized light modulated with a second order Bessel function $J_2(\varphi_0)$. Possible ways to correct the spectra for this term are described in the next section.

3.3.6 Experimental normalization procedure with additional polarizer

In order to compare the absorption modes of PMIRRAS spectra quantitatively it is useful to be able to perform a normalization. Buffeteau et al. [25] described a method to calibrate PMIRRAS spectra to absolute values, as they can be obtained from IRRAS spectra. They validated the theoretical results with experimental ones [25]. In addition to this normalization, artifacts introduced due to the folding with a second order Bessel function during signal demodulation Eq.3.3.21 can be removed. The basic concept of the method is a measurement of the p and s-polarized part of the PMIRRAS spectra additionally to the spectrum and calculate the IRRAS signal using the three spectra. Using the full expression of Eq. 3.3.19 and a factor $\gamma = \frac{C_p}{C_s}$ accounting for the different responses of the setup to p- and s-polarized light, the following expression for the signal S is obtained:

$$S(d) = \frac{|\gamma I_p(d) - I_s(d)| J_2(\varphi_0)}{\gamma I_p(d) + I_s(d) + [\gamma I_p(d) - I_s(d)] J_0(\varphi_0)} \quad (3.3.22)$$

By introducing a polarizer in p- and s-position, respectively, after the sample (compare to Fig. 3.3.7), only p- and accordingly s-signal are measured:

$$C_p = \frac{|J_2|}{1 + J_0} \quad (3.3.23)$$

$$C_s = \frac{|J_2|}{1 - J_0} \quad (3.3.24)$$

Using Eq. 3.3.22), 3.3.23) and 3.3.24) the ratio of the polarized intensities can be calculated:

$$\frac{\gamma I_p(d)}{I_s(d)} = \frac{C_p [C_s - S(d)]}{C_s [C_p + S(d)]} \quad (3.3.25)$$

which is an approximation of the IRRAS signal. In order to obtain the true IRRAS signal $\frac{I_p(d)}{I_p(0)}$ it has to be considered the following. Indeed, γ is close to 1 for metallic substrates and $I_s(d)$ is close to $I_s(0)$ due to the surface selection rule (compare to Sec.3.3.4), however $I_s(0)$ is slightly different from $I_p(0)$. In a second step the result in Eq. 3.3.25 have to be normalized by a signal of a bare substrate calculated in the same way, resulting in:

$$\frac{I_p(d)}{I_p(0)} = \frac{\gamma I_p(d)}{I_s(d)} = \frac{C_p [C_s - S(d)]}{C_s [C_p + S(d)]} \quad (3.3.26)$$

The only approximation which has to be made is, that $I_s(d)$ is equal to $I_s(0)$, which is virtually fulfilled for metal substrates, as argued above. Indeed a comparison of the normalized PMIRRAS spectra with IRRAS spectra show excellent agreement [25].

As later shown in Sec. 4.1.3 it is important to do both steps of the calibration procedure in order to get a adequate normalization. However, it is not necessary to measure the

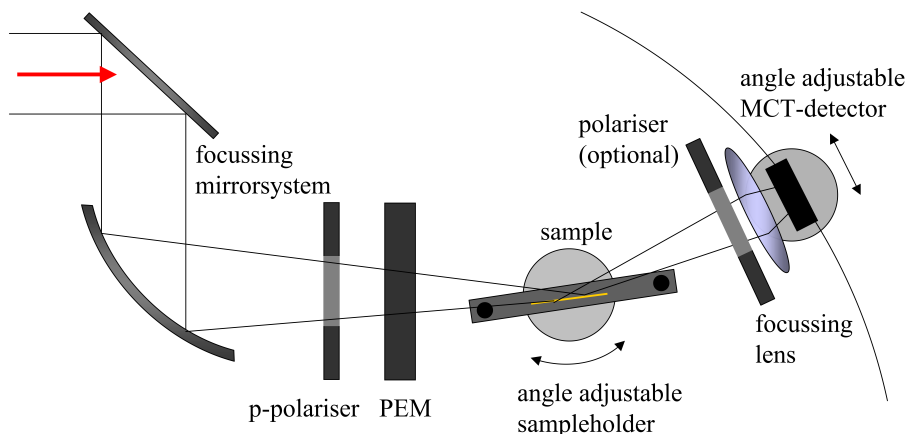


Figure 3.3.7: PMIRRAS setup. An infrared beam is coupled out of the spectrometer, polarized, phase modulated and focused on the sample. After passing the sample it is refocused on the MCT detector, a optional polarizer in between sample and detector can be used for a normalization of the spectrum.

s- and p-polarized spectra for each sample. For the measurement of thin films in air the differences in the s- and p-polarized spectra (see Eq.3.3.23 and Eq.3.3.24) in between different thin films are negligible. Only the bare substrate has to be measured in addition to the sample. Unfortunately, this method is only suitable for thin films. For *in-situ* measurements, involving the attenuation of the beam by a water layer, it is not possible to get a useful normalization.

3.3.7 Experimental setup

For PMIRRAS measurements a Vertex70 Fourier transform infrared spectrometer (Bruker, Ettlingen) is used. It is equipped with a PMA50 module (Bruker) including a photoelastic modulator (PEM), a variable angle reflection unit and a MCT detector with an angular range of 70 to 90 degrees. The infrared beam is coupled in from the Vertex 70 spectrometer, focused on the sample by a parabolic mirror and refocused in front of the detector with a ZnSe lens, compare to Fig. 3.3.7. The standard reflection unit, suitable for absorption reflection measurements in air can be exchanged with a sample holder for home-built liquid cells. The sample chamber is purged with dry, carbon dioxide free air to reduce background absorption. With PMIRRAS, absorption is measured only within the range of the evanescent field above the sample, commensurate to the wavelength of infrared light, compare to Sec. 3.3.5. The combination of both methods to reduce the background signal allows to obtain reflection absorption spectra in air without measurable background contribution.

The following settings for the PEM unit are used: Retardation was set to 0.5. The PEM frequency was adjusted in a way that it is close to the spectral region of interest, an

explanation can be found in Sec. 3.3.5. For measurements of modes in the finger print region, the PEM frequency was set to 1500 cm^{-1} , for the monitoring of modes in the CH_3 region it was set to 2900 cm^{-1} . The signal was enhanced with the lock-in amplifier in a way that the maximum signal was around 10000 - 15000 counts, well below the saturation limit of the instrument, but strong enough for a high signal-to-noise ratio. In order to optimise the spectral resolution, the signal to noise ratio and the measuring time were set to the spectral resolution to 4 cm^{-1} and 256-1024 scans were co-added depending of the adsorbate signal strength and if the samples were measured in air or under aqueous conditions. For an optimal signal, measurements in air were done at an angle of 80 degrees, measurements in water at an angle of 70 degrees, taking into account simulation results, experimental findings and instrumental limits. The angular divergence of the collimated beam is about ± 3 degrees.

For the angle dependent measurements of the PMIRRAS signal Sec.4.1.1.3 spectra were taken using a dry-air-purged Bio-Rad FTS-6000 Fourier transform IR spectrometer with polarization modulation unit. Data were collected at 20 Hz at a resolution of 8 cm^{-1} , and an under-sampling ratio (UDR) of 4 was used to improve the speed of data acquisition. To avoid aliasing, an UDR filter is placed into the optical path of the IR beam, which prevents radiation at higher wavenumbers from reaching the detector. A polarization modulator (PM) was employed, which was controlled by a Hinds Instruments PEM-90 photoelastic modulator control unit. The half-wave retardation was set at 37 kHz. The sample was placed vertically between a focusing mirror and a ZnSe lens in front of the detector. The sample was measured at incident angles ranging from 45 to 85° with respect to the surface normal of the sample.

3.3.7.1 Liquid cell

For measurements in an aqueous environment a home-built liquid cell, developed in close cooperation with the mechanical workshop is used (see Fig. 3.3.8). The sample is mounted on a height adjustable stage inside a trough, which can be filled with solution from outside via nozzles. On top of the sample is a BaF_2 hemisphere, laying on a o-ring seal and fixed with 4 screws. Importantly, the crystal is chemically not stable in water or D_2O over long times, to enhance it's stability NaF (0.1 M) was added to the solution. The effect of salt on the hydration properities of ethylene glycols is described in Ref. [71]. For *poly*(ethylene glycols) a slightly decreasing of the hydration of the EG moiety with increasing salt concentration is observed. This would suggest, that due to the adding of salt to the solution, we slightly underestimate the effect of hydration in our in-situ measurements. With the help of two bolts the cell is mounted on a stage, which can be angle adjusted and laterally adjusted to center the sample towards the beam position. Once the position is fixed it is very stable. Prior to each series of measurements the BaF_2 crystal was rinsed with EtOH, irradiated with UV light for about 2 min and stored in the UV chamber for another 20 min for further cleaning in ozone (produced by the UV-light) and cooling.

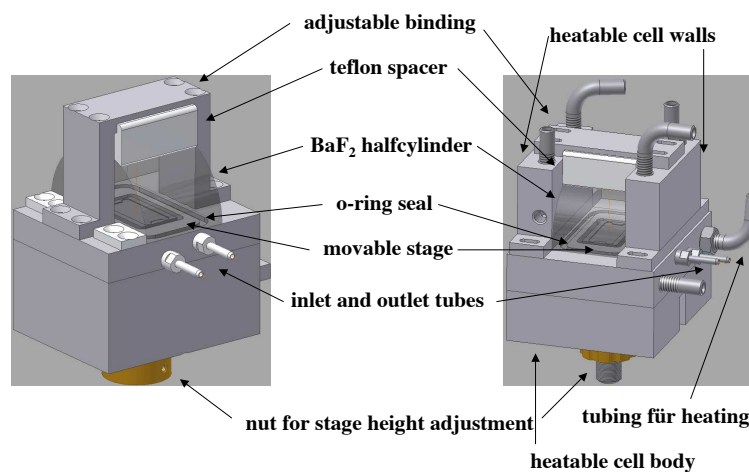


Figure 3.3.8: Sketches of of the thin liquid layer cell and the temperature controllable thin liquid layer cell. The sample is placed in between the movable stage and the barium fluoride crystal.

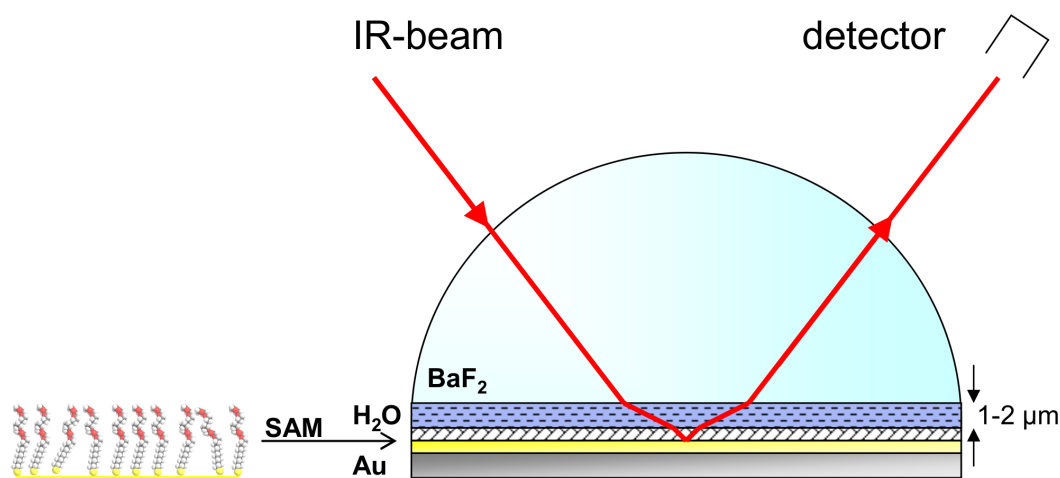


Figure 3.3.9: Optical system for PMIRRAS measurements under aqueous conditions

Two methods can be used to mount the sample. The common way, which was used for nearly all experiments, is the following. First, the height of the stage was adjusted with a test sample of the same shape as the sample. The BaF₂ hemisphere was pressed on the sample, and the stage was lowered until the crystal had enough pressure on the o-ring seal to render the cell water-proof. Then, the cell with the test sample was mounted in the spectrometer and adjusted for a maximum signal. Second, the sample was immersed with a drop of solution and the BaF₂ crystal was placed on top of the it. Excessive water was removed with the tissue and the sample was centered with respect to the crystal. Successively, the crystal with the sample was placed on top of the stage of the sample cell and fixed with four screws. To ensure optimal and equal thickness, the screws were tightened uniformly and in small steps. Finally the cell was filled with liquid and placed in the spectrometer. For time dependent measurements the second step of this procedure took about 2 minutes. Samples prepared with this procedure are very stable with respect to thickness of the liquid layer and position and suited for long term real-time measurements. There is also an alternative method of sample preparation. The sample is fixed on the sample stage with a flexible tape, and adjusted in a way that there is a gap in between sample and BaF₂ hemisphere of some millimeters. The solution is added and the crystal is mounted. Afterwards the trough is filled completely with solution and the stage is moved until the sample has contact to the crystal. With this method also very thin liquid layers are possible, however it is not as stable and reproducible as the first method.

3.3.7.2 Temperature controllable liquid cell

In order to perform temperature dependent measurements, a cell very similar to the *in-situ* cell was constructed, compare to Fig. 3.3.8. It can be temperature regulated by hot water provided from a thermostat. Since a BaF₂ half cylinder is used, which is very sensitive towards expansion, it had to be ensured that the crystal is warming up as uniformly as possible. For this purpose the bottom of the cell, which has contact to the water bath contacting the crystal and the sample was heated, as well as both sides which are pressed against the semicircular sides of the BaF₂ crystal. To ensure a optimal heat transfer as well as a protection of the crystal, soft heat transfer polymer foils in between the cell walls and the BaF₂ half cylinder are used. For the transfer of the sample into the cell one of the sides can be removed. This is possible by a flexible tubing system between the heated parts of the sample cell.

The thermostat water bath temperature can be controlled with a accuracy of 0.5 K. More important is the temperature transfer from the water bath to the sample. In order to prevent temperature losses from the thermostat to the sample cell the tubes were isolated with a heat insulator tube. Simultaneously to the measurement of the temperature of the thermostat reservoir, the temperature of the water bath in the sample cell was measured. There was no measurable difference and a latency of about 30 s in between both temperatures with a temperature gradient of 2.5°C in 5 min.

For the temperature dependent measurements the temperature of the water bath was increased in steps of 2.5 K and it was waited for 10 min to get an equilibrated system. In a measurement lasting 15 min 1024 Scans were co-added, the resolution was set to 4 cm^{-1} . The temperature range was 22 °C to 65 °C in the normal runs and 22°C to 45°C in the reversibility runs.

3.3.8 Data processing and analysis

The infrared data are acquired with OPUS software (Bruker). A procedure for Fourier transformation is included. Further data processing is done in Igor Pro (Wavemetrics Inc. Lake Oswaego, U.S.A.). Data are exported from OPUS in the comma separated value format, it can directly be loaded into Igor Pro. Note, that the data is exported with 10 decimal places. This is necessary for a reasonable accuracy when normalizing raw reflectivity or transmission data with a reference spectrum.

3.3.8.1 Baseline correction

An important issue in PMIRRAS measurement is the baseline correction. As explained in Sec.3.3.5, due to the demodulation of the polarisation modulated signal with the help of a lock-in amplifier a second order Bessel function is introduced and folded with the absorption spectra. There are different ways to get rid of this term. First, one can do a manual background subtraction with interpolation points, one has to take great care to set the interpolation points at the right position where no absorption mode should be located. Second, one can determine the Bessel function introduced by an optical setup with the help of additional measurements with a polarizer behind the sample, see Sec.3.3.6. An approach was used, combining the accuracy of the method with a second polarizer and the convenience and reproducibility of the manual background subtraction. Our first step is a normalization of the spectra with the help of a second polarizer (see Sec.3.3.6), now points in between the absorption modes supporting the baseline were determined and a baseline correction performed. As a last step a manual baseline correction with this set of supporting points was performed and the spectra were compared with the ones obtained via normalization. The supporting points were varied until normalized and the manually corrected spectra look very similar. The obtained set of pivot points is used for every dataset of the same component under the same conditions. As a result a much higher reproducibility as in case of a manual baseline correction can be achieved. Due to the obtained smooth curves (compared to relatively rough ones achieved with a normalization with a second polarizer) the Gaussian fitting of the absorption modes has a higher reproducibility.

3.3.8.2 Baseline correction for the angle dependent PMIRRAS measurements

For the angle dependent measurement of the PMIRRAS signal strength described in Sec. 4.1.1 only the intensity of the C-O-C stretching vibration was important, so a simpler approach for baseline correction was sufficient. A set of seven points at positions 1260, 1220, 1180, 1080, 1065, 1050 and 1030 cm^{-1} was used for all samples to interpolate the shape of the baseline. The interpolation points were chosen to lie well away from the peak of interest in the spectrum. This standard correction procedure was necessary for the determination of the peak intensity for different samples, especially for the in situ measurements, where the whole angle series could not be measured without refilling the liquid cell. The liquid had to be replaced after about one hour due to partial drying or air bubble formation.

3.3.9 Data analysis program multifit

The program “multifit” automates the baseline correction and mode fitting of datasets, leading to a faster and more reproducible data analysis. It has a user interface (see Fig. 3.3.10), whose functions are explained chronologically as used for processing a set of spectra.

- By pressing “load data”, the program is able to load comma separated data files (csv files) in the specified folder, the folder can be browsed in a pop up window. One can assign a name to the dataset, which is very useful if handling multiple data sets in one experiment. If the file name ends with a number, this number is written in a wave and the data files are sorted by rising numbers. This may be the time in case of a time dependent measurement. By pressing “load” the program loads all CV files in a new folder with the specified name.
- By pressing “plot” one gets a graph of the raw data. The next step is the selection of the wavenumber range which is of interest and insert a lower and an upper limit.
- Via “truncate” one can cut out this region. The next step is the automated baseline correction via splines. One can specify a wave including the supporting points and choose a subtraction of the baseline (one may also choose division). The spline is performed with the Igor command “interpolate2” and the options “/F=0 /I=3 /S=0.05 /T=2”.

The second step is the fitting of the spectral modes with Gaussians. The program uses an Igor Pro implemented extension called “multifitting”.

- Before the fitting starts one can load data as predefined start parameters for the fitting in the path of the data set, enabling its use during the fitting. Next, one selects one data set and presses the “set” button.

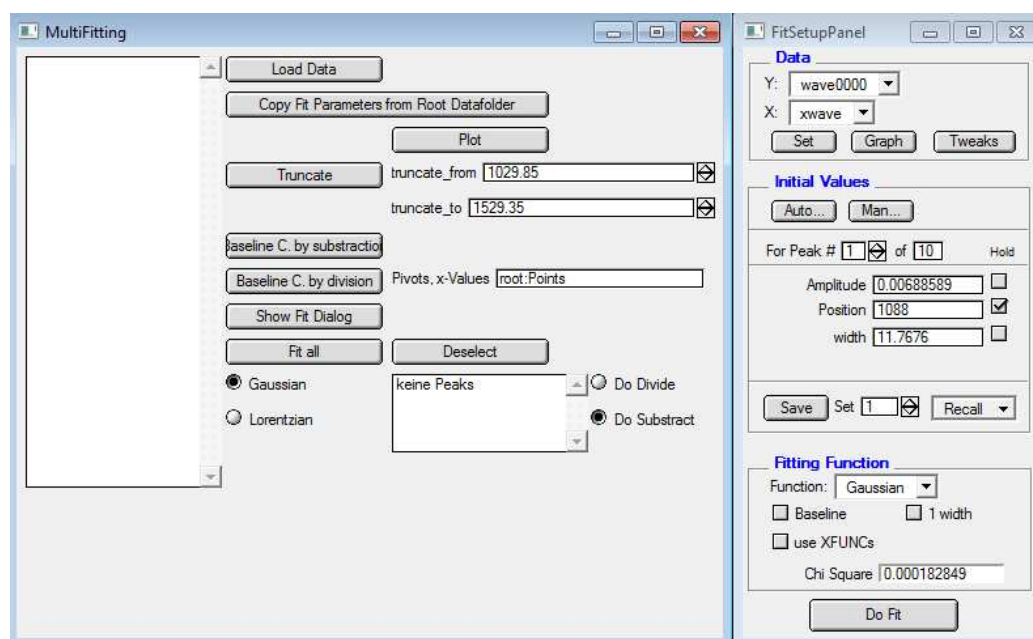


Figure 3.3.10: User interface of the data-processing program “multifit” and interface of the fitting tool, which belongs to the Igor package and can be remotely used by “multifit” after setting initial parameters

- To load predefined start parameters one can press “load data set” and choose one. This is a very convenient option, since often one has lots of datasets with very similar spectra.
- By pressing the “fit” button the data is fitted. It has proven useful to fix most of the parameters in the first fit and unlock them one after an other.
- If the fit is satisfying one can press “fit all” in the “multifit” console to fit all spectra of the dataset. The results of area, amplitude, width and position of the Gaussians are stored in the datasets folder in waves with corresponding names.

3.3.10 Plot and normalization of the fit results

For comparison with each other the results of the fitting procedure described in Sec. 3.3.6 are normalized to a arbitrary value. That may be the first spectra for long time studies or a average of the last 5 spectra for growth experiments. In case of amplitude, area

and width results are normalized by division in case of position they are normalized by subtraction. The normalized results are plotted and in case of a systematical behaviour (for example exponential increase) a fit can be performed with the analysis tool in Igor Pro.

3.4 X-ray reflectivity

3.4.1 Theoretical background

X-rays belongs to electromagnetic waves, so the theoretical considerations in Sec. 3.3.4 can be transferred to X-ray reflectivity. However, the energy range of X-rays is much higher than the one of light, resulting in different properties regarding refractive indices. Electromagnetic waves interact with matter predominantly via electronic transitions, covering a large energy range. In the case of X-rays, yielding a high energy, there is an interaction with the inner K- and L-shell electrons. In contrast to visible light the refractive index of matter is less than unity, resulting in a total external reflection for reflectivity on the boundary vacuum-matter at angles below the critical angle. The refractive index is defined as

$$n = 1 - \delta + i\beta \quad (3.4.1)$$

The real part describes the dispersion, it depends on the electron density ρ , the scattering amplitude per electron r_0 and the wave vector $k = \frac{2\pi}{\lambda}$. The real part of the refractive index is close to 1, typical values of δ are in the order of 10^{-6} [72]:

$$\delta = \frac{2\pi\rho r_0}{k^2} \quad (3.4.2)$$

Using Snell's law (Eq.3.2.7) the critical angle can be calculated:

$$\alpha_c = \sqrt{2\delta} \quad (3.4.3)$$

The imaginary part of Eq. 3.4.1 denotes the absorption, usually β is much smaller than δ :

$$\beta = \frac{\mu}{2k} \quad (3.4.4)$$

It is useful to calculate with wave vectors instead of angles. The wave vectors of the incoming and the reflected beam k_{in} and k_{out} are spanning the vector of the out-of-plane momentum transfer Q :

$$Q = 2k \sin \alpha \quad (3.4.5)$$

By normalizing Q with the corresponding value at the critical angle Q_c , one gets the dimensionless value q :

$$q = \frac{Q}{Q_c} \quad (3.4.6)$$

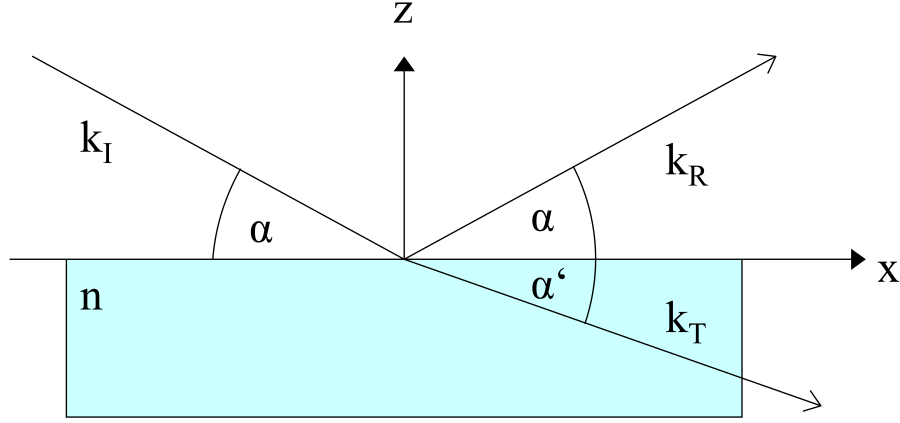


Figure 3.4.1: X-ray reflection and refraction at phase boundary. k_I and k_R are the incoming and reflected beam enclosing the angle α with the surface and k_T is the refracted beam with the angle α' .

With the help of Snell's law and the Fresnel equations (Eq. 3.3.4) one can calculate the transmission and reflection of one layer [72]. Note that the angle α is spanned by the incident beam and the plane of the substrate (Fig. 3.4.1) in contrast to the angle θ used in Sec. 3.3.4 which is spanned between the incident beam and the surface normal (Fig. 3.2.1). Therefore, in the corresponding equations sine has to be substituted by cosine and cosine by sine:

$$r(q) = \frac{q - q'}{q + q'} \quad (3.4.7)$$

$$t(q) = \frac{2q}{q + q'} \quad (3.4.8)$$

$$q^2 = q'^2 + 1 - 2ib_\mu \quad b_\mu = \frac{2k}{Q_c^2} \mu \quad (3.4.9)$$

From these considerations one can determine that for the normalized $q \gg 1$ the reflectivity coefficient $r(q)$ is proportional to $(2q)^{-2}$, leading to a decline of the reflectivity approximately proportional to $(2q)^{-4}$.

Based on the Fresnel formulas one can also calculate the reflectivity of a slab of finite thickness on the substrate. Light transmitted through the first interface can be reflected at the second interface. Back at the first interface it can be transmitted or reflected again. Considering the contribution of all possible series of such reflections to the reflectivity one gets:

$$r_{slab} = \frac{r_{01} + r_{12}p^2}{1 + r_{01}r_{12}p^2} \quad (3.4.10)$$

with the reflectivity r_{ij} denoting the reflectivity at the associated interface and the phase factor $p^2 = \exp(iQ_1\Delta)$ [72]. The corresponding reflectivity curve displays oscillations with

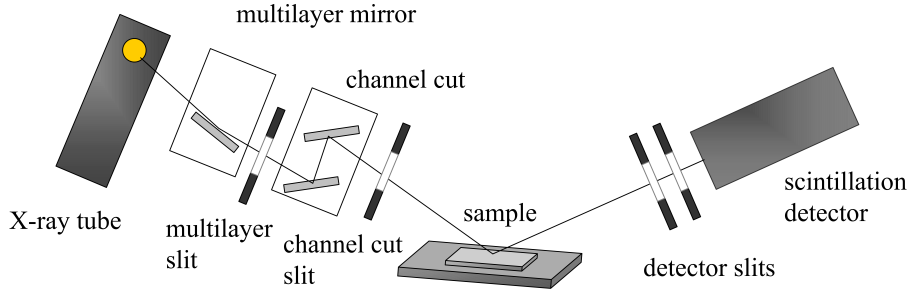


Figure 3.4.2: Schematic of a X-ray reflection setup. The X-rays are monochromated and parallelized by a multilayer and a channel-cut and detected with a scintillation detector after passing the sample.

equidistant minima called Kiessig fringes. By measuring the distance between the minima Δq one can determine the thickness of the slab:

$$d = \frac{2\pi}{\Delta q} \quad (3.4.11)$$

The calculation of the reflectivity of a multilayer system needs a more sophisticated approach. Suitable are the kinematic approximation for normalized q-values well over 1 and Parratt's recursive method. For our calculations a program based on the Parratt method [73, 74] was used. In the considerations above, the assumption of a perfectly flat substrate is made, real samples have a certain roughness. Due to a root-mean square surface roughness σ (rms roughness) the Fresnel coefficient is changed to:

$$r_{rough} = r_{flat} \exp(-Q_z^2 \sigma^2)$$

Diffuse scattering adds a broad contribution to the sharp specular reflectivity centered at the position of equal angles of incident and reflected beam. In order to correct reflectivity curves experimentally for diffuse scattering, one can measure the diffuse reflectivity at the boundary of the specular reflectivity. To this end the detector is placed at an angle slightly larger or smaller than the incident angle and the measured reflectivity is subtracted from the reflectivity signal at equal angles. More details can be found in the literature [72, 75].

In addition to the measurement of thin layers at higher q-values one can measure the atomic spacing d of the crystal lattice according to Bragg's law:

$$m\lambda = 2d \sin \theta \quad (3.4.12)$$

3.4.2 Experimental setup

The X-ray reflectivity measurements were performed using a two-circle X-ray reflectometer (XRD 3003 TT, Seifert Analytical X-ray, Ahrensburg, Germany) with a copper anode and an NaI scintillation counter, see Fig. 3.4.2 for a scheme of the setup. A Ni/C multilayer

mirror and a germanium channel-cut crystal give a monochromatic and parallel beam with $\lambda = 1.54 \text{ \AA}$ (Cu $K_{\alpha 1}$). The chosen slits resulted in an angular resolution of $\sim 0.01^\circ$. A dynamic range of more than seven orders of magnitude can be covered with automatic beam attenuators. The data was measured in air.

3.5 Grazing incidence X-ray diffraction

3.5.1 General remarks

Grazing incidence X-ray diffraction (GIXD) is a well suited method for the determination of the atomic or molecular structure of surfaces. Since the measurements are made at angles below the critical angle, the beam is totally reflected and due to the evanescent field exhibits a very small penetration depth, rendering it very surface sensitive. In X-ray reflectivity measurements the q_z momentum transfer is along the specular path, providing information about the out-of-plane structure of the sample. For grazing incidence X-ray scattering experiments, however, the momentum transfer is mostly in (q_x, q_y) direction is measured, containing information about the in-plane periodicity of the sample. Due to the small number of scatterers on the surface, intense X-ray sources as synchrotron X-ray facilities are highly desirable for this kind of experiments. The measurements are particularly sensitive to periodic surface structures, disordered areas only contribute to the diffuse scattering. Weak in-plane reflections can only be found when the background noise from the bulk crystal is featureless [76].

In the following paragraph a brief quantitative understanding of the penetration depth should be provided. As already pointed out in Sec. 3.4.1 the refractive index for X-rays is in most materials slightly smaller than in air. Therefore, at the air-substrate interface total reflection occurs, if the angle of incidence is below the critical angle. This is accompanied by an evanescent wave travelling along the interface and damped exponentially in direction to the surface normal. The critical angle can be calculated with Eq. 3.4.3. With the angle of incidence α_1 , the critical angle α_c , the wave vector k and the absorption coefficient β the penetration depth Λ_1 can be expressed as [76]:

$$\Lambda_1 = \left\{ 2k^2 \left[\sqrt{(\alpha_1^2 - \alpha_c^2) + 4\beta^2} + \alpha_c^2 - \alpha_1^2 \right] \right\}^{-\frac{1}{2}} \quad (3.5.1)$$

Note, that the penetration depth is very small for $\alpha_1 < \alpha_c$ and is strongly rising above α_c , this can be used to suppress diffuse thermal scattering from the bulk crystal. The amplitude of the refracted wave E'_1 is given by:

$$E'_1 = T_1 E_1 \quad (3.5.2)$$

It is a function of the amplitude of the incoming wave E_1 and the transmission coefficient T_1 , which shows - plotted as a function of angle of incidence - a maximum at the critical

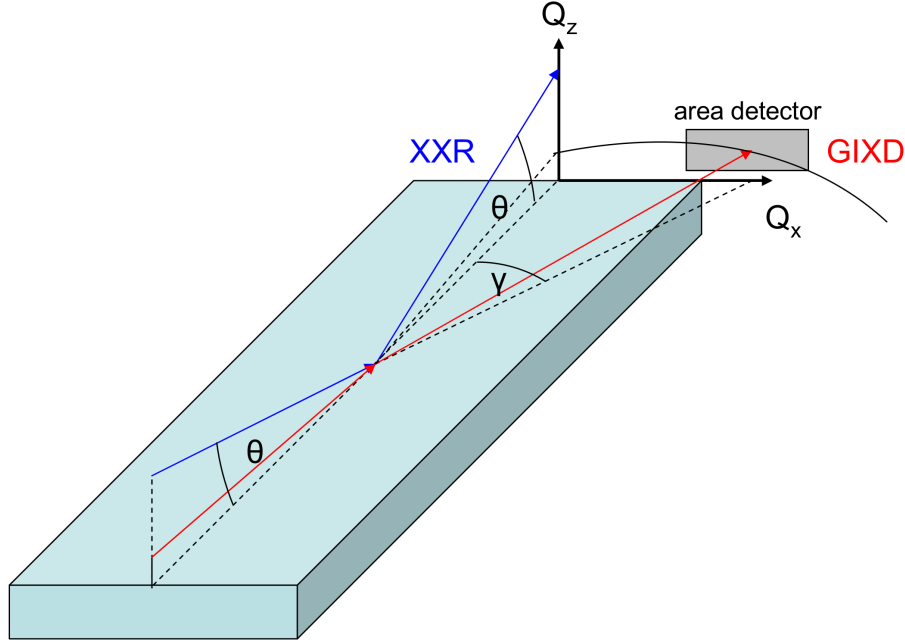


Figure 3.5.1: Schematic setup for the GIXD in-plane measurements

angle. This can be explained with the standing wave phenomena: At the critical angle incoming and total reflected wave are in phase, leading to a doubling of the amplitude and neglecting absorption a fourfold surface signal. Therefore, the optimum signal-to-noise ratio of the surface signal can be obtained, when the angle of incidence α_1 equals the critical angle α_c . In experiment, however, a angle slightly below the critical angle is chosen. Since above the critical angle the surface signal is decreasing dramatically, a small misalignment of the angle would have significant impact on the signal strength. For a more details see Ref. [76]

3.5.2 Experimental setup

The in-plane grazing incidence X-ray scattering experiments were performed at the beamline I07 at the Diamond synchrotron facility, a scheme of the setup is shown in Fig. 3.5.1. For the experiments a slit configuration with the vertical slits after the source and before the detector at 0.8 mm and the horizontal slits at 0.6 mm was used. The measurements were performed in air and at an energy of 20 keV. A Pilates100k area detector was used with $487 \times 195 = 94,965$ pixels, each sized $172 \mu\text{m} \times 172 \mu\text{m}$ summing up to an overall area of 83.8 mm x 33.5 mm. The angle of a peak in q_x direction, was calculated as the sum of the detector angle in q_x direction γ and the distance of the measured peak from the detector center in horizontal direction, where N is the pixel position:

$$\gamma = \gamma_{det} + \arctan \frac{(N - 244) \cdot 0.172\text{nm}}{L} \quad (3.5.3)$$

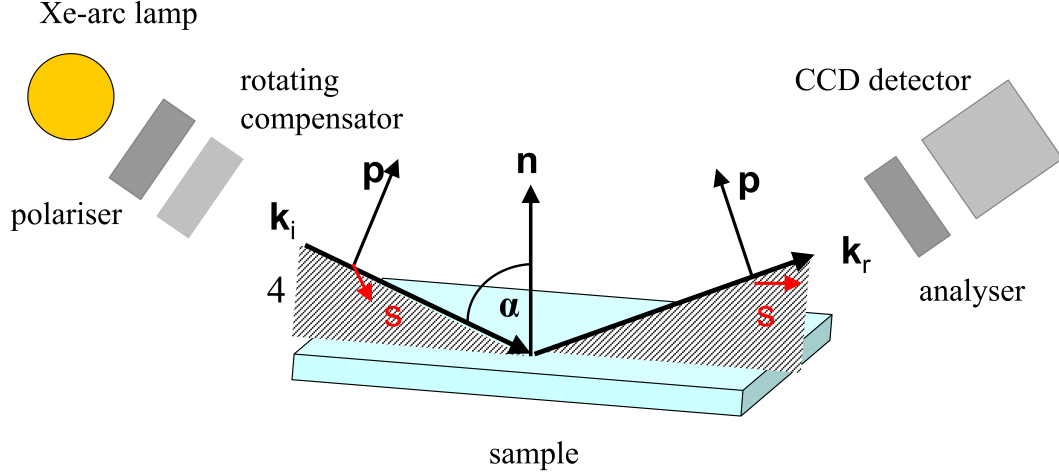


Figure 3.6.1: Schematic of ellipsometry setup

The distance between sample and detector L was approximately 1200 mm, for an exact determination the position of the Au (222) q_x reflection was used. The q values can be obtained from:

$$q = \frac{4\pi}{\lambda} \sin \gamma \quad (3.5.4)$$

where λ is the X-ray wavelength and γ the angle in q_x direction.

3.6 Spectroscopic ellipsometry

Spectroscopic ellipsometry is a method to determine optical constants or thickness of layers from a few Angstroms up to some 100 nanometers. It uses the effect that the reflectivity of light at interfaces in between layers with different dielectric constants depends on its polarisation. Therefore, the effective polarisation of light is changed when passing a sample, which can be measured [77]. The Fresnel reflection coefficients in Eq. 3.2.8 and Eq. 3.2.9 are related to the ellipsometric angles Δ and ψ by Eq. 3.6.1:

$$\frac{r_p}{r_s} = \exp(i\Delta) \tan \psi \quad (3.6.1)$$

To determine the dielectric constants from the ellipsometric angles the equation has to be solved numerically, either by a so called point-by-point fit, optimising the dielectric constants separately for each wavelength or with the help of analytical functions, whose parameters are optimized for a specific energy range. The data are analyzed with the software WVASE, compare to [78]. For further details see [77, 79].

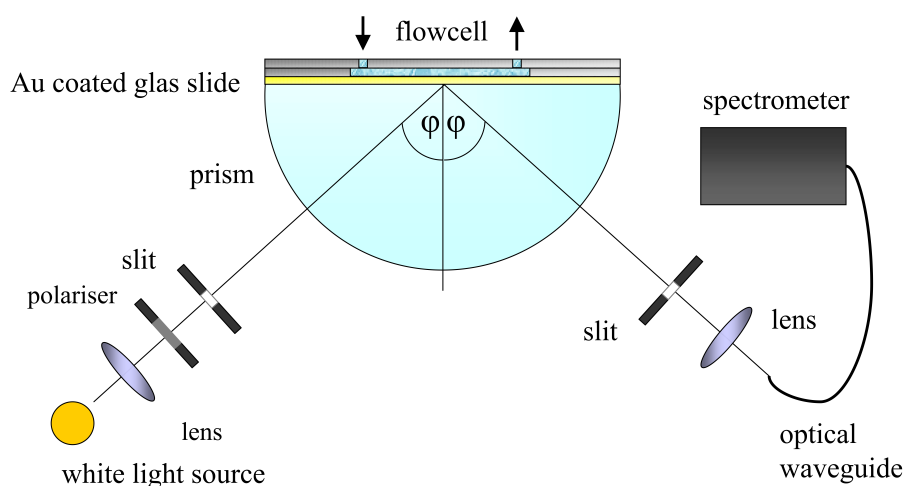


Figure 3.7.1: Scheme setup surface plasmon resonance

3.6.1 Experimental Setup

The data are measured with a Woollam M-2000 Rotating Compensator ellipsometer. The white light of the Xe-arc lamp is linearly polarized and further modified by a rotating analyser. After reflection from the sample the light passes a polarizer, the so-called analyser and is measured by a CCD detector (see Fig. 3.6.1). The ellipsometer is mounted on a Woollam goniometer which can be controlled regarding position and angle with the WVASE software. The spot size on the sample is dependent of the angle of incidence, at angles of about 60 degrees it is around 10 mm^2 . After each initialising of the system a calibration procedure is performed using a Si(100) reference wafer with a thermal oxide layer of 20 nm. For further details see [79].

3.7 Surface plasmon resonance

Surface plasmon resonance (SPR) is a highly surface sensitive method detecting changes of refractive indices. It can be used to monitor very precisely adsorption and chemisorption of thin layers on surfaces, which renders it to an established method to monitor biomolecular interaction at interfaces. Surface plasmons are vibrations of surface charges at the interface of a metal and a dielectric. The associated electromagnetic field is totally reflected from both layers and attenuated exponentially in both layers, it is a so-called evanescent field. Its interaction with the media within a small range makes the surface plasmons sensitive for changes in the dielectric constants inside this range. A very common setup for SPR measurements is the so-called Kretschmann configuration. Light polarized parallel to the plane of incidence (p-polarized, compare to 3.2 is totally reflected at the interface of the prism and the metal layer. The penetrating evanescent field induces surface plasmons at the interface of the metal layer with the analyte, compare to Fig. 3.7.1.

The resonance frequency of the surface plasmons is a function of the angle of the incident light, the dielectric constants of the prism and the metal layer and importantly of the dielectric function of the analyte close to the metal surface. One can derive the resonance conditions from the Maxwell equations, considering energy- and momentum conservation and the boundary conditions [80]:

$$\sin \theta \sqrt{\epsilon_1(\lambda)} = \sqrt{\frac{\epsilon_{2,re}(\lambda)\epsilon_3(\lambda)}{\epsilon_{2,re}(\lambda) + \epsilon_3(\lambda)}} \quad (3.7.1)$$

At the resonance position the incident light is exciting the surface plasmons, resulting in a attenuated reflection. Analyte adsorption leads to a change of the dielectric constants and to a shift of the resonance peak. There are two common methods for monitoring the resonance peak. First, one can excite surface plasmons with monochromatic light and vary the angle to find the minimum of the reflected light and, second, one can excite surface plasmons with white light, measure the spectrum after the sample with a spectrometer and monitor at which wavelength the lowest reflection occurs. For a more detailed description see [80–82].

3.7.1 Experimental setup

For the measurements a home-built setup, using a white light source (560 nm to 720 nm) and the Kretschmann configuration (compare to Fig. 3.7.1) is used, for details see [80]. The shift of the resonance frequency can be evaluated either by monitoring the position of the resonance peak or the intensity of the reflected light at one fixed frequency at the slope of the resonance peak, for our measurements the resonance peak position is calculated from a fit over the values in the vicinity of the resonance peak. Gold coated glass slides were pressed on the prism, using immersion oil to bridge the gap without changing the refractive index. For an optimal signal-to-noise ratio, the gold layer has a thickness of 50 nm (compare to [81]). Since the penetration depth of the evanescent field from the surface plasmons in the analyte is in the order of the wavelength of the exciting light and a analyte layers of only a few nanometers is monitored, a linear dependence of the thickness of the adsorbed analyte and the shift of the resonance peak is assumed (compare to [81]). For further details of the setup see Ref. [80].

3.8 Complementary techniques

Additionally to the technique above, the following techniques have been applied from our cooperation partners from the Max Planck institute for metal research in Stuttgart for the characterisation of thin SiO_x layers deposited on titanium substrates.

3.8.1 Electron microscopy

A transmission electron microscopy (TEM) specimen was prepared using the conventional cross-section method. Unidirectional ion milling from the substrate to the film was performed using a low-angle ion milling and polishing system at 4 keV (Model 1010, E.A. Fischione Instruments Inc., Export, U.S.A.). Final polishing was performed at 0.5 keV. During the ion-milling process, the specimen was cooled with liquid nitrogen. Conventional TEM was performed using a JEOL JEM 4000 FX (JEOL Ltd., Tokyo, Japan) operated at 400 keV. Analytical TEM studies were carried out in a VG HB501UX dedicated scanning transmission electron microscope operated in ultra-high vacuum at an accelerating voltage of 100 keV. The beam current was 0.12 nA for a beam diameter of 0.7 nm (full width at half maximum (FWHM)). This microscope has a cold field emission source and is equipped with an energy-dispersive X-ray spectrometer (Noran System SIX, Thermo Fischer Scientific, Waltham, U.S.A.) and an electron energy-loss spectrometer (EELS) (Gatan UHV Enfina system, Gatan Inc., Pleasanton, U.S.A.). The energy resolution of the whole system was approximately 0.6 eV as determined by the FWHM of the zero-loss peak at a dispersion of 0.1 eV/channel. For a detailed description of TEM see Ref. [83, 84].

3.8.2 X-ray photoelectron spectroscopy (XPS)

X-ray photoelectron spectroscopy was carried out using non-monochromated Mg K_{α} (1256.6 eV) X-rays from a Dual-Anode X-ray Source (Physical Electronics Inc., Chanhassen, U.S.A). Photoelectrons were detected using a hemispherical energy analyzer (Phoibos 150 from Specs GmbH, Berlin, Germany). All measurements were performed in normal emission geometry, at a vacuum of $\sim 5 \times 10^{-10}$ mbar. Peaks to be quantified were fitted, after subtraction of a Shirley background, with the following Gaussian-Lorentzian product formula:

$$GL(x, F, E, m) = \frac{\exp(-4 \ln 2(1 - m) \frac{(x-E)^2}{F^2})}{1 + \frac{4m(x-E)^2}{F^2}} \quad (3.8.1)$$

where x is the binding energy, E is the peak position in binding energy, F the peak width and m , which controls the relative weight of Gaussian and Lorentzian character, was fixed at 0.1 throughout. For a detailed review see Ref. [85]

Chapter 4

Results and discussion

In this chapter the experimental results are presented and discussed in detail. The focus of this work was on the characterization of the growth and the properties of Eg₆OMe thiol SAMs in solution. In the first part of this chapter technical developments are described which expand the possibilities of PMIRRAS and are the basis for the experiments described successive part of the results. In Sec. 4.1 a method to simulate the intensity of the PMIRRAS signal is shown. The results are verified experimentally. In the next part, Sec. 4.1.2 a new method is shown to calculate the thickness of the water layer above the sample when measuring under aqueous conditions. The new approach is compared with two established methods. In Sec. 4.1.3 a normalization procedure converting PMIRRAS spectra into IRRAS spectra is showed. The method is experimentally tested and compared for different substrates. The methodical part is completed with Sec. 4.1.4 comprising the characterization and application of a novel layered substrate enabling PMIRRAS measurements on dielectric substrates.

The main part of this chapter focuses on *in-situ* measurements of Eg₆OMe SAMs. In Sec. 4.2 the growth of Eg₆OMe thiols on Au is studied in solution and in real time. Spectral modes in the fingerprint region comprising the spectral range from 1000 cm⁻¹ to 1500 cm⁻¹ are identified and analyzed regarding area, amplitude, position and width. Moreover the influence of the surrounding water molecules are investigated and spectra of SAMs with different surface coverage are compared in air and in aqueous environment. In Sec. 4.3 different approaches to estimate the coverage of OEG SAMs are compared. First, Eg₆OMe SAMs growth is monitored with SPR and the infrared spectra of the so produced complete and partially grown SAMs are compared. Second, after immersion of substrates in Eg₆OMe thiol solution for varying times, the substrates are immersed in amide thiol solution. The strength of the amid modes are compared with Eg₆OMe absorption modes. In Sec. 4.4 the longterm behaviour of Eg₆OMe SAMs is monitored under different conditions. The spectra of SAMs stored in air and illuminated with natural light are compared to SAMs stored in the dark in air and SAMs stored in the dark in solution as a function of time. Moreover the impact of multiple drying and reimmersion

cycles and temperatures higher than 50 °C are studied. In the last part of this chapter, Sec. 4.5, the influence of elevated temperature is investigated for SAMs in solution as a function of temperature and surface coverage. To analyse the effect of the interaction with water the results were compared with measurements in air.

4.1 Technical development of the PMIRRAS method

The first part of the results chapter focuses on the technical development of the PMIRRAS method. The simulation of the strength of the PMIRRAS signal and the novel substrates enabling PMIRRAS measurements on dielectric substrates are useful for measurements in air and in aqueous conditions. In contrast, the normalization procedure of PMIRRAS measurements can only be applied on measurements on air and the calculation of the thickness of the water layer can be used for measurements *in-situ*.

4.1.1 Simulation and optimization of PMIRRAS signal strength

In this section the calculation and optimization of the PMIRRAS signal strength is shown. Additionally, the calculations are verified with experimental results measured in solution and in air over an angular range from 50 ° to 80.5 °. The results are published in Ref. [23] and the following part is taken from this manuscript.

4.1.1.1 Mathematical framework and implementation

The propagation of electromagnetic waves through stratified media has been discussed in detail in the literature [86–88]. The present calculation uses the formalism and notation used by Hansen [24]. The basic implementation was obtained from Corn’s group [89] and was extended to describe a four-layer system including s- and p-polarized light. From the resulting reflectivity for the whole stack, the PMIRRAS difference signal was computed (Eq. 4.1.1) in order to compare these calculations with actual experimental data:

$$\frac{\Delta R}{R} = \frac{\Delta I_{sample}}{\langle I \rangle_{ref}} \approx \frac{I_p^{det} - I_s^{det}}{I_p^{det} + I_s^{det}} J_2(\phi_0) \quad (4.1.1)$$

In Eq. 4.1.1 I_{sample} is the measured signal, $\langle I \rangle_{ref}$ is the reference signal, $I_{s,p}^{det}$ are the recorded signals for p and s polarized light, respectively and $J_2(\phi_0)$ is the second order Bessel function. The detected PMIRRAS intensity depends on the cosine of the photoelastic modulator (PEM) phase ϕ . This phase in turn depends on the PEM frequency ω . The PMIRRAS signal containing a $\cos(\phi_0 \cos(\omega))$ term can then be expanded in terms of Bessel functions. Bessel functions of orders higher than two can usually be neglected. The Bessel function was thus not included in the calculation, since the experimental spectra can be corrected without major problems and the implicit Bessel function removed,

for instance by manual baseline correction or subtraction of a reference spectrum. For an interesting discussion of some issues related to the signal generation of this type of modulation see, e.g. Ref. [90].

On the basis of the calculations described in Sec. 3.2 and Sec. 3.3.5 the reflection of p- and s-polarized light can be derived and further the PMIRRAS signal can be calculated. The reflection coefficients r_s (Eq. 3.2.22) and r_p (Eq. 3.2.21) for the entire stack are then used to compute the PMIRRAS signal r_{calc} (see also Eq. 4.1.1):

$$I_{s,p} = R_{s,p} = |r^{s,p}|^2 \quad (4.1.2)$$

$$r_{calc}(\theta) = \frac{I_p - I_s}{I_p + I_s} \sim \left(\frac{\Delta R}{R} \right)_{exp} \quad (4.1.3)$$

The final signal is obtained by calculating the relative reflectance of the sample. This is given by the ratio of the reflectance of the stack with SAM to that without it:

$$I_{calc}(\theta) = \frac{r_{calc}^{SAM}}{r_{calc}^{noSAM}} \quad (4.1.4)$$

The Igor Pro code plots r_s and r_p for the entire stack and the total PMIRRAS signal I_{calc} . The software can calculate these quantities as a function of angle for fixed thicknesses of SAM and water layer, or the signal can be evaluated at a given angle as a function of the thickness of either SAM or water layer. The resulting functions are very helpful for the determination of the ideal experimental conditions regarding optimum angle of incidence and the impact of the thickness of the water layer. In addition, the optical constants for H₂O and D₂O, which vary considerably in the mid-infrared region, can be automatically loaded from the tabulated values of Bertie et al. [91]. The refractive index of the BaF₂ half cylinder is calculated using the following Sellmeier approximation [92]:

$$n_{BaF_2}^2 = 1 + \frac{0.643356\lambda^2}{\lambda^2 - 0.57789^2} + \frac{0.506762\lambda^2}{\lambda^2 - 0.10968^2} + \frac{3.8261\lambda^2}{\lambda^2 - 46.3864^2} \quad (4.1.5)$$

This approximation is valid at 25°C in the wavelength range of $\lambda = 37707.4 - 966.5 \text{ cm}^{-1}$. The optical constants of gold were taken from [93].

4.1.1.2 Optimization of experimental parameters

Some examples are shown to illustrate the importance of the choice of incident angle and thickness of the water layer for the system which was investigated in our previous letter by using PMIRRAS. Samples presenting a hexa(ethylene glycol) (Eg₆OMe) terminated SAM were used as a model system in this study. The fingerprint region of a characteristic in situ spectrum, i.e. a spectrum taken through a thin ($\sim 1 \mu\text{m}$) water layer, is shown in Fig.4.2.1. The typical shape of reflectivity curves for the present four-layer system is a smoothly rising curve with a broad peak at angles higher than 50°, which falls rather abruptly to

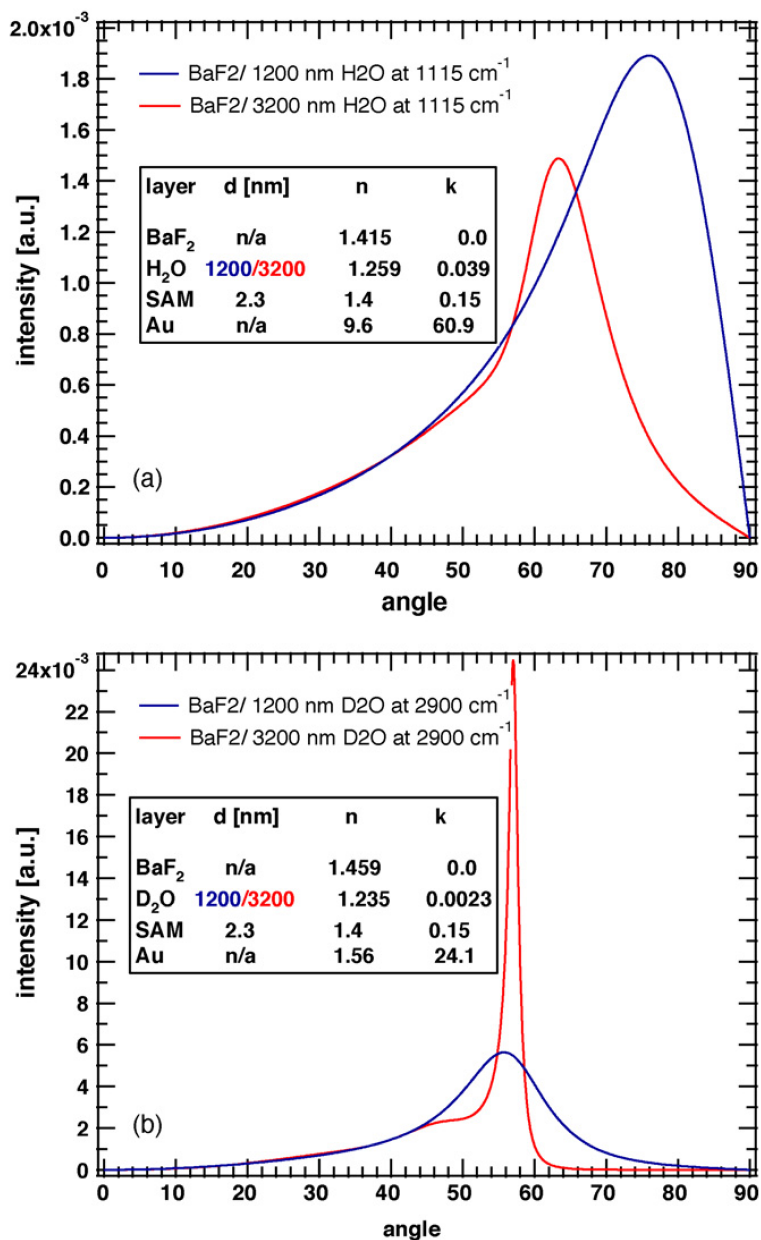


Figure 4.1.1: (a) Simulation of the C-O-C peak intensity at 1115 cm^{-1} for a four-layer system consisting of barium fluoride, H₂O, monolayer and gold substrate (optical constants are shown in the inset). (b) Simulation of the C-H peak intensity at 2900 cm^{-1} for a four-layer system consisting of barium fluoride, D₂O, monolayer and gold substrate (optical constants are shown in the inset). The blue lines denote a water thickness of 1200 nm, while the red line represents 3200 nm of water.

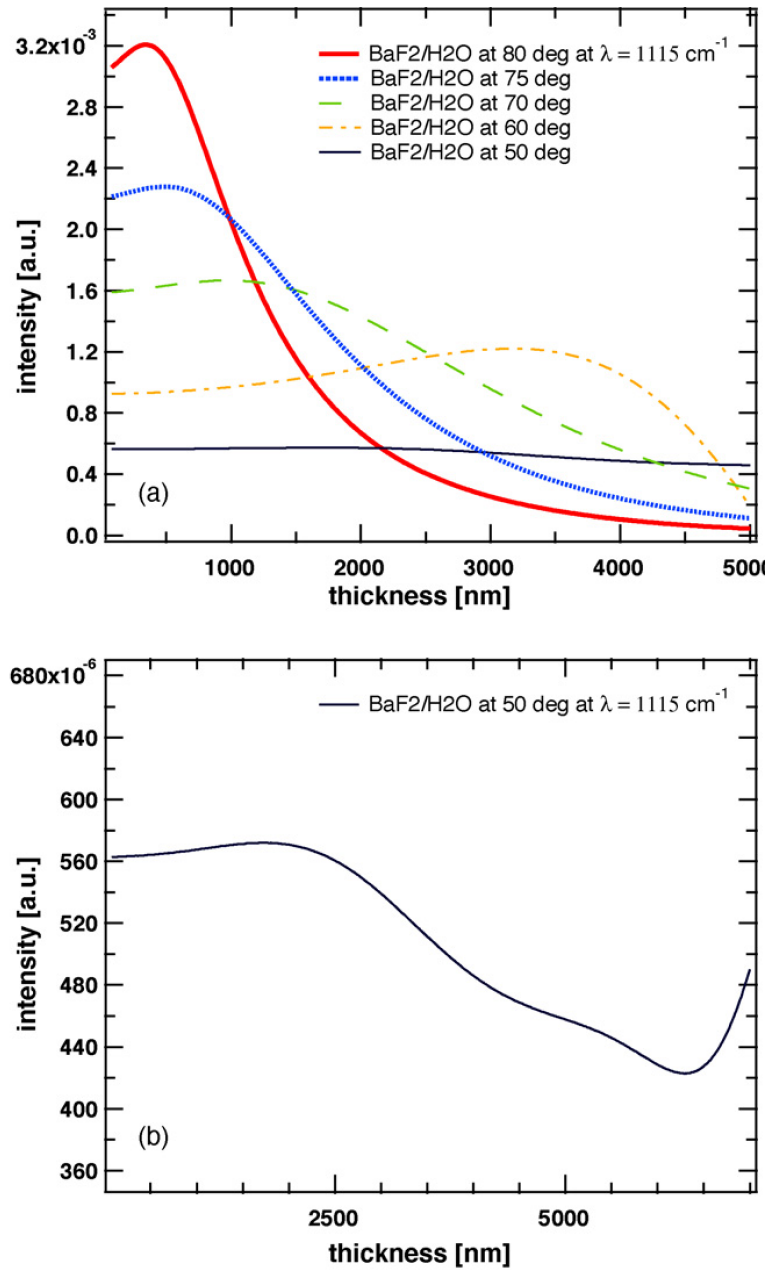


Figure 4.1.2: (a) Simulation of the C-O-C peak intensity at 1115 cm^{-1} for a four-layer system consisting of barium fluoride, H₂O, monolayer and gold substrate for different, but fixed incident angles as a function of thickness of the water layer. (b) Detailed view of the plot for 50° .

zero at 90° . However, the position, width and relative height of the peak strongly depends on the thickness of the water layer sandwiched between the barium fluoride half-cylinder and the sample. Whereas for relatively thin layers of H_2O , i.e. around 1000 nm, the peak is rather broad, centered at around 75° , the situation changes if the water layer becomes thicker (3000 nm). Then the peak becomes much sharper and shifts towards lower angles. This means that the observed intensity of the IR absorption band (e.g. that of the C-O-C stretching vibration) can vary by a factor of up to seven between an angle of incidence of 80° compared to the optimum angle at 63° (Fig.4.1.1a). A more dramatic effect can be observed for D_2O due to its difference in refractive index compared to the barium fluoride in the CH stretching region. If absorption peaks in the CH region (around 2900 cm^{-1}) are measured, then a variation of the thickness from 1200 to 3200 nm can lead to a strong drop in the signal at angles away from the optimum angle at around 58° , as shown in Fig.4.1.1b. This behavior is caused by the difference in refractive index, which leads to total reflection between the BaF_2 half-cylinder and the water layer (the exact critical angle varies with wavelength). However, due to the relatively high imaginary part of the refractive index (equivalent to the absorption coefficient) for H_2O at 1115 cm^{-1} , the electromagnetic wave can still propagate into the water beyond the critical angle. In contrast, the absorption coefficient for D_2O at 2900 cm^{-1} is very small, and there is only the evanescent wave present at angles higher than the critical angle. Even in this case the intensity does not vanish immediately, since the evanescent field penetrates to depths of the order of the wavelength (i.e. a few micrometers) into the water. Finally, the peak intensity can be plotted for a fixed angle as a function of the thickness of the water layer. An overview of the results is shown in Fig.4.1.2. The absorption peak intensity drops strongly with the thickness of the water layer at angles much larger than the critical angle. The intensities are almost constant for angles smaller than the critical one, and show an oscillatory behavior in the simulations. This is due to interference effects, when the thickness is of the order of the wavelength of the light. This effect is small even in the calculations, and it is not expected to be present in actual experiments due to roughness of half-cylinder and sample, and also due to potential misalignment (i.e. the water layer is not a slab of constant thickness, but has rather a wedged shape as a consequence of the inevitably imperfect mechanical assembly).

4.1.1.3 Comparison of calculations and experiments

In order to validate the simulations and compare them with experimental data, a systematic study of the angular dependence of the PMIRRAS was performed. With this setup it was possible to access angles between 40° and 90° using the liquid cell (Fig.3.3.8). The EG_6OMe sample was measured in air (Fig.4.1.3). The peak heights were determined and compared to the calculated values. The measured values were only multiplied by a constant factor to account for the efficiency of the optics in the experimental setup. As can be seen from Fig.4.1.4, the measured values are in excellent agreement with the calculated curve. The data points at angles higher than about 80° are slightly lower than

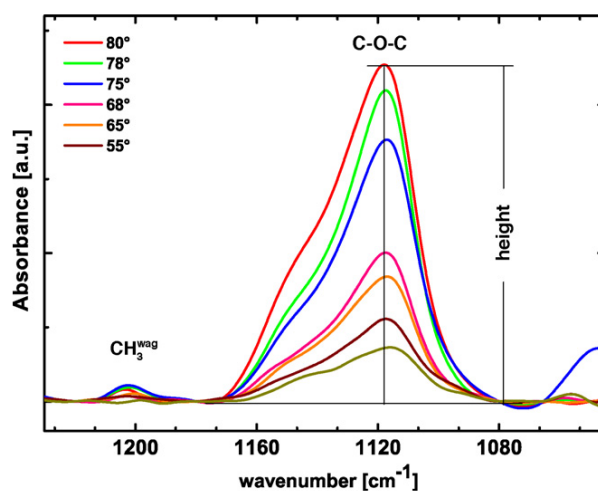


Figure 4.1.3: Measured C–O–C peak heights for various angles on an EG₆OMe coated SAM in air.

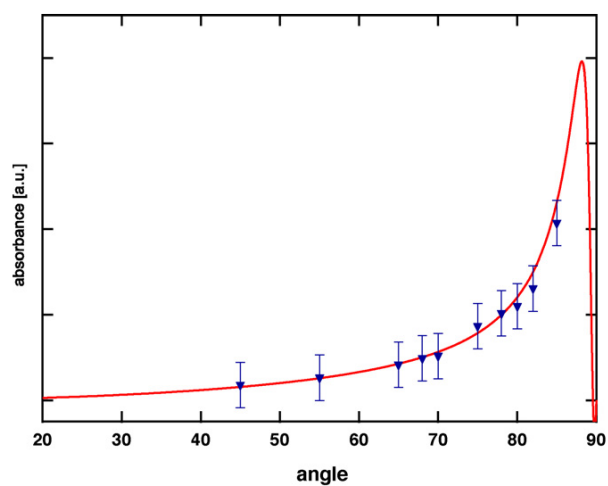


Figure 4.1.4: Comparison of calculated (solid red line) and measured (blue triangles) reflectivities for various angles of the characteristic C–O–C absorption band of an EG₆OMe coated SAM in air. The calculation was performed at 1118 cm⁻¹.

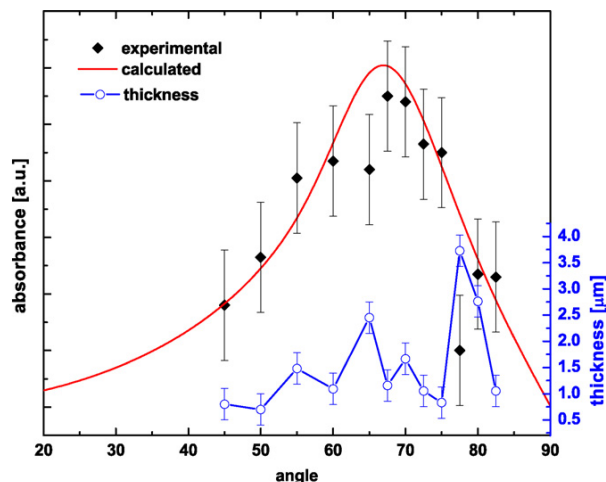


Figure 4.1.5: Comparison of calculated (red solid line) (at 1118 cm^{-1}) and measured (black diamonds) reflectivities for various angles of the characteristic C–O–C absorption band of an EG₆OMe coated SAM in a 0.1M H₂O/NaF solution. The red line is the PMIRRAS calculation for a four-layer stack with optical constants listed in Table 1 at 1118cm^{-1} . The blue solid line with open circles denotes the actual measured thickness of the water layer for each angle.

the calculated curve. This can be explained by the large size of the footprint of the beam compared to the sample at grazing angles, as was verified in measurements with differently sized samples. If the sample is sufficiently long in the direction of the beam, then the overspill can be minimized or even eliminated and the data points are commensurate with the calculated values. The peak heights were taken to be the vertical distance between the abscissa of the corrected spectra and the highest point of the C–O–C peak at about 1118 cm^{-1} (Fig.4.1.3). The error was estimated by repeated measurements of one sample at one given angle at different times and calculating the standard deviation of the measured values.

A second series of measurements was performed in situ, using the liquid cell, where the EG₆OMe SAM was in contact with a thin layer of water. Because the solubility of BaF₂ is about 1.6 g/kg in water at room temperature [94], a 0.1 M NaF/water solution was used instead in order to avoid damage to the BaF₂ half-cylinder as a consequence of prolonged exposure to water. The duration of one in situ measurement at a resolution of 8 cm^{-1} was about 20 min including the time required for the calibration of the instrument after the angle was changed. In addition, the thickness of the water layer was determined by an ellipsometry measurement of about 15 min duration before and after the PMIRRAS measurement. The results of the angle dependent measurements and the calculation are compared in Fig.4.1.5. The optical constants used for the four-layer model are listed in Tab. 4.1.1. Establishing the systematic error for the in situ measurements was more difficult than for the data taken in air. The data point at 80° was taken nine times under similar conditions and the standard deviation of these measurements was taken as error estimate for the data points at 45° , 55° , 67.5° and 82.5° degrees, which were measured

Table 4.1.1: Optical constants for the PMIRRAS calculation in Fig. 4.1.5

Layer	d (nm)	n
BaF ₂	n/a	1.4148
H ₂ O	1200	1.2588
SAM	2.8	1.4
Au	n/a	9.38

only once. Despite the large error bars, the experimental data reproduce well the trend of the calculation. In the simulation only one overall scaling factor was used between experimental and calculated data points; no other fitting parameters were used. The additional line in Fig. 4.1.5. shows the measured water layer thickness for each point. The reason for the larger discrepancy at 65° and 77.5° is the fact that the actual thickness of the water layer was much larger than the thickness used for the calculation of all angles. In addition, during the experiments it was noticed that, under certain conditions, for instance when the sample is not entirely parallel to the barium fluoride prism, thickness measured by the relatively small laser spot (ca. 1 mm × 2 mm), may vary from the actual range of thicknesses over which the much larger beam of infrared light is averaging (ca. 0.5 cm × 3 cm).

4.1.1.4 Conclusion

To conclude, this study demonstrates the importance of choosing and controlling the experimental parameters (incident angle, thickness of the water layer, sample size etc.), in particular for in situ PMIRRAS experiments. The presented software can serve as an aid for the selection of the optimum settings regarding angle of incidence and thickness of the liquid layer when a complex multilayer system is studied, especially if the optical constants of the employed materials strongly depend on wavelength. The accuracy of the calculated data was examined by a systematic experimental study and was found to be in excellent agreement with the experimental values.

4.1.2 Estimation of the water layer thickness for *in-situ* measurements

In Sec. 4.1.1 the PMIRRAS signal strength was simulated for various conditions and the findings were compared to experimental data, showing good agreement. It was calculated, that for measurements of thin layers on Au covered substrates under water, there is a high signal strength at 70°. Moreover, it has been shown that it is virtually constant a thickness of the water layer from 1 μm to 2.5 μm (Fig.4.1.2). Therefore, this angle is a perfect choice for measurement series focusing on relative changes in spectra. In section 4.1.1 the thickness of the water layer was measured by ellipsometry. The purpose of this

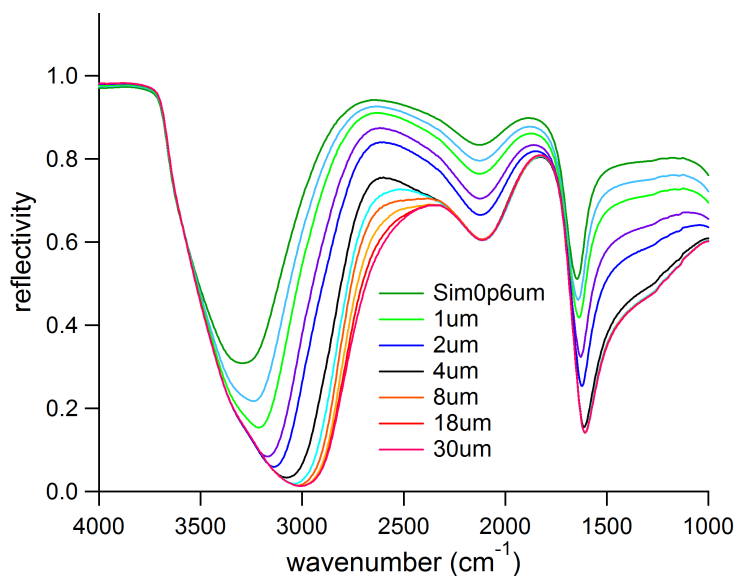


Figure 4.1.6: Calculation of the Average Reflectivity of p- and s-polarized light, this term is used in PMIRRAS measurements to normalize the difference signal, also compare to Eq. 3.2.12 and Eq. 3.3.21. Note, that the reflectivity curves are well distinguishable from each other for different thickness of the water layer, which makes them a good tool for its estimation.

section is to discuss alternative approaches for the estimation of the layer thickness and to compare the results to ellipsometric measurements.

Ellipsometry is well suited to measure the thickness of thin layers with known optical constants. However, for *in-situ* experiments there are some drawbacks. First, as already discussed in Sec. 4.1.1 the spot size and position are not exactly the same for ellipsometric and PMIRRAS measurements. This can generate errors if the sample is not exactly parallel to the crystal, compare Fig. 4.1.7 Second, and even more important, the sample cell has to be removed from and placed again in the PMIRRAS setup, with subsequent readjusting. This may be difficult e.g. for temperature measurements, where the temperature has to be kept constant. Third, ideally the thickness of the water layer and the PMIRRAS signal are measured simultaneously, especially in case of real time measurements an automation would be eligible. The first two points can be overcome by calculating the thickness of the water layer using the IRRAS signal, according to a method used in literature [70, 95]. However, a simultaneous measurement and an automation is not possible since the PEM unit has to be switched off in order to measure IRRAS spectra. In this section a method to calculate the thickness of the water layer directly from the PMIRRAS signal is described and the results are compared with ellipsometric measurements as well as the calculation method using IRRAS spectra. Figure 4.1.6 shows the calculation of $\frac{1}{2}(R_s + R_p)$, the average of the reflectivity of s- and p-polarized light, corresponding to the average PMIRRAS signal passing a low pass filter. There are significant differences between the curves for various water layer thickness, showing the sensitivity of the method

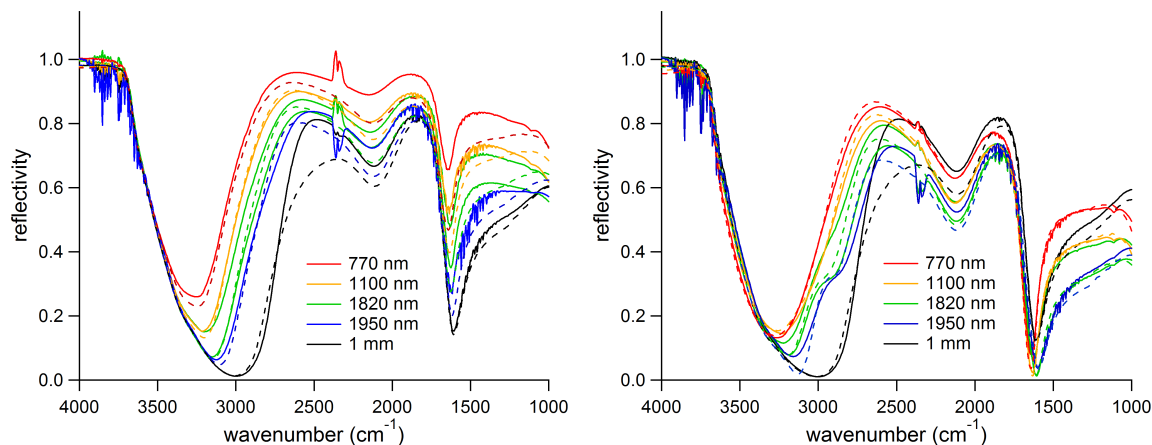


Figure 4.1.7: A comparison of experimental reflectivities and calculated reflectivities is shown. The thickness for the calculations is taken from ellipsometry measurements, enabling a comparison between different methods for the determination of the thickness of a thin water layer. Experimental data is shown in solid lines, calculations in broken line. On the right hand side the normalized IRRAS reflectivity curve is shown and the corresponding calculated values, showing good agreement. On the left hand side the PMIRRAS average signal $\frac{1}{2}(R_s + R_p)$ is shown and the corresponding calculated signal, there is a good agreement especially for wavenumbers higher than 2500 cm^{-1} . Note that for both solid green curves the same thickness was measured with ellipsometry, however, the thickness is not exactly the same as can be seen in the reflectivity spectra. The calculated curve is in the average of the experimental curves, possibly the sample is tilted and ellipsometry and infrared data are measured on different spots.

in this thickness range.

For a comparison, *in-situ* measurements with a thickness of the water layer over a range of $0.7 \mu\text{m}$ to $2 \mu\text{m}$ are shown. The samples were measured first with PMIRRAS, then with IRRAS and last with ellipsometry. The ellipsometric data was fitted in VASE using a model of the optical layer system, see Fig. 3.3.9 and compare to Sec 3.6. The reflectivity of s- and p-polarized light was calculated with a program using the algorithm described in Sec. 4.1.1 (also compare to [70,95]) In order to evaluate the three methods, the calculations were performed with the water layer thickness measured by ellipsometry for the real samples. The calculated reflectivities were compared with the corresponding normalized experimental reflectivities. This is in case of IRRAS R_p , in case of PMIRRAS $\frac{1}{2}(R_s + R_p)$. The measured reflectivity was normalized using a measurement of the empty *in-situ* cell.

A comparison of experimental and calculated reflectivity spectra, using the thickness measured with ellipsometry shows a good agreement (see Fig. 4.1.7). The reflectivity R_p of the IRRAS signal is in good agreement with the calculated values over the whole spectral range. A comparison of the experimental PMIRRAS average signal ($\frac{1}{2}(R_s + R_p)$) with the corresponding calculated signal shows good agreement in the range from 4000 cm^{-1} to 2500 cm^{-1} . In the range below 2500 cm^{-1} , however, are substantial differences between the experimental and calculated values. The discrepancy in the lower wavenumber region is

possibly due to the modulation of the signal with the PEM unit. However, a comparison in the range above 2500 cm^{-1} is sufficient for a determination of the thickness. This spectral region shows substantial differences in the spectra, even for differences in the range of 100 nm in the thickness of the water layer.

4.1.2.1 Conclusion

It is shown, that it is possible to determine the thickness of the water layer directly from the PMIRRAS measurement. There is a good agreement with results from ellipsometric and IRRAS measurements. Especially in the spectral range above 2500 cm^{-1} the calculated data points match the measured spectra. This enables the monitoring of the thickness of the water layer during *in-situ* series and a calculation for all PMIRRAS *in-situ* measurements done, ex-post. The method allows a normalisation and successively quantitative relation of *in-situ* data measured with different water layer thickness. A further step would be the programming of a tool for an automated fitting of the thickness, using the results presented in this section. This tool may be incorporated directly into the measuring software for real time thickness evaluation. With its help it could be estimated if the signal strength is remaining constant over the time range of the experiment.

4.1.3 Normalization of spectra

Transmission infrared spectra and IRRAS spectra are absolutely normalized. This makes it possible to perform quantitative comparison of different spectra, as long as the length of the optical way through the examined substance is known. In PMIRRAS spectra, the absorption spectra are folded with the second order term of the Bessel function (see Eq. 3.3.21), which makes a quantitative comparison difficult. It was shown by Buffeteau et al. [25] that it is possible to transform PMIRRAS spectra into IRRAS spectra, with the help of additional measurements using a polarizer behind the sample and normalization with the signal of the bare substrate (see. 3.3.6). In this section this should be checked experimentally. Especially the influence of different substrates and the corresponding different intensity of the Bessel arches should be elucidated. The concept of absolute normalization, which can be achieved with the polarizer calibration method is really fascinating, however, the effort is very high. One has to measure six instead of one spectra, the bare substrate with and without a s-and p-polarizer after the sample and the real sample with and without polarizer. One way to save measurements would be to perform only step one of the calibration procedure. In Fig. 4.1.9 a spectra of EG₆OMe on gold treated with step one can be seen in comparison with the IRRAS spectra. The result looks not very promising, similar to the results mentioned at Buffeteau et al. [25]. This suggests, that a reference sample needs to be measured - in most cases the bare substrate to perform a suitable calibration.

Four measurements with polarizers have to be performed in order to calculate a IRRAS

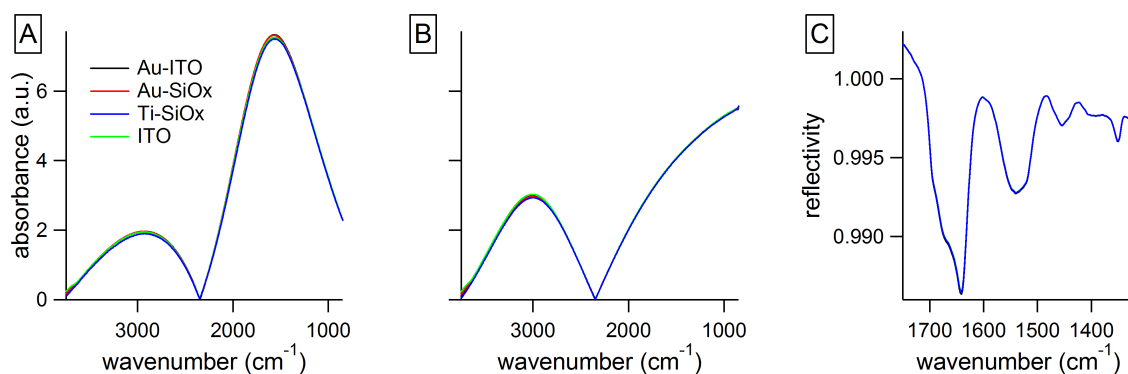


Figure 4.1.8: Calibration spectra on different substrates, obtained by introducing a additional polarizer after the sample are shown and the resulting normalized spectra using them for the normalization procedure. In A spectra for a s polarization after the sample are depicted, in B spectra for a p-polarization after the sample. In C spectra of a PEG-biotin SAM on Ti-SiOX normalized with the spectra in A and B are shown. Note, that the spectra are virtually identical, regardless of the sample used for the normalization reference measurement.

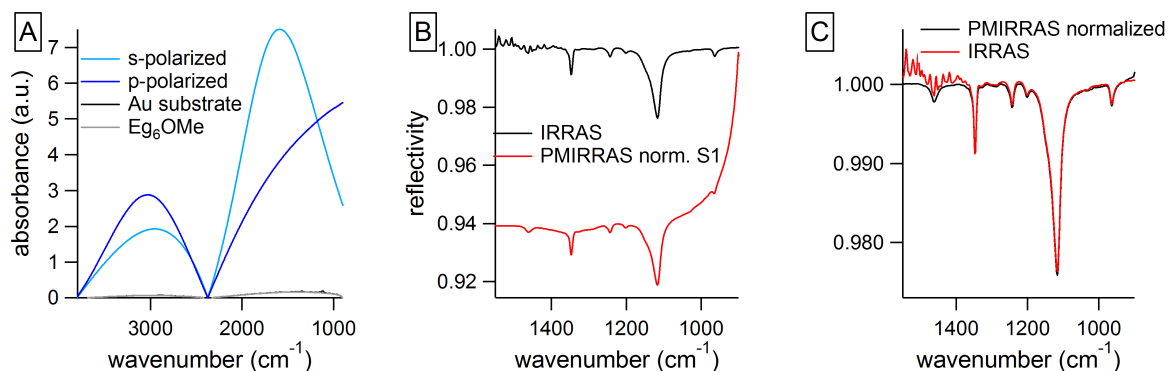


Figure 4.1.9: Calibration procedure shown by means of a EG_6OMe SAM on an Au substrate. In A raw PMIRRAS data are shown, note the increased signal of the calibration spectra with respect to the sample spectrum taken without a second polarizer. In B the corrected spectrum of an EG_6OMe SAM on Au is shown, calculated from the data shown in A. It is compared to the corresponding IRRAS spectra, the good agreement proves the usability of the calibration method.

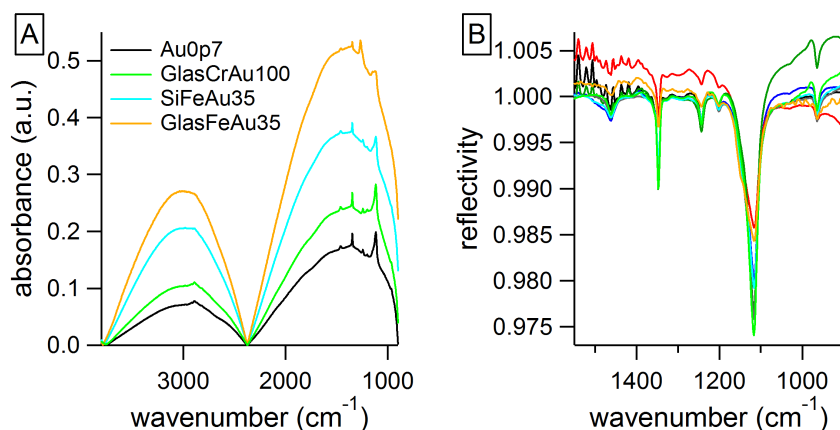


Figure 4.1.10: The figure shows the applicability of the calibration method for substrates, whose PMIRRAS signals show different intensities of the Bessel arches. In A the raw data are shown, in B the comparison of the processed data with IRRAS data are shown, showing a good agreement.

signal from the PMIRRAS data. In the following paragraph it should be elucidated if this is really necessary for each measurement. In Fig. 4.1.8 the calibration spectra using a s- and a p-polarizer after the sample (A and B respectively) are shown and the resulting normalized spectra (C). The calibration functions as well as the resulting spectra look nearly identical, suggesting, that it is not necessary to measure the calibration spectra for each sample, this saves four out of six measurements and make the calibration procedure much more time effective. However, there is one disadvantage of the method left: one has to measure an reference spectra of a clean bulk sample etc. in some cases this is not possible, for such cases PMIRRAS was originally made and in other cases one has to be careful to use a real blank sample to prevent the introduction of artifacts into the normalized spectra. Therefore, one has to decide how important the absolute values and their comparability with other absolute value are for the experiment and decide if a normalization procedure is necessary.

As a last point it was of interest if the normalization is also possible for high intensity Bessel arches, indicating a big difference in the reflectivity of s- and p-polarized light. To this end the calibrated PMIRRAS spectra of EG₆OMe SAMs grown on gold substrates with different thickness and different underlayer were compared with IRRAS spectra. The variation of the substrates was resulting in a different intensity of the Bessel arches and also an different SAM growth (see Fig. 4.1.10A for raw data). There is a high agreement of the PMIRRAS and the IRRAS spectra (compare to Fig. 4.1.10B), showing the high potential of the calibration procedure for a reliable quantitative comparison of PMIRRAS measurements on different substrates.

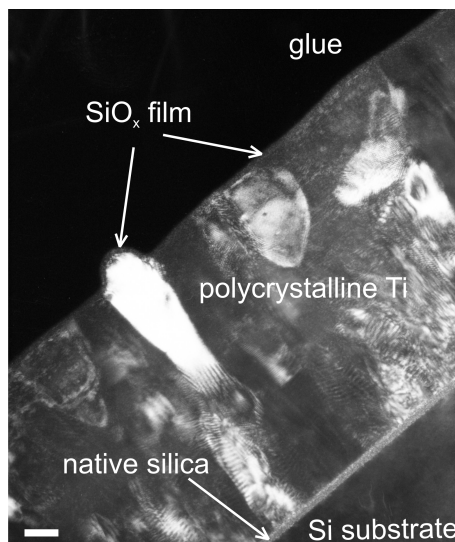


Figure 4.1.11: Dark field TEM image of cross-sectional Si-Ti-SiO_x specimen. Scale bar represents 20 nm.

4.1.3.1 Conclusion

It was shown, that it is possible to normalize infrared spectra measured in air with a normalization procedure developed by Buffeteau et al. [25] disregarding the exact reflecting properties of metallic surfaces. It was further confirmed, that a reference spectra of the blank substrate is needed. It is enough, however, to measure the reference spectra with a second polarizer after the sample only once. If the scope of an experiment lays on the quantitative comparison of molecules on different kinds substrates this method has proved to be a powerful tool.

4.1.4 Specific protein binding on PEG-Biotin functionalized surfaces

In this section a novel substrate enabling PMIRRAS measurements of molecules bound on a dielectric layer is described. The substrate consists of a titanium layer and a thin silica film on top. It is characterised with different methods and a proof of principle experiment is done studying the specific binding of streptavidin on a PEG-biotin functionalized surface. The results are already published in Ref. [16] and the section is adapted from the corresponding manuscript.

4.1.4.1 Characterization of Si-Ti-SiO_x substrates

The structure of the novel Si-Ti-SiO_x substrates is illustrated by a dark field (DF) transmission electron microscopy (TEM) image of the cross section in Fig.4.1.11. The titanium

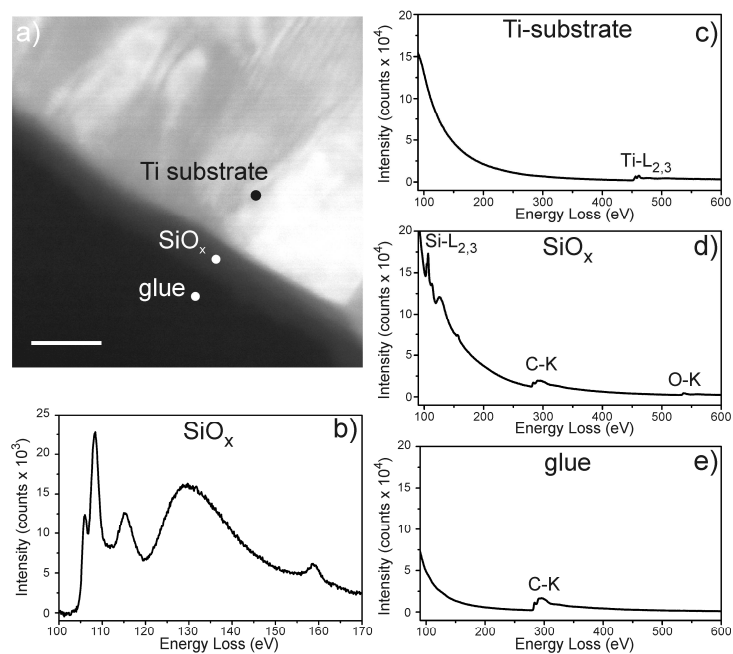


Figure 4.1.12: HAADF-STEM and EELS characterization of Si-Ti-SiO_x substrate. a) HAADF-STEM image of a cross-sectional TEM specimen. Scale bar represents 20 nm. c) d) e) EELS spectra recorded in the energy range of Si-L_{2,3}, C-K, Ti-L_{2,3} and O-K edges from the regions indicated in image (a). b) Background-subtracted Si-L_{2,3} edge acquired at a position similar to that of (d).

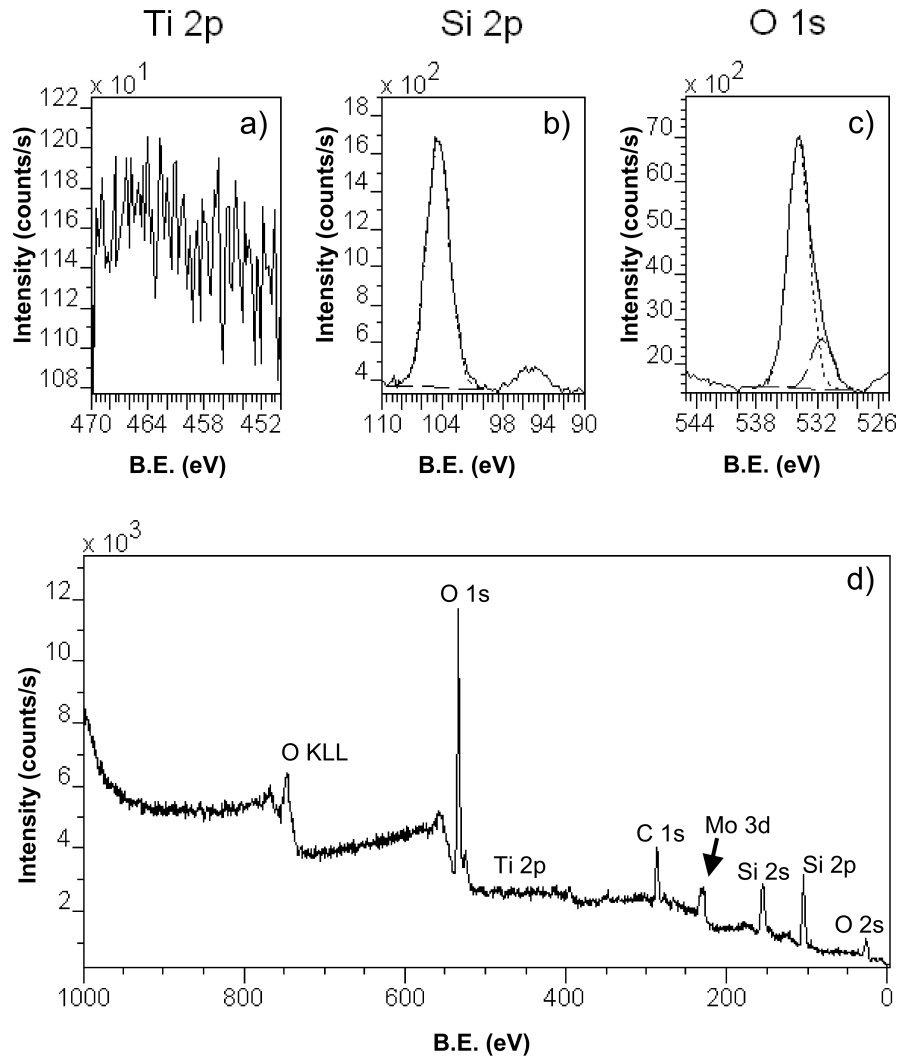


Figure 4.1.13: XPS spectrum of the Si–Ti–SiO_x substrate. Graphs show intensity in counts per second versus binding energy (B.E.) in eV. Detailed scans of the a) Ti 2p, b) Si 2p and c) O 1s regions: solid lines show measured spectra, near-horizontal dashed lines show fitted Shirley backgrounds and other dashed lines show fits to the measured spectra using Gaussian–Lorentzian functions as described in the text. The small peaks approximately 10 eV to the right of the main peaks in the Si 2p and O 1s regions can be ignored as they are almost certainly due to the presence of Mg K_{α3} radiation in the exciting X-rays. d) Overview of the entire spectrum. The C 1s peak may arise from contamination and/or adsorbed CO₂, as may the subsidiary O 1s peak at 531.6 eV. The Mo 3d peak is due to the sample holder.

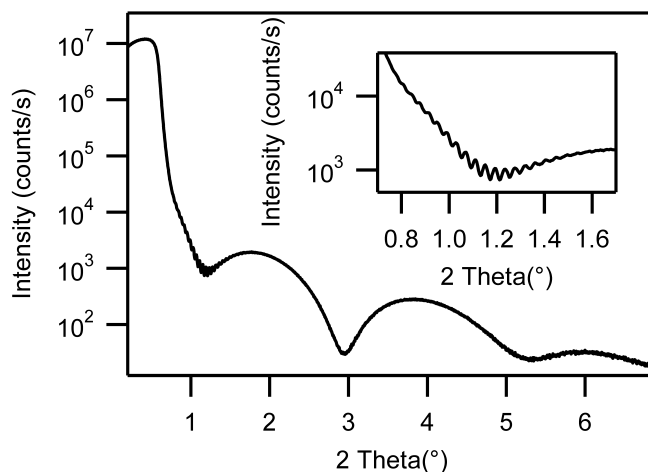


Figure 4.1.14: X-ray reflectivity of the Si–Ti–SiOx substrate, measured using Cu K α radiation. The interference fringes demonstrate the formation of well-defined interfaces and reveal the thicknesses of the SiOx and Ti layers. The narrow fringes (enlarged in the inset) correspond to a Ti thickness of 212 nm, whereas the broad fringes yield an SiOx thickness of 6.4 nm.

film lies on top of the silicon wafer and its native oxide layer. In this DF image, the polycrystalline nature of the titanium film is clearly visible. The silicon oxide film on top of the titanium film is visible, and appears to be of roughly uniform thickness (of the order of 5 nm) and to smoothly follow the titanium surface. Since the titanium film is polycrystalline, its surface is not entirely flat, but is rather punctuated by crystallites that rise out of the surface, as in the centre of Fig.4.1.11. (Images of other areas suggest that these features may be more common than shown in Fig.4.1.11.) A high-angle annular dark field (HAADF) scanning transmission electron microscopy (STEM) image of the surface is shown in Fig.4.1.12a. Electron energy-loss spectroscopy (EELS) measurements were performed in the various regions, i.e. the titanium substrate, the silicon oxide film and the glue used for the TEM sample preparation. The different spectra for the titanium substrate, the silicon oxide film and for the glue are shown in the energy region between 90 and 600 eV in Fig. 2c,d,e, and confirm the chemical identity of the deposited films. The Si-L_{2,3} electron energy-loss near-edge structure of the SiOx film corrected for the background is shown in Fig.4.1.12b. This spectrum contains two initial sharp peaks that are followed by a sharp and a broad peak and have been attributed to electron excitation into molecular orbitals associated with a silicon atom that is tetrahedrally coordinated [96,97]. Our intention was to investigate a silicon oxide, and not a titanium or titanium oxide surface; it is thus essential that the titanium layer should be completely or almost completely covered by the silicon oxide layer over the whole of the substrate. This is shown to be the case by the X-ray photoelectron spectrum (XPS) of the surface (Fig.4.1.13), which shows peaks in the Si 2p and 2s and O 1s and 2s regions, but no discernable peak in the Ti 2p region. The sampled area was of the order of square millimeters. The relative values

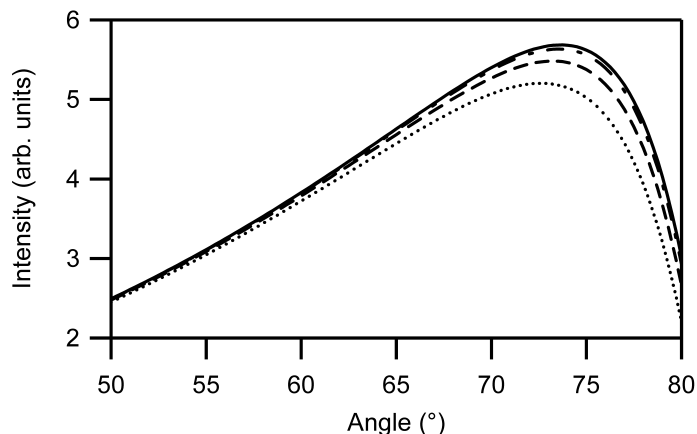


Figure 4.1.15: Simulation of the PM-IRRAS signal from an organic thin film (15 nm thick) which is separated from a semi-infinite titanium substrate by a silicon oxide film of thickness: no silicon oxide (—), 5 nm (---), 20 nm (····), 50 nm (-·-·).

of the areas under the Si 2p and O 1s peaks (Fig.4.1.13b, c), combined with tabulated sensitivity factors [98], give an atomic silicon to oxygen ratio of $1.5_{-0.0}^{+0.3}$. The fact that no titanium peak can be observed suggests that the silicon oxide film thickness is at least a few times the electron attenuation length in silicon oxide, which has been measured to be of the order of 2-3 nm [99], but may vary strongly with film density and microstructure; this is consistent with the film thickness observed by TEM. To measure the exact thickness of the Ti and SiOx films on the Si substrate X-ray reflectivity measurements were performed (see Fig.4.1.14). The data show distinct Kiessig oscillations which arise from the interference of X-rays reflected from the different interfaces and can be used to calculate the thickness d according to $d = 2 \pi / \Delta q$, where Δq is the periodicity of the oscillations in reciprocal space ($q = 4 \pi \lambda^{-1} \sin \vartheta$, where λ is the wavelength and ϑ the incidence angle). The narrow fringes shown in the inset to Fig.4.1.14 originate from the 212 nm thick Ti layer, whereas the broad fringes correspond to the 6.4 nm thick SiOx layer on top. Both thicknesses confirm the (local) values found by TEM measurements on a macroscopic length scale. Moreover, the data shown in Fig.4.1.14 indicate well-defined interfaces with moderate roughness for this particular sample. Because other samples showed increased roughness, the data was not analyzed in more detail.

4.1.4.2 Simulations of PM-IRRAS on Si-Ti-SiOx substrates

To enable optimization of the signal and to determine the influence of the thickness of the silicon oxide layer on the signal strength, simulations of the PM-IRRAS signal were performed as described in ‘Materials and Methods’. A model consisting of a semi-infinite titanium layer, a silicon oxide layer whose thickness was varied between 5 nm and 50 nm, and an organic layer with a thickness of 15 nm, which generated the specific infrared

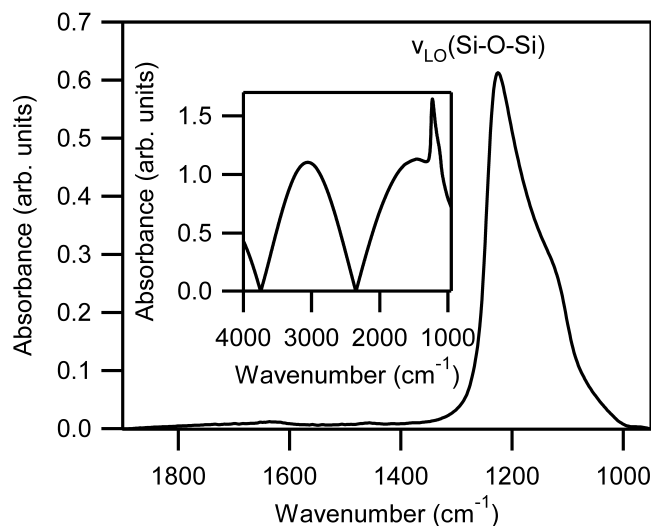


Figure 4.1.16: PM-IRRAS spectrum of non-functionalized Si-Ti-SiO_x substrate. Inset shows spectrum before, and main figure after removal of the Bessel function envelope.

absorption signal was used. For simplicity, smooth interfaces were assumed. As shown in Fig.4.1.15, the simulated signal from the organic layer is strongly angle-dependent, with an optimum (highest signal to noise ratio) angle of incidence around 74° from the surface normal. Importantly, the simulated signal is only slightly attenuated by the presence of the silicon oxide film, especially at the lowest film thicknesses. For a 5 nm thick silicon oxide film, which corresponds approximately to the Si-Ti-SiO₂ substrates used in this study, the signal is almost the same as that from an organic film on bare titanium, confirming that these substrates should indeed enable PM-IRRAS measurements of a similar quality to those performed on a metal surface.

4.1.4.3 PM-IRRAS measurements on Si-Ti-SiO_x substrates

A typical PM-IRRAS spectrum of a clean, non-functionalized Si-Ti-SiO_x substrate surface is shown in the inset to Fig.4.1.16. There are strong absorption bands from the silicon oxide film in the range 1000 to 1250 cm⁻¹; this region of the spectrum after removal of the Bessel function envelope is shown in the main part of Fig.4.1.16. Bands at 1225 cm⁻¹ and 1178 cm⁻¹ (broader band, visible as a shoulder) can be distinguished, and both may be attributed to longitudinal optical (LO) LO (Si-O-Si) stretching modes. The two bands are associated with differing Si-O bond angles and thus with the details of the local coordination of silicon atoms by oxygen atoms. The relative strength of these two bands is known to depend in general on the overall silicon to oxygen ratio - the band at 1178 cm⁻¹ has been associated with SiO, with the band at 1225 cm⁻¹ being associated with SiO₂ - as well as on the details of the local film structure [27]. As a proof of principle for the practical use of the Si-Ti-SiO_x substrate in PM-IRRAS,

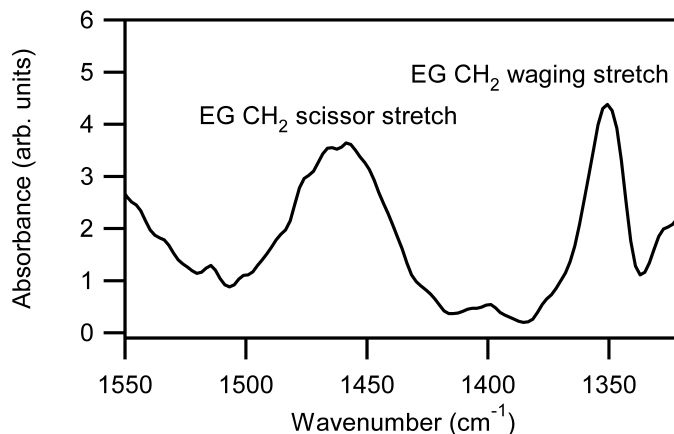


Figure 4.1.17: Background-subtracted PM-IRRAS spectrum of Si-Ti-SiOx that has been functionalized with silane-PEG-biotin.

now a series of measurements designed to investigate the protein adsorption properties of a selectively protein-resistant self-assembled monolayer of biotin-NH-CH₂-CH₂(O-CH₂-CH₂)_n-NHCONH(CH₂)₃-Si(OEt)₃ (silane-PEG-biotin), which was designed to enable the production of a surface that strongly binds streptavidin, although remaining resistant to other protein molecules is described. The resistance to protein adsorption of surfaces functionalized with *poly*(ethylene glycol) is well known, and silane-functionalized *poly*(ethylene glycol) molecules have previously been used to render silicon oxide surfaces protein resistant [100–103]; our silane-PEG-biotin molecule is similar to the silane-PEG-methoxy of Blümmel et al. [100]. The binding of biotin to the protein streptavidin is one of the strongest non-covalent interactions known, with an association equilibrium constant of order 10¹³ M⁻¹, and is also highly specific [104]. Since each streptavidin molecule has four biotin binding sites, streptavidin could be used as a linker for example to bind a chosen biotinylated protein molecule to the substrate surface. Silane-anchored, biotin-terminated PEG has been previously used to produce a surface that repels most proteins but can be functionalized with streptavidin [105–108]; to the best of our knowledge, the present study is the first time that this has been carried out using a one-step process involving the formation of a covalent bond to a silicon oxide substrate. A typical PM-IRRAS spectrum of an Si-Ti-SiOx substrate surface that has been functionalized with silane-PEG-biotin is shown in Fig.4.1.17. Because of the interference with the silicon oxide absorption bands, the strong C-O-C stretching mode could not be monitored. Nevertheless, other significant vibrational modes of PEG are visible: the ethylene glycol wagging mode (1350 cm⁻¹) and the ethylene glycol scissoring mode (1463 cm⁻¹) [109]. Fig.4.1.18 shows the PM-IRRAS spectra of blank and silane-PEG-biotin-functionalized Si-Ti-SiOx substrates that have been exposed to aqueous solutions of bovine serum albumin (BSA) and streptavidin respectively. It can be seen from the presence of strong amide I (1664 cm⁻¹) and amide II (1540 cm⁻¹) peaks that BSA has adsorbed in significant quantities

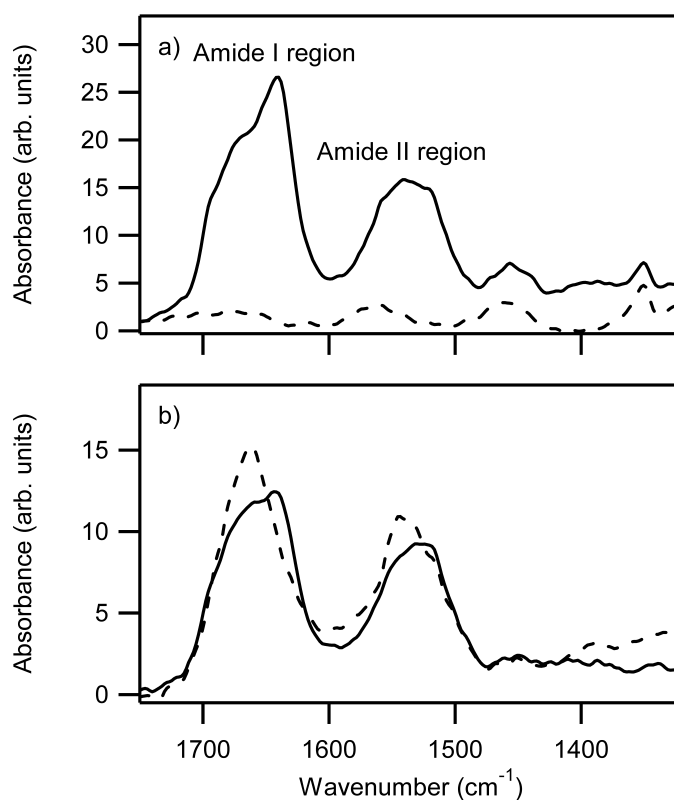


Figure 4.1.18: Selective adsorption of protein molecules by silane-PEG-biotin-functionalized silicon oxide surface. PM-IRRAS spectra measured on Si-Ti-SiO_x substrate surfaces that have been incubated in protein solutions, rinsed and dried. a) Silane-PEG-biotin functionalized surfaces following incubation in solutions of streptavidin (0.1 mg/ml in PBS, solid line) and BSA (1.0 mg/ml in PBS, dashed line). b) Control experiments on bare surfaces following incubation in solutions of streptavidin (0.1 mg/ml in PBS, surface heated with toluene and triethylamine as control for PEG-biotin reaction, solid line) and BSA (1.0 mg/ml in PBS, surface heated with toluene and triethylamine, dashed line). Incubation time 50 min (all spectra). Spectra of bare substrates have been subtracted.

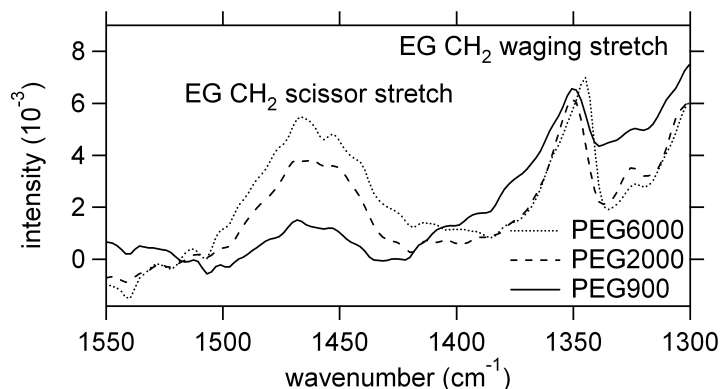


Figure 4.1.19: PMIRRAS absorption spectra of PEG coatings. EG CH₂ wagging and scissor mode region of PEG900, PEG2000 and PEG6000 coatings, measured with PM-IRRAS. The absorption bands indicate the presence of PEG.

to the blank substrate, as expected for a silicon oxide surface [110]. In contrast, there is no discernable BSA on the silane-PEG-biotin-coated surface. When similar surfaces are exposed to aqueous streptavidin solutions, however, significant amounts of streptavidin are seen to adsorb to the silane-PEG-biotin surface. These results thus demonstrate that the silane-PEG-biotin-functionalized surface has its intended properties of binding streptavidin, but resisting the adsorption of other proteins.

4.1.4.4 Surface loading as a function of PEG length

PMIRRAS measurements were made to prove the successful immobilisation of the different length PEG molecules on the sensor surface. The infrared spectra of the PEG layers in the region of the ethylene glycol CH₂ (EG CH₂) wagging and scissor modes [109], demonstrating the presence of the PEG coatings on the surfaces are shown in Fig. 4.1.19. Note that the C-O-C stretching mode of PEG is shadowed by a strong SiO₂ substrate mode [95]. After this, to demonstrate the specific binding of streptavidin, the PEG layers were functionalized with biotin and exposed to a streptavidin solution. The infrared spectra clearly show the specific binding of streptavidin to immobilized biotin, evidenced by the signal in the amide I and amide II region between 1500 cm⁻¹ and 1700 cm⁻¹ [111] and the presence of PEG on the surface shown by the absorption of the EG CH₂ wagging and scissor modes (Fig. 4.1.20). The intensity of the amide I and amide II bands are the lowest for PEG6000 coated sensor, showing less specific binding of streptavidin. In contrast, the bands of PEG 2000 coated surfaces show highest intensity and thus significantly increased specific binding. Exposure to BSA showed no signal in the amide region (data not shown). This indicates that the PEG-Biotin coating covers the whole surface, passivates it against non-specific protein adsorption, such as BSA and binds streptavidin specifically.

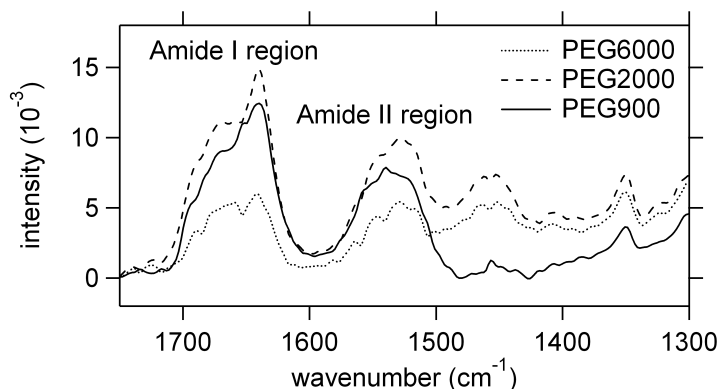


Figure 4.1.20: PMIRRAS absorption spectra in the region of the amide bands. PMIRRAS spectra of biotinylated PEG coatings after 1 h exposure to 100 $\mu\text{g}/\text{mL}$ streptavidin solution. The amide modes I and II can clearly be observed, indicating a binding of the protein. Additionally, the EG CH_2 wagging and scissor modes of the PEG coating can be detected.

4.1.4.5 Transmission measurements of PEG2000 SAMs on silicon substrates

In this section the PMIRRAS spectra shown in Fig. 4.1.17 and Fig. 4.1.18 are compared with transmission spectra of a PEG2000 SAM on silicon substrates shown in Fig. 4.1.21. The comparison reveals that the signal to noise ratio of the transmission measurements is much lower compared to the PMIRRAS measurements. With PMIRRAS measurements on Ti-SiO_x substrates the absorption modes of the EG CH_2 wagging vibration at 1348 cm^{-1} and the EG CH_2 scissoring vibration at 1463 cm^{-1} of a PEG2000 SAM could be measured with high signal to noise ratio and one is also able to see protein sub monolayers. With infrared transmission measurements, however, the absorption modes of PEG2000 molecules are even just above noise level. In addition, it is much harder to detect protein sub monolayers, due to the lower signal to noise ratio. The absorption modes of PEG2000 molecules are even just above noise level. Moreover PMIRRAS spectra can be collected within 5 minutes and have not to be normalized by a reference sample. An advantage of the transmission measurements is that they can be obtained with a simple setup and with standard silicon substrates.

4.1.4.6 Conclusion

It has been demonstrated that successively sputtered thin films of titanium and silicon oxide provide a valuable substrate for PMIRRAS measurements of self-assembled monolayers on silicon oxide surfaces, and such measurements were used to characterize the protein adsorption properties of a silane-anchored selectively protein-resistant self-assembled monolayer. The comparison with infrared transmission measurements, shows a significantly higher signal to noise ratio for PMIRRAS measurements. This stresses the high importance of PMIRRAS for the measurement of subtle changes in molecular monolayers

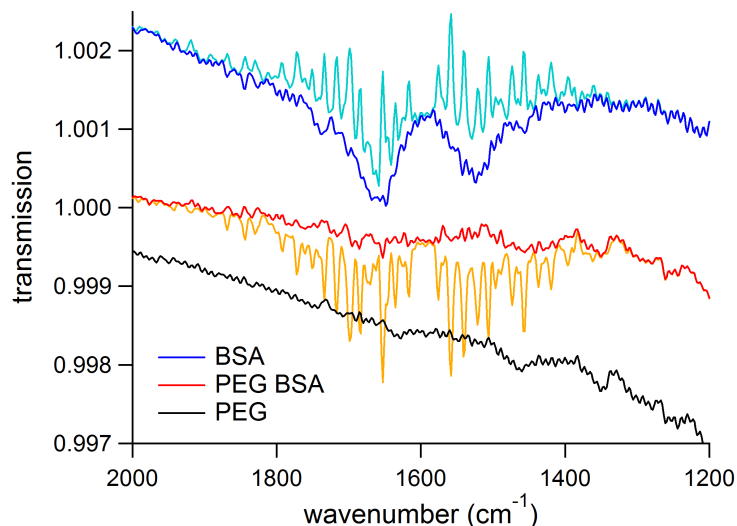


Figure 4.1.21: Spectra of a bare Si substrate and a functionalized one with a PEG2000 SAM are shown. The spectra in light colours are normalized transmission spectra before correction of water vapor absorption bands. After the correction procedure, it can be estimated whether protein is absorbed on the substrate or not, compare to Sec. 3.3.3. Note, that the spectra of the PEG coated substrate show absorption modes of the EG CH₂ wagging vibration at 1348 cm⁻¹ and the EG CH₂ scissoring vibration at 1463 cm⁻¹. The intensity of these modes, however, is only slightly above the level of background noise.

and the relevance of the substrates presented in this section.

4.2 *In-situ* growth of *oligo*(ethylene glycol)

The later stages of the growth of the hexa(ethylene glycol) terminated thiol (Eg₆OMe) were monitored in solution with PMIRRAS in real time. Modes in the fingerprint region were tracked and a conformational change from mixed all-trans and helical OEG moieties to predominant helical ones was observed. Further, the differences in conformation under aqueous conditions relative to in air conformation and the level of the change with respect to the surface coverage are shown. The results are published in Ref. [22] and the following section is adapted from the manuscript.

4.2.1 Identification and significance of the vibrational modes

Before analysing their temporal evolution, first the assignment and significance of the vibrational modes are explained. The focus will be on the spectral range from approximately 1050 cm⁻¹ to 1400 cm⁻¹ (Fig.4.2.1). This so-called ‘fingerprint region’ contains a number of absorption modes which are characteristic for the different conformations

Table 4.2.1: Spectral mode assignment of ordered OEG SAMs in the fingerprint region in helical and all-*trans* conformation respectively [46, 109]

mode assignment	Eg6OMe helical (cm^{-1})	Eg6OMe all- <i>trans</i> (cm^{-1})
EG CH ₂ rock (gauche)	964	
C-O, C-C stretch (gauche)	1116	
C-O, C-C stretch (trans)		1144
CH ₃ rock	1200	1200
EG CH ₂ twist	1244	
EG CH ₂ wag (trans)		1325
EG CH ₂ wag (gauche)	1348	
EG CH ₂ scissor (gauche)	1461	

of the molecules in the SAM. A detailed assignment of the modes can be found in the literature. [46, 109, 112] A position of the C-O-C stretching mode at 1116 cm^{-1} , an ether CH₂ twisting mode at 1244 cm^{-1} and an ether wagging mode at 1348 cm^{-1} are indicating a helical structure of the OEG moiety of the SAM. In contrast, a C-O-C stretching mode at 1144 cm^{-1} and an ether wagging mode at 1325 cm^{-1} , which may be split, indicate an all-*trans* conformation of the OEG-SAM. [46] A broadening, attenuation and a blue-shift of the absorption modes and the coexistence of modes characteristic for both conformations in fairly equal parts indicate a rather amorphous structure instead of a crystalline one. [46, 47] The CH₃ rocking mode at about 1200 cm^{-1} , a feature from the CH₃ end-group of the OEG-SAM, seems to be rather independent of conformational changes and can be used as an indicator for the surface coverage of the SAM. The reason of this insensitivity to structural changes is supposed to be due to its large interaction with water molecules and the resulting random orientation in aqueous solution. [28] See Tab. 4.2.1 for a summary of the vibrational modes.

4.2.2 Evolution of the modes

Since mounting of our thin liquid-layer-cell takes roughly 2 min and a scan with reasonable signal-to-noise ratio another 4 min, the first spectrum taken by us corresponds to an average growth time of 4 min, i.e. to an intermediate growth state. The data are very stable and reliably monitor subtle changes in the long time ordering process with a superior signal to noise ratio, but not the initial growth. With ordering and reordering respectively structural and conformational changes of EG₆OMe thiol molecules after binding to the surface are identified. The time evolution of the absorption spectra is shown in Fig.4.2.2. The position and width of the CH₃ rocking mode (1200 cm^{-1}) is not changing significantly and spreads around its mean value. This is underlining that there is no conformational change of the terminal CH₃ group over the measured time scale. Since there is no detectable intensity change of the CH₃ rocking mode, it is assumed that the increase of the surface coverage of the SAM is nearly finished until the start of the

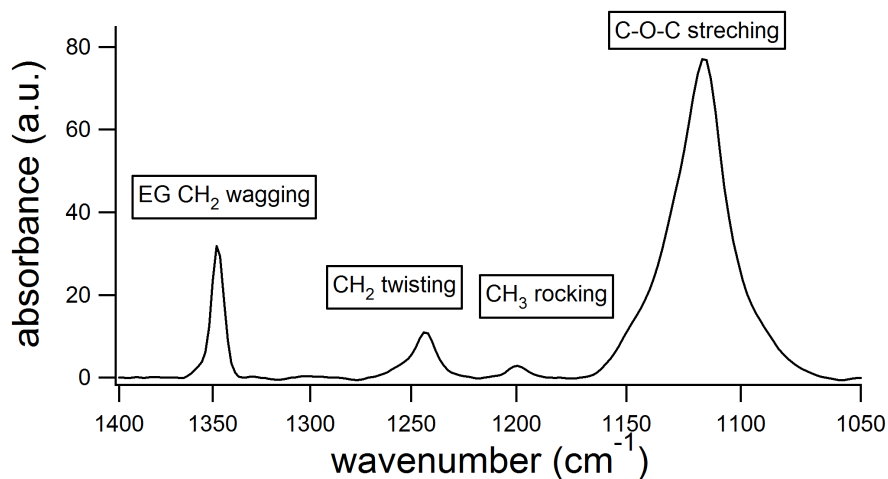


Figure 4.2.1: Spectrum of a fully grown EG₆OMe SAM under water, one can clearly see the different absorption modes. The dominating feature is the C-O-C stretching mode with its low frequency part at 1115 cm⁻¹ and its high frequency part at 1144 cm⁻¹. The CH₃ rocking peak at 1200 cm⁻¹, the CH₂ twisting Peak at 1244 cm⁻¹ and the EG CH₂ wagging mode at 1350 cm⁻¹ can clearly be distinguished. The dominating low frequency part of the C-O-C stretching mode, the EG CH₂ twisting mode and the strong EG CH₂ wagging mode are indicating a well ordered SAM with predominant helical conformation.

measurement. The intensities of the high frequency part of the C-O-C stretching mode at 1145 cm⁻¹ and the ether CH₂ wagging mode at 1325 cm⁻¹ are decreasing, whereas the intensities of the low frequency part of the C-O-C stretching mode at 1116 cm⁻¹, the ether CH₂ wagging mode at 1350 cm⁻¹ and the ether CH₂ twisting mode at 1244 cm⁻¹ are increasing over the measured period (Fig.4.2.3). The decrease of the modes associated with the all-*trans* conformation and the simultaneous increase of the modes assigned to the helical conformation is indicating an evolution from a mixed helical and all-*trans* conformation to a predominant helical conformation. In addition to the change in intensity, with progressing time also an increasing red shift, as well as a sharpening of the modes can be found. Typical data are shown in Fig.4.2.3. A comparison with spectra of liquid C₁₁EG₆OMe [46] and C₁₁EG₆OMe-SAMs grown over night in air reveals that the spectrum of the SAM in early states of our measurement shows more liquid-like features and evolves with time more and more to a spectrum similar to the one in air, suggesting an increasing order over time. Analysing the time dependence of this ordering process, it is found that the increase in intensity as well as the sharpening and the red-shift of the modes follow a single exponential behaviour (Fig.4.2.3). After about 100 min the sharpening of the peaks and the red-shift is finished, whereas the increase in intensity proceeds on a longer timescale. Besides structural changes there may be also another reason for the decrease of the high frequency part of the C-O-C mode. Malysheva et al. [113] calculated infrared spectra for OEG thiols in different orientations. They concluded, that even if the conformation is purely helical a high frequency shoulder can occur if the EG moiety is

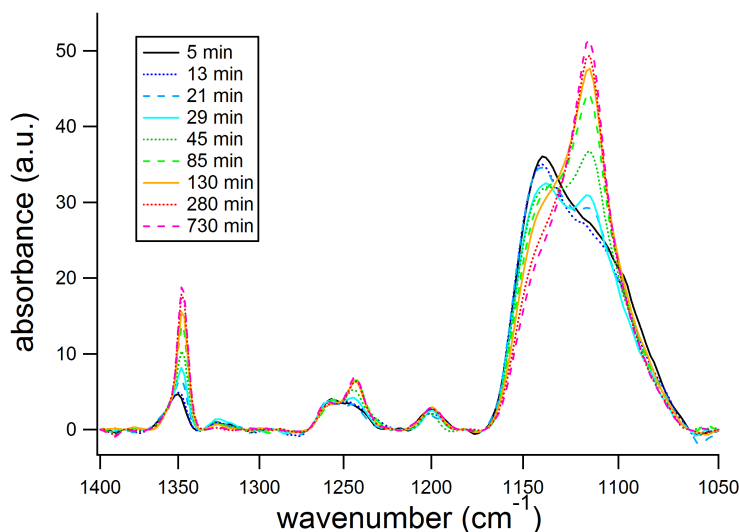


Figure 4.2.2: Spectra of EG₆OMe in aqueous environment as a function of growth time. The intensity of the low frequency part of the C-O-C stretching mode, the EG CH₂ twisting mode and the EG CH₂ wagging mode are increasing with time, while the intensity of the high frequency part of the C-O-C stretching mode is decreasing. The amplitude of the CH₃ rocking mode is constant.

not oriented perpendicular towards the surface. This is due to the surface selection rule for IRRAS measurements. The part of the electrical field oriented parallel to the surface is eliminated in the vicinity of the surface and so only dipole moments perpendicular to the surface can contribute to the signal. If the EG moiety is oriented perpendicular to the surface only dipole moments which are parallel to the helical axis contribute to the spectrum. However, if the helical axis is tilted, which is suggested in the model of the OEG-SAM in Malysheva et al. [114] and which may be also the case at low surface coverage enabling high conformational freedom, also modes perpendicular to the helical axis could contribute to the signal. The position of the strongest mode perpendicular to the helical axis is at 1142 cm^{-1} , [113] i.e. virtually at the same position as the mode assigned to the C-O-C mode in the all-*trans* conformation. Since no other modes which are perpendicular to the helical axis are seen and also a significant shift of the peak positions in the ‘fingerprint region’ as well as a sharpening can be seen, it is assumed that orientation effects contribute only marginally to the observed changes in our spectra. This is contrary to the liquid spectrum of OEG, which, of course, shows modes corresponding to all directions.

In order to understand the ordering process better experiments with less concentrated thiol solutions were performed. It was noticed that the process slowed down, due to its dependence on the thiol concentration, and stopped during the conformational change. Even after waiting over long periods of time (days) the spectrum did not change further. An exchange of the solution against fresh OEG-solution, however led to a further confor-

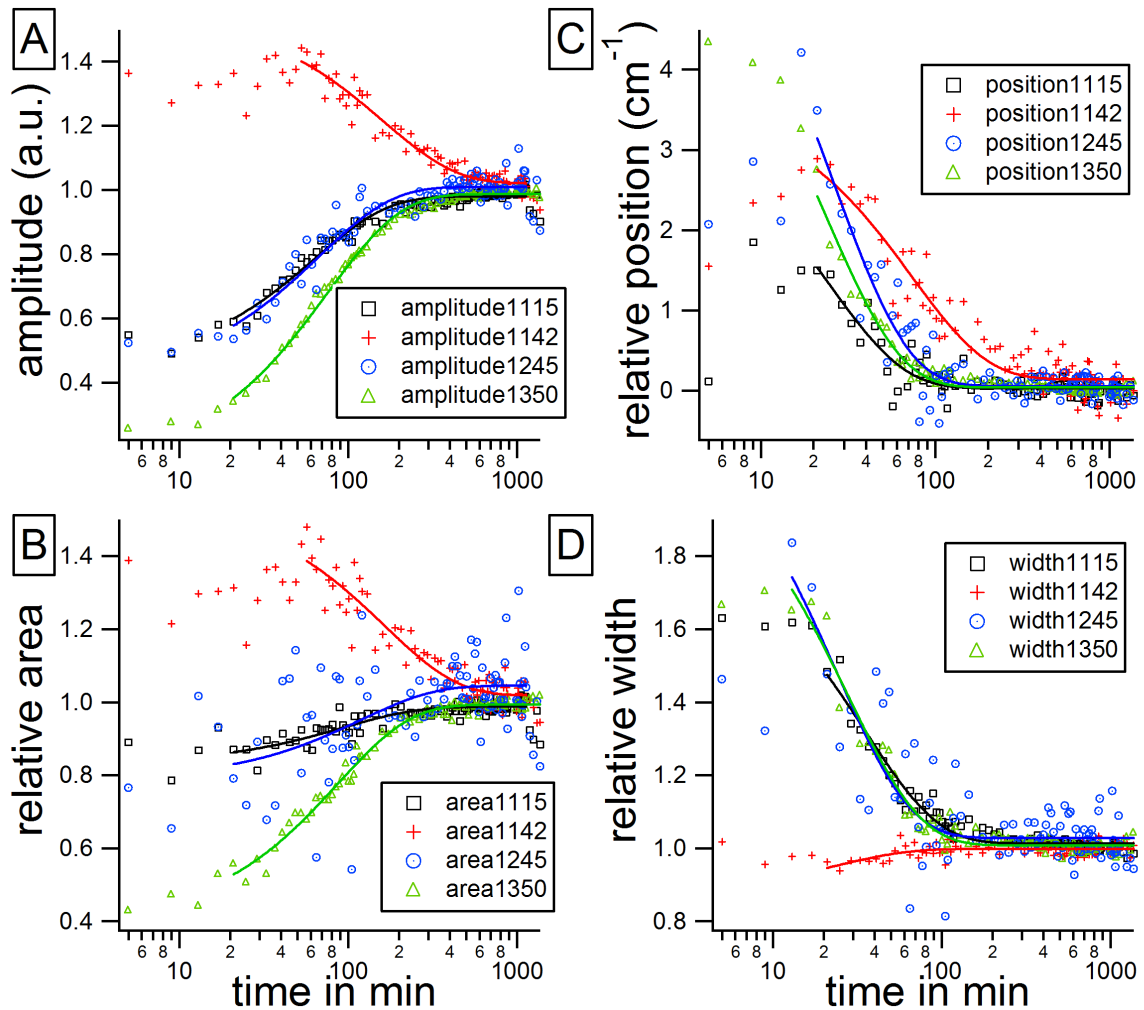


Figure 4.2.3: Kinetic fit of spectral characteristics as a function of time. For visualisation in one graph the values are normalized to the magnitudes at long time. In A and B one can see that amplitude and area of the Gaussian fits of the modes follow an exponential behaviour. While area and amplitude of the modes indicating a helical structure are increasing, the values of the high frequency mode of the C-O-C peak are decreasing indicating an increase in helical structure. In C one can see a red-shift of the peak-positions, towards the positions known for high ordered helical structures. The time scale of the shift of the high-frequency part of the C- O-C mode is significantly slower than the one of the shift of the other modes. In D one can see a sharpening of the peaks of the modes associated with a helical structure, indicating a increase in order over time. The peak of the high frequency mode of the C-O-C peak is not sharpening.

mational change with an increase of the helical fraction in the SAM. Also the experiment was stopped after a few hours, when the reordering was still in progress, by removing of the OEG-solution and monitored the SAM under pure water. This procedure slows down the ordering process dramatically. These experiments show that a steady incorporation of thiol molecules is a driving force for the reordering process. If this incorporation stops, the reordering is slowed down dramatically. This indicates that a dense packing helps to stabilize the energetically favourable helical conformation. An important point concerning the investigation of SAMs and their properties is their stability over long times. As known from literature, [115,116] OEG thiol SAMs exposed to air and light show substantial changes after a couple of days. To prevent this degeneration it is usual to prepare fresh SAMs directly in advance of experiments. In order to exclude degeneration effects for our experiments *in-situ* grown SAMs were monitored over long times *in-situ*. Even after six days no significant difference in the width, position and intensity of the absorption modes revealing the conformation and crystallinity of the SAM as written above could be found, for further details see Sec. 4.4.5. This indicates that the full-coverage SAM is very stable in solution against degeneration and desorption.

4.2.3 Interaction with water

In this study the OEG growth is monitored in real-time under aqueous conditions. Therefore, the interaction of the SAM with the solvent and the resulting differences of the measured spectra to those obtained in air or vacuum has to be taken into account. Skoda et al. [47] found a red shift of the C-O-C stretching mode for triethylene glycol-terminated alkanethiol monolayers under aqueous conditions. Also SFG data of the CH₃ region reveal large-scale distortions of the helical structure in liquid environments which leads to an amorphization of the SAM. [28,29] To clarify this point the reordering process was interrupted at different stages and spectra of the SAMs were measured in air. By this it was possible to compare the corresponding infrared spectra in water and in air. The spectra measured in air are quite different from the ones measured under aqueous conditions (Fig.4.2.4). At very early growth stages, which could be identified by a smaller area of the CH₃ rocking mode indicating a lower surface coverage, the SAM is rather disordered in water as well as in air. At higher coverage, during the reordering process a small area of the EG CH₂ wagging mode and the EG CH₂ twisting mode as well as a broad C-O-C stretching peak with equally high and low frequency components are indicating a poor order. In air the area of the first two modes is much higher and the C-O-C stretching peak is dominated by the low frequency component, indicating a highly ordered helical SAM. A fully grown SAM shows a highly ordered helical conformation whether recorded in air or in solution. Additionally, one can observe a red-shift of the C-O-C peak in water which becomes higher the lower the surface coverage is, compare to Skoda et al. [47] Now the question should be addressed how these phenomena can be interpreted. The poor order at low surface coverage can be attributed to the high conformational freedom at this stage and the resulting lack of an energetic gain by for a crystalline packing. With

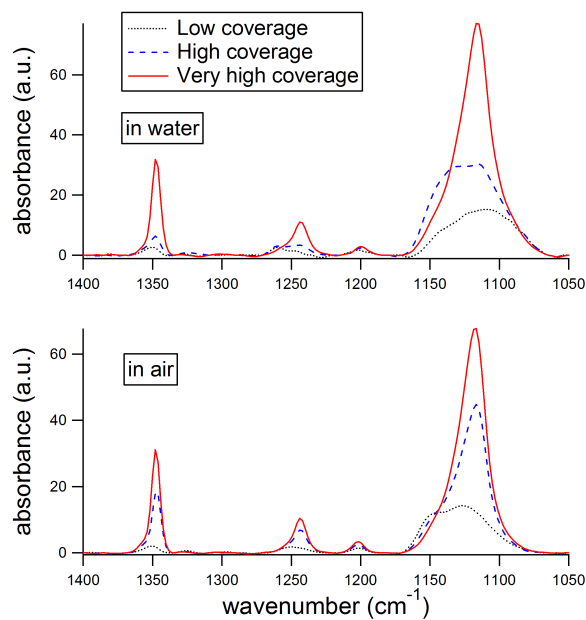


Figure 4.2.4: Spectra of EG₆OMe SAMs in water at different growth stages and the corresponding spectra in air. At early growth states the SAM shows a low order in air and under water. At intermediate growth stages the ratio of the high frequency part of the C-O-C stretch and the low frequency part is smaller in air, indicating a bigger proportion of molecules in the SAM in helical conformation and therefore a higher order in air. At the end of the growth process the spectra in air as well as in water show high helical order. Note that there is a red shift of the C-O-C peak under water, the earlier the growth state, the higher the shift.

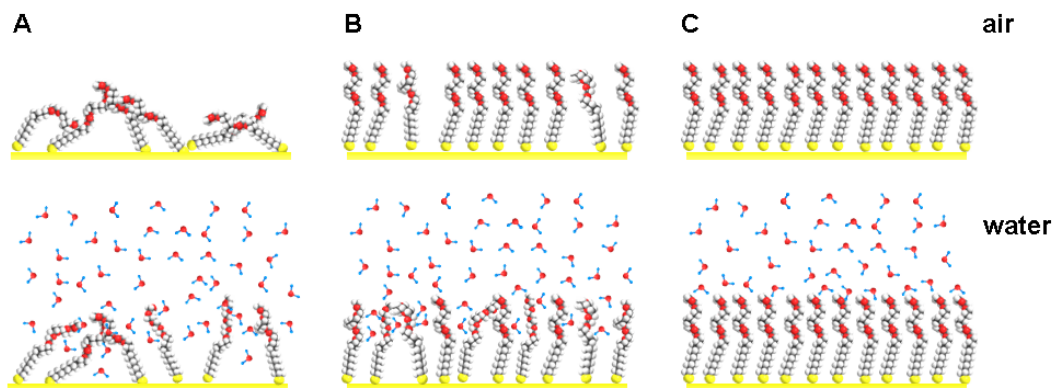


Figure 4.2.5: Schematic of the proposed interaction of water molecules with the EG₆OMe SAM at different surface coverage. At low surface coverage (A), the ethylene-glycol molecules on the surface are in air as well as under aqueous conditions rather unordered and in amorphous structure, water molecules can easily penetrate the SAM. At high surface coverage (B) the SAM shows a well ordered helical structure in air, however under aqueous conditions water molecules can penetrate deep into the OEG moiety and interact with it, resulting in structural disorder and gauche defects but also in a very stable and energetically favourable structure. For ideally helical SAMs with complete surface coverage (C) the water molecules cannot penetrate the ethylene-glycol moiety and the perfect helical conformation in air is preserved under aqueous conditions.

increasing packing density this freedom becomes smaller and a crystalline structure becomes energetically favourable. However, the molecules are not close enough to prevent water molecules from penetrating the SAM and so disturbing the conformation. [28,29] At complete surface coverage the water molecules are no longer able to penetrate the SAM deeply and disturb its structure and so there are only little differences in between the spectra in water and in air. This hypothesis is also supported by the coverage dependence of the red-shift. At low surface coverage there is a strong red-shift in water indicating a strong interaction of the SAM with the solvent, at high coverage and highly ordered SAMs this red-shift nearly vanishes. The larger width of the C-O-C peak at lower surface coverage in water indicates that the different modes contributing to the C-O-C peak are not affected equally by the interaction with water. [47] Vanderah et al. [31] reported in their studies of protein resistance of OEG-SAMs with different surface coverage that SAMs with complete coverage and perfectly helical structure are not resistant against unspecific protein adsorption while such with lower surface coverage (around 80%) and less well ordered structure are protein resistant. Our measurements suggest that this may be due to the different properties of the SAM to incorporate water molecules dependent of its packing density. Water plays a prominent role in the ability of a SAM to repel proteins [20] and the understanding of the parameters of its interaction with SAMs may lead to a deeper understanding of their protein resistant properties.

4.2.4 Conclusion

In this study it was shown that there is a change from a rather amorphous structure with all-*trans* and helical EG conformers to a crystalline structure with helical conformation in the last part of the growth process of a C₁₁EG₆OMe thiol SAM on gold. This reordering takes place on an exponential time scale. It can be identified by a red-shift as well as a sharpening and an increasing intensity of the vibrational modes associated with a helical conformation. Additionally, the intensity of those modes related to an all-*trans* conformation are decreasing. The lack of a significant change in intensity of the CH₃ rocking peak associated with the CH₃ group adjacent to the water layer above the SAM indicates that the change in surface coverage during the monitored period is small. Nevertheless, it was observed that the reordering process is dramatically slowed down if the incorporation of thiols stops. In addition, it was observed that the interaction with water strongly depends on the surface coverage (compare to Fig.4.2.5). As can be seen by comparing spectra in air and under aqueous conditions, even for high surface coverage there is a strong penetration of water and interaction with the EG moiety, while a SAM with a full coverage prevents this penetration. Due to these differences it is important to perform *in-situ* measurements in order to find out how the SAM behaves in its application under aqueous conditions. Since the ability of the SAM to ‘bind’ a water layer seems to be crucial for its ability to prevent unspecific protein adsorption, our results are also important to make this property more reproducible. It was shown that *in-situ* PMIRRAS measurements are a valuable tool to obtain information about the molecular structure under aqueous conditions. Due to a very thin liquid layer it is possible to get a high signal to noise ratio and so PMIRRAS may be used as a technique complementary to other *in-situ* methods for structural investigation like sum frequency generation.

4.3 Conformation as a function of surface coverage

In Sec. 4.2.3 the conformational change of OEG SAMs was investigated under aqueous conditions as a function of surface coverage of the SAM. The exact surface coverage was not defined, however, the virtually identical intensity of the CH₃ rocking mode for high and very high coverage SAMs suggests that in both cases the surface coverage is saturated. In this section two complementary methods are used to prove this assumption.

4.3.1 SPR measurements

First, OEG SAM growth was monitored with SPR. A low concentrated OEG solution (10 μ M EG₆OMe in H₂O) was used to follow the complete growth including the initial rapid growth on a time scale of minutes. A washing step with H₂O is followed by a flushing with EG₆OMe solution and by a second washing step. In Fig. 4.3.1 is shown, that the shift of the resonance peak, which is proportional to the thickness of the OEG layer on the surface

is following an exponential behaviour. Note, that additional to a fast exponential increase

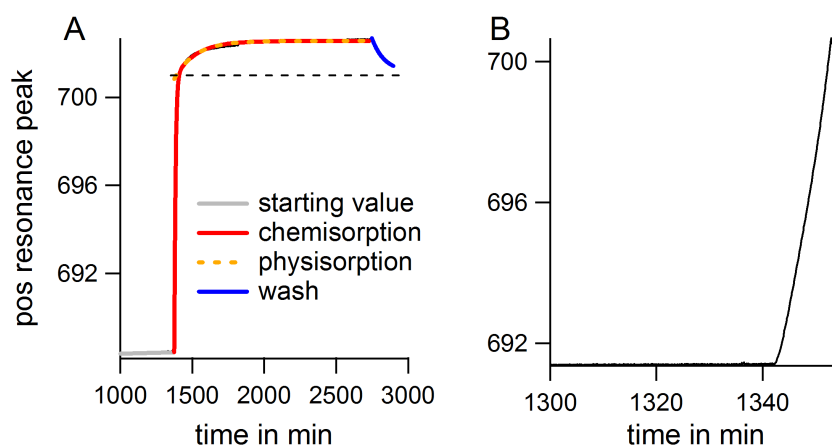


Figure 4.3.1: SPR measurement of the growth of EG₆OMe on gold. The figure shows the position of the resonance peak, linear proportional to the surface coverage, as a function of time. In A a washing step with H₂O is followed by a flushing with EG₆OMe solution and by a second washing step. Note, that the increase in surface coverage during incubation in EG₆OMe solution can be fitted with a fast and a slow component. Its decrease in the final washing step can be fitted with one exponential component, whose time constant is equal to the slow component of the incubation step. This is indicating that the fast component is featuring chemisorption and the slow components physisorption and desorption of OEG molecules. In B a washing step is followed by a flushing with EG₆OMe solution and a abortion of the measurement at incomplete surface coverage.

in the thickness of the OEG layer, which is identified as the increase in surface coverage due to chemisorption of thiol molecules on the surface, there is another slower exponential component of the slope. A successively washing step of the surface with H₂O led to an decrease of the position of the resonance peak. The time constants of the slow component of the increase of the resonance peak and of the decrease during the washing step are very similar and significantly smaller as the time constant of the fast exponential component. Moreover, their contribution to the absolute value to the shift of the resonance peak is virtually the same. This suggests, that a increase of OEG molecule concentration in the vicinity of the surface during growth e.g. physisorption may be responsible for the slow components (also compare to Ref. [117]). In order to measure the surface coverage due to chemisorbed OEG molecules, only the fast component of the shift of the resonance peak is taken into account. The single exponential behaviour of this component is indicating Langmuir growth. This and also the time constant of $\tau = 8.1 \text{ min}^{-1}$ for growth in a $10 \mu\text{M}$ solution are consistent with the literature [31] ($\tau = 10 \text{ min}^{-1}$ for growth in a $5 \mu\text{M}$ solution). Additionally, in further measurements the growth was aborted at 75% of the estimated resonance shift for a full coverage. The spectra were compared with each other and spectra from the mixed SAM series in Sec. 4.3.2.

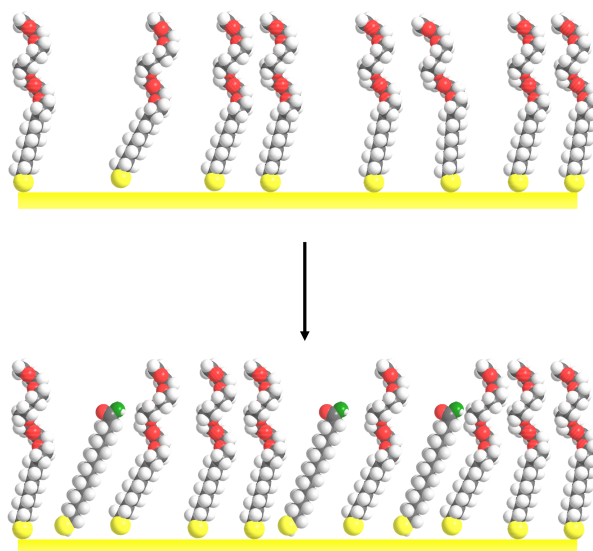


Figure 4.3.2: The scheme shows in the top part a EG₆OMe SAM with incomplete surface coverage. In the lower part is shown, that after immersion of the substrate in amid thiol solution free binding places are occupied by amid thiol molecules.

4.3.2 Mixed SAMs

In a second approach the formation of mixed SAMs was used to estimate the surface coverage. EG₆OMe SAMs were grown in a 10 μM solution of EG₆OMe thiols in H₂O for different times and their spectra in air and under aqueous conditions were recorded. Successively, the substrates were incubated in a 500 μM solution of 11-mercaptoundecanamide (amide thiol), a thiol containing a alkane chain with 11 carbon atoms and a amide group in H₂O. During this incubation amide thiol molecules were able to adopt free places on the substrate, see Fig. 4.3.2. The intensities of its characteristic modes, normalized against the intensities on a substrate completely covered with amide thiol can be used to estimate the fraction of unoccupied thiol binding places on the surface. There is, however, also a slow substitution of OEG thiols bound on the surface against thiols in solution, compare to [1, 118]. This exchange process takes place on a timescale of hours and days rather than minutes, however, it is useful to minimize its effect by choosing the incubation time of amid thiols as short as possible. It was figured out, that the spectra of an amide thiol SAM grown on a fresh substrate in a 500 μM solution of amide thiol does not differ for SAMs grown for 2.5 h and 24 h, indicating a full coverage within 2.5 h. In Fig. 4.3.3 the spectrum of an Eg₆OMe SAM grown over night is compared with the spectra of the same SAM incubated in amide thiol for 2.5 h and 120 h, respectively. After 2.5 h there is only a small change in the intensity of the modes indicating helical structure and no detectable absorption modes indicating the presents of amide thiol. This suggests, that the coverage

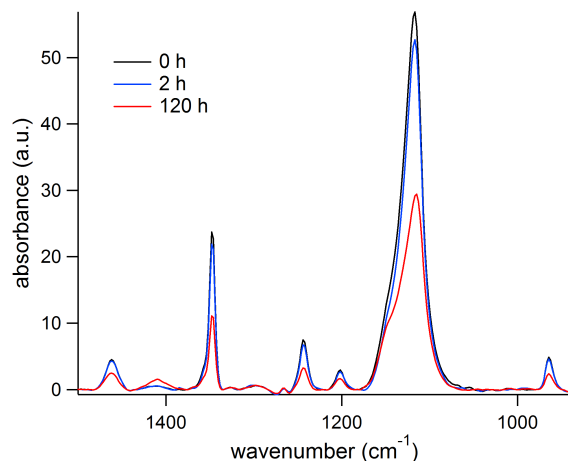


Figure 4.3.3: The spectra of an EG₆OMe SAM after growth and after successively immersion in amide thiol solution for 2 and 120 h, respectively is shown. After 2 h in amide thiol solution the spectra of the SAM show only small changes in the modes indicating helical structure and no significant changes in the CH₃ rocking mode and no detectable modes indicating the presents of amide thiols on the surface. This is suggesting a full coverage and no significant exchange of thiol molecules at the surface. After 120 h, however, the spectrum shows substantial changes as well as the presents of strong amide modes, suggesting a significant substitution of OEG-thiol molecules on the surface by amide thiol molecules.

of the SAM was nearly complete and more importantly, that the exchange of OEG thiols on the surface with amide thiols in solution was very small. After 120 h, however, there was a significantly decrease in intensity of the modes indicating helical structure as well as the CH₃ rocking peak indicating a significant exchange of molecules from the surface with molecules from solution, consistent with literature [118]. Therefore, for the following experiments 2.5 h were chosen as incubation time in amide thiol solution.

A series of EG₆OMe SAMs was grown in 10 μ M OEG thiol solution for different times and successively measured in air, under aqueous conditions and again in air after incubation in a 500 μ M amide thiol solution for 2.5 h. The spectra measured in air clearly show a rising intensity of the CH₃ rocking peak for increasing immersion time, indicating an increase in surface coverage. Additionally the intensity of the modes indicating helical conformation are increasing, similar to our growth experiments in solution. For a comparison with the spectra in aqueous environment (Sec. 4.2) see the corresponding spectra under aqueous conditions in Fig. 4.3.5. Also the spectra in air of the SAMs grown in the SPR measurements are also shown in Fig. 4.3.4. Note, that the intensity of the CH₃ rocking mode of the SAM grown for 12 min in the SPR setup is significantly smaller than the intensity of the corresponding mode of the SAM grown for 8100 min in bulk solution indicating an incomplete surface coverage. The intensity of the CH₃ rocking mode of the SAM grown in the SPR setup for 1350 min, however, is virtually identical to this reference indicating full coverage. This results connect SPR and infrared measurements

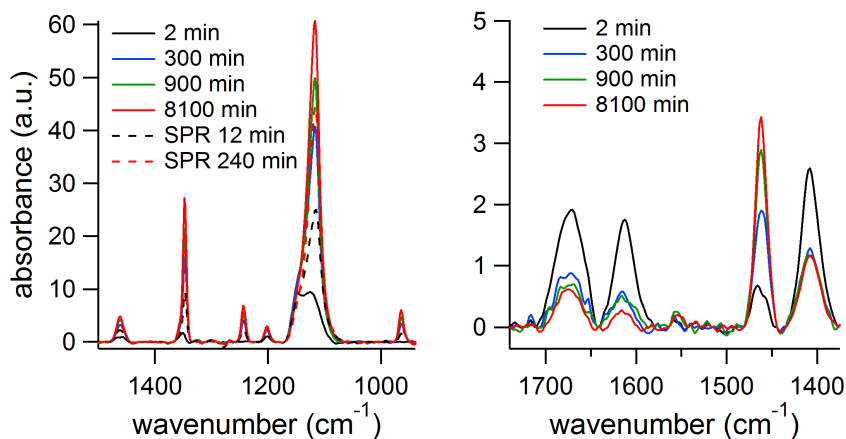


Figure 4.3.4: The spectra of a series of EG₆OMe SAMs with different growth times in EG₆OMe thiol solution, measured in air are shown. In A spectra measured directly after growth are presented. It can be seen that the part in helical order and the crystallinity is increasing with growth time. SAMs grown in the same solution during SPR measurements reach comparable growth states, related to their growth time. In B spectra of the same SAMs after immersion in amide thiol solution for 2.5 h are shown. The intensity of the amide absorption modes is the higher the lower the previous immersion time in EG₆OMe solution, indicating an increase in surface coverage of EG₆OMe over time.

and supports the infrared results. In Fig. 4.3.4 also the the spectral region of the amide absorption bands is shown. The used compound 11-mercaptoundecanamide is a primary amide, the mode at 1410 cm^{-1} can be assigned to the C-O-stretching vibration (Amide I), the mode at 1614 cm^{-1} an overlap of the C-N stretching vibration and the N-H bending vibration (Amid II) and the mode at 1674 cm^{-1} can be assigned to the a skeleton deformation vibration (Amide VI). The intensity of these modes is the higher the lower the incubation time of the SAM prior to the incubation in amide thiol solution. Considering, that the more amid molecules are bound to the surface due to free binding positions, the lower the initial surface coverage, this is consistent with the evolution of intensity of the CH₃ rocking mode in the spectra measured directly after OEG SAM growth. To get an quantitative understanding of this correlation a multi Gauss fitting procedure was performed and area and amplitude were plotted as a function of incubation time of the substrate in OEG thiol solution, see Fig. 4.3.6. The values of the CH₃ rocking mode are normalized to the value at immersion for 8100 min and the values of the amid modes to the value of the pure amid SAM. Note, that for better comparison between the modes, the difference of the amid modes of the miscellaneous spectra to the mode intensity of the pure amid SAM are plotted, illustrating the number of occupied binding sites. The relative values of the data points indicating surface coverage are increasing with immersion time of the SAM and saturating above a immersion time of 300 minutes. The behaviour of the data points related to the CH₃ rocking mode and the amid modes are following the same behaviour, which is supporting the idea that the intensity of the CH₃ rocking mode

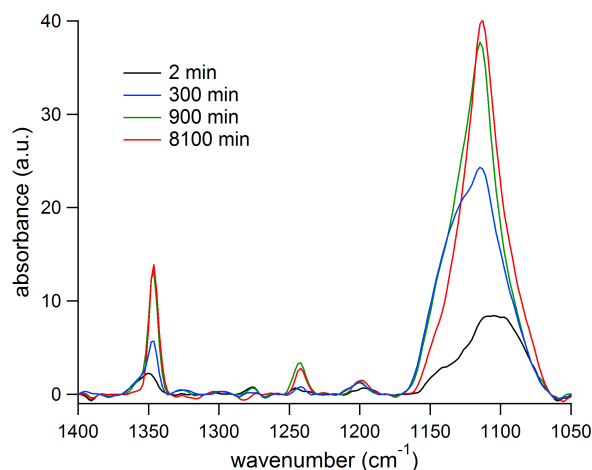


Figure 4.3.5: Spectra of a series of EG₆OMe SAMs with different growth times, measured under aqueous conditions are shown. It can be seen that the fraction of the SAMs molecules in helical order and their crystallinity is increasing over growth time. The same SAMs are measured as shown in Fig. 4.3.4 and Fig. 4.3.6, so this spectra can be compared with the results in Sec. 4.2.3.

is a good indicator for surface coverage. A comparison with Fig. 4.3.4 and Fig. 4.3.5 show that despite the saturation of the intensity of the CH₃ rocking mode and the amid modes for high immersion times, the modes indicating helical conformation are increasing significantly. This supports our assumption in Sec. 4.2 that during the monitored conformational change from mixed all-*trans* to helical conformation the surface coverage of the SAM is not changing significantly.

4.3.3 Conclusion

The focus of this section was on the evaluation of our assumption in Sec. 4.2, that the monitored reordering process takes place at saturated surface coverage. To this end, two approaches were followed. First, EG₆OMe SAMs were grown in a SPR setup until saturation of the resonance peak position, this is indicating a full surface coverage. Also short time measurements without saturation of the position of the resonance peak were performed. The infrared spectra of the resulting SAMs were compared to infrared spectra for SAMs grown in bulk solution. It was observed, that for spectra of the SPR measurements until saturation of the resonance peak position the intensity of the CH₃ rocking mode was virtually identical to the intensity of the modes for SAMs grown for very long time in bulk solution. However, for short time growth the CH₃ rocking mode was significantly smaller. This underlines the correlation of the intensity of the CH₃ rocking mode and the surface coverage.

In addition, after a growth in bulk solution for different times, OEG SAMs were immersed in an amid thiol solution and the intensity of the amid modes, indicating the number of

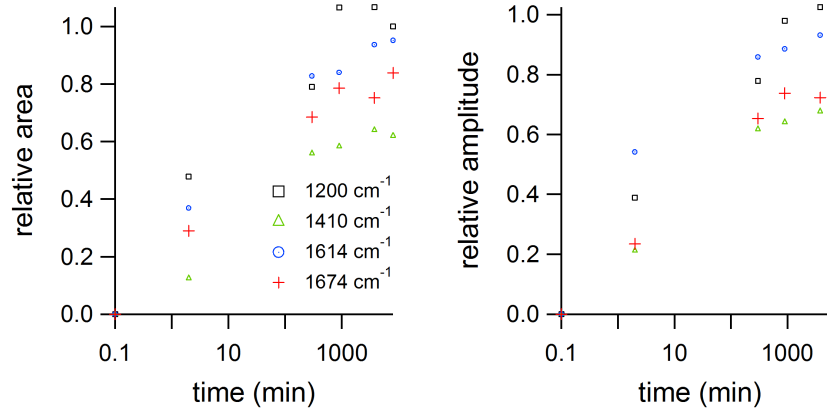


Figure 4.3.6: Plot of the areas and relative intensities of modes indicating the presence of amide thiols and the CH_3 rocking mode are shown. The data points are normalised to the value of the pure amide thiol SAM and the CH_3 rocking mode at full coverage (8100 min), respectively. Note, that the difference of the intensities of the amide bands and the value of the pure amide thiol SAM is plotted, indicating the number of occupied binding positions. This enables a better comparability of their intensity with the CH_3 rocking mode. A comparison of the results regarding the amid bands and the CH_3 rocking mode reveal similar results, they show a saturation of the surface coverage at growth times higher than 300 min.

free binding positions was measured. With increasing growth time in the OEG solution the intensity of amid modes was decreasing indicating a higher surface coverage of the OEG SAM. The behaviour was exactly reverse to the evolution of the intensity of the CH_3 rocking mode. For growth times above 300 min there was a saturation. These results supports our assumption in Sec. 4.2 that the reordering occurs at saturated surface coverage. To gain direct relations of surface coverage and structure, which was beyond the scope of this thesis, it is necessary to monitor the structure and the surface coverage under identical conditions *in-situ* and also consider time effects. Very suitable for such an attempt would be a setup enabling simultaneously PMIRRAS and SPR measurement.

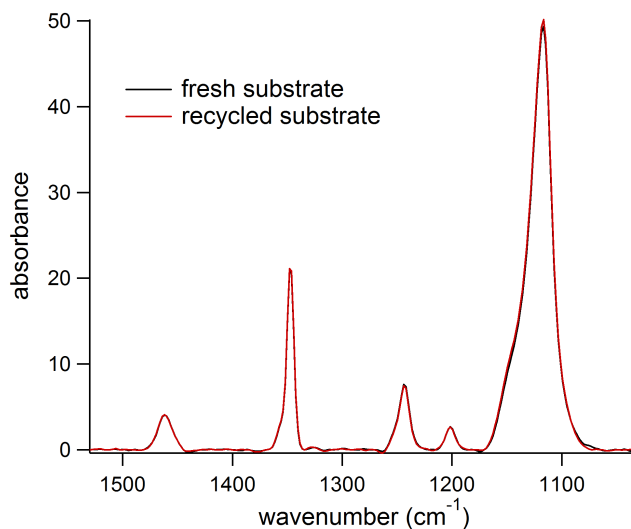


Figure 4.4.1: Spectra of EG₆OMe SAMs grown on fresh and recycled substrates, immediately after cleaning in UV light and successively rinsing with EtOH. The spectra are virtually identical, indicating no effect of a previously grown SAM on the growth of EG₆OMe SAMs on fresh UV cleaned substrates.

4.4 Stability of OEG-SAMs

The structure and properties of SAMs, especially SAMs containing an ethylene glycol moiety, are very sensitive towards subtle changes. Therefore, it is important to ensure reproducible conditions regarding substrate cleanliness prior to SAM growth and sample storage. It is especially interesting what happens with SAMs over time for different storage conditions. These results are also very helpful in order to interpret experiments using ethylene glycol SAMs to prevent biofouling. This section focuses on degradation effects and longtime behaviour of OEG SAMs under different conditions regarding light exposure, media and elevated temperature.

4.4.1 Degradation with UV-light

A common method [32, 119] to clean gold substrates is their irradiation with high energy UV light, containing energy bands around 185 nm and 254 nm, followed by a thorough rinsing with EtOH. The part of the UV radiation above a wavelength of 200 nm is able to excite and dissociate organic molecules, while the part with a wavelength below 200 nm is able to produce ozone from atmospheric oxygen. The ozone can oxidise sulfur and gold atoms and thus break the thiol bonds to the gold substrate [44, 120]. In combination with the UV radiation breaking bonds in the organic molecules, ozone is also able to fully oxidise the SAM into volatile products as carbon dioxide and water [32]. Importantly, oxidized gold atoms can be buried by self assembling alkane thiol molecules and so the origin

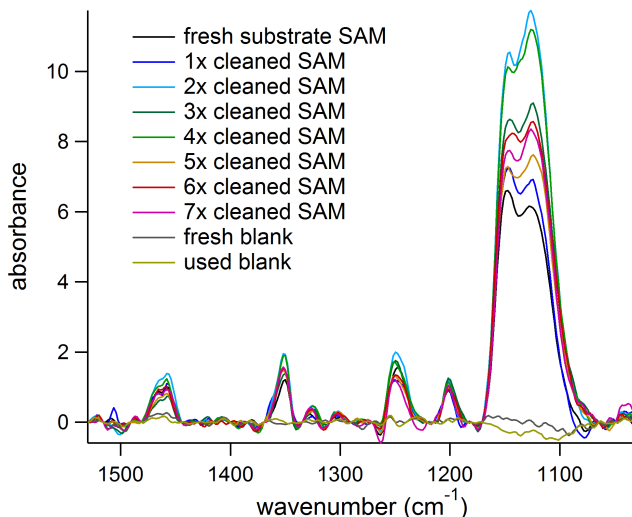


Figure 4.4.2: Spectra of EG₆OMe SAMs grown for 1 min on fresh and repeatedly recycled substrates, immediately after cleaning in UV light and successively rinsing with EtOH. There is no systematic trend in the intensity of the absorption modes regarding the number of recycling cycles, indicating no effect of a previously grown SAM on the growth of EG₆OMe SAMs on fresh UV cleaned substrates. Note, that this test is very sensitive towards the cleanliness of the substrate, as indicated by the variations between the different spectra. Prior to SAM growth no absorption bands can be found on the cleaned substrates, neither after initial cleaning, nor after cleaning after SAM growth, indicating a clean substrate.

of defects, lowering the quality of the monolayer. However, those oxidized gold atoms are very unstable and can be reduced by EtOH which is oxidized to volatile acetaldehyde [32]. A thorough rinsing of the substrates with EtOH after UV treatment significantly improves the SAM quality and makes the SAMs surface pattern indistinguishable from SAMs on freshly evaporated substrates, validated by STM and contact angle measurements. Additionally, it has been shown that the quality of SAMs grown on substrates evaporated 4 months prior to the experiments and 1 day prior to the experiment is the same as long as the SAMs are treated by the procedure above [32].

To verify this procedure for gold substrates used in this thesis, two kinds of experiments were done. First, PM-IRRAS spectra of gold substrates functionalized with an *oligo*(ethylene glycol) SAM were measured after UV treatment and compared to spectra of SAMs on fresh UV-cleaned substrates. Note, that prior to SAM growth no absorption bands can be found on the cleaned substrates, neither after initial cleaning, nor after cleaning after SAM growth, indicating a clean substrate, compare to Fig.4.4.2. As shown in Fig.4.4.1 the spectra cannot be distinguished from each other, indicating a complete removal of the SAM. To refine the test, *oligo*(ethylene glycol) SAMs were grown on both sets of wafers. The kinetics of SAM growth is assumed to be highly dependent on substrate cleanliness. Especially at intermediate growth steps, the structural differences between SAMs in distinct growth stages should be pronounced. SAMs were grown in a 100 μ M

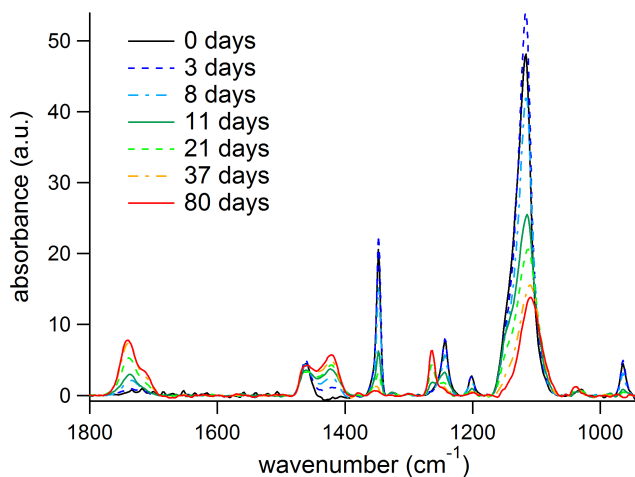


Figure 4.4.3: Spectra of an EG₆OMe SAM in air as a function of exposure time to natural light. The modes indicating crystalline OEG molecules in helical conformation, as well as the CH₃ rocking mode indicating the presence of the CH₃ end group and the part of the C-O-C mode indicating amorphous structure decreased in intensity. This indicates a degeneration of the OEG moiety of the SAM. Spectral modes which can be assigned to ester and formate groups increased, indicating that these compounds are end products of the degeneration of the SAM. Note that the modes indicating helical conformation increased in intensity in between the first and the second measurement. Since the SAM was grown in water and the first measurement was made immediately after the growth, the helical part is distorted by residual water for this first measurement.

EG₆OMe solution for about 1 minute on fresh gold wafers cleaned with UV treatment and EtOH rinsing and on the same substrates subsequently cleaned again and again with this treatment. Comparing the data sets, no systematic increase or decrease in the modes characterising the OEG moiety (see 4.2.1) with a rising number of UV cleaning cycles was found, see Fig.4.4.2. There is variation in the strength of the modes, which is randomly distributed showing the great sensitivity of the SAM growth. These results verify, that it is possible to use gold samples with previous grown SAMs again with no measurable influence on the SAM structure. It is, however, necessary to clean the substrates using the method above prior to each self assembly process and to check the substrates for physical damage as it may arise from dewetting. The ability to reuse substrates is especially valuable for components which are difficult to produce, such as large gold-coated quartz blocks or customized substrates.

4.4.2 Stability in air

When comparing spectra of SAMs, measured at different times after growth, it is important to know if the SAM is stable in air rather for hours, days or weeks and how long it takes until degradation effects are visible in the spectrum. Therefore, SAMs stored

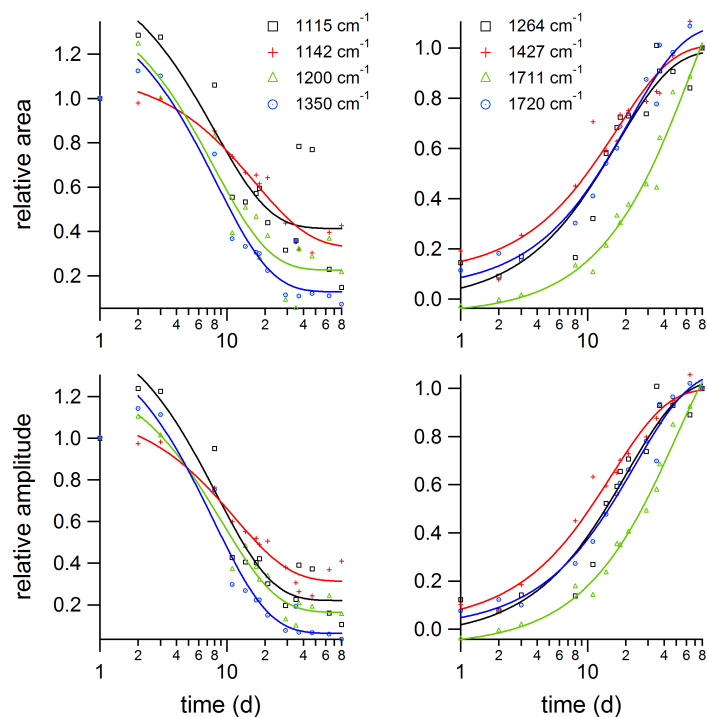


Figure 4.4.4: Kinetic fit of spectral characteristics, from the spectra shown in Fig. 4.4.3 as a function of exposure time to natural light. For visualisation in one graph the values are normalized to the magnitudes at the start for the modes arising from the intact OEG moiety and long time for the modes indicating the degeneration products. The amplitude and area of the Gaussian fits of the modes follow an exponential behaviour. The modes indicating a helical conformation of the OEG moiety, as well as the CH₃ rocking mode indicating the presence of the CH₃ end group and the part of the C-O-C mode indicating amorphous structure decreased in area and intensity. The time constants for the decrease of the area and amplitude of modes indicating amorphous structure are bigger, than the ones for the modes indicating helical structure. The values of the spectral modes which can be assigned to ester and formate groups increased. The time constants of the of the modes indicating ester groups are smaller than the time constants of the mode indicating formate groups.

under different conditions were measured over increasing periods of time. As a model system, EG₆OMe SAMs grown over night in a 500 μ M ethanolic EG₆OMe solution were used. First, a series of SAMs stored in light-transmissive containers was measured. Figure 4.4.3 shows the evolution of the spectrum of a EG₆OMe SAM in air as a function of exposure time to natural light. Already after three days, there are significant changes in SAM structure, notably a decrease in the intensity of vibrational modes indicating a helical structure and the emergence of modes of degradation products. After two weeks the spectrum has changed dramatically, implying a notable degradation of the SAM.

For a detailed analysis it is focused on the individual modes. As explained in Sec. (4.2.1), highly ordered EG₆OMe SAMs adopt a predominantly helical conformation, giving rise to characteristic modes: the low frequency component of the C-O-C stretching vibration at 1114 cm^{-1} , the EG CH₂ twisting vibration at 1244 cm^{-1} , the EG CH₂ wagging vibration at 1348 cm^{-1} and the EG CH₂ scissoring vibration at 1463 cm^{-1} . In addition the existence of the CH₃ end group of EG₆OMe can be proved with the CH₃ rocking vibration at 1200 cm^{-1} (compare to Tab. 4.2.1 and [46]).

On the other hand, spectra of SAMs exposed to natural light over long times show modes, which can be attributed to esters and formates. Namely the absorption modes at 1740 cm^{-1} and 1712 cm^{-1} can be allocated to the C=O stretching vibration of ester and formate groups respectively [33, 35, 121]. The mode at 1460 cm^{-1} can be allocated to the C-H asymmetrical deformation vibration of esters [121] and the mode at 1264 cm^{-1} can be allocated to the C-O-C stretching vibration if one of the C atoms is esterified to C=O [121, 122].

In order to get a qualitative understanding of the underlying conversion a fitting procedure of the modes, as described in Sec. 3.3.8, 3.3.9 and 3.3.10 was performed. In Fig.4.4.4A the time evolution of the amplitude and area of the modes of the helical part of the OEG SAM and the CH₃ rocking mode indicating the presence of the CH₃ end group are plotted as a function of time. The amplitude and the area of all four modes decreased following a single exponential behaviour, indicating a steady-going degradation process. The time constants concerning the modes assigned to the helical structure and the CH₃ rocking mode are similar suggesting a real degradation of the molecules rather than a conformational change. Also, the intensity of the absorption modes of the alkane linker between the sulfur atom and the OEG moiety, which can be found in the CH₂ stretching region of the spectra decreased, indicating a degradation of the complete SAM rather than only the OEG part. However, the decrease of the modes of the OEG part was more pronounced, indicating a higher stability of the alkane part. Figure 4.4.4B shows the time evolution of the amplitude and the area of the modes of the ester and formate degradation products. The time constants of the increase of the amplitude and the area of the modes are similar for all four modes and also to the time constants of the decrease of the modes of EG₆OMe molecules in helical conformation and the CH₃ end group.

As described in Sec. 2.3.5 esters and formates are the two main products of the degeneration of PEG exposed to light with $\lambda \geq 300\text{nm}$ [33]. Qin et al. [36] also found formates

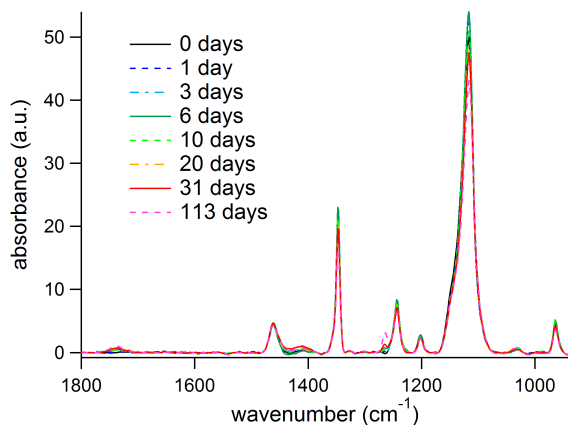


Figure 4.4.5: Spectra of an EG₆OMe SAM in air as a function of storage time in the dark. The intensity of the modes indicating crystalline ordered OEG molecules in helical conformation, as well as the CH₃ rocking mode indicating the presence of the CH₃ end group and the part of the C-O-C mode indicating amorphous structure decreased. This indicates a degeneration of the OEG moiety of the SAM. However, the decrease of the modes is significantly slower than in the case of a SAM under light exposure. The intensity of the spectral modes which can be assigned to ester and formate groups increased, indicating that these compounds are end products of the degeneration of the SAM. Note that the intensity of the modes indicating helical conformation increased in between the first and the second measurement. Since the SAM was grown in water and the first measurement was made immediately after the growth, the helical part is distorted by residual water for this first measurement.

and esters as the main products, studying the degradation of OEG molecules with 3 EG units. Knowing this results, it was expected to find these products on our substrates after the exposure of OEG SAMs to natural light. Morlat et al. [33] concluded that for photo-oxidation formates are the main products rather than esters. In our experiments, however, esters are the main products. One explanation may be the following. Morlat et al [33] were investigating the degradation of long PEG molecules in bulk phase. There the scission products are still relatively long chains remaining in solution. In our case the molecules are much shorter, so a number of the formate products after β -scission (compare to Sec. 2.3.5) are short-chained. If a alkoxy radical is formed, attacking the first available carbon atom from top, methyl formate and a macroradical comprising the remaining part of the EG₆OMe molecule are formed. Methyl formate has a boiling point of 32 °C and it is likely that it evaporates shortly after formation at room temperature. This evaporation of short chained formates may explain the modes indicating formates in the infrared spectra measured during degradation are rather weak. In addition to the kinetics of degradation, it was studied if the degradation products are still chemisorbed on the surface or only physisorbed. To this end the samples being exposed to light for 80 days were rinsed with EtOH and the resulting spectra were compared to measurements before rinsing. Results showed a further decrease in the intensity of modes attributed to the OEG moiety of the SAM and alkane spacers and a strong decrease in

the modes indicating the degradation products, esters and formates. This shows that many molecules were only physisorbed and washed away during rinsing. Reasons for this behaviour may be the scission of the OEG chains during oxidation (compare to 2.3.5) as well as the oxidation of the sulfur atoms due to the UV part of the light (compare to 4.4.1).

Also, a series of SAMs stored in the same containers, but in the dark, was measured (Fig.4.4.5). Even after long storage times (weeks) there was only small change in the spectra, the decrease of the modes which can be assigned to the not oxidized part of the SAM and the modes assigned to the oxidation products are significantly smaller than for a similar SAM exposed to natural light. In Fig.4.4.6A the time evolution of the amplitude and area of the modes of the helical part of the OEG SAM and the CH_3 rocking mode indicating the presence of the CH_3 end group are plotted as a function of time, their decrease is following a single exponential behaviour. Figure 4.4.6B shows the time evolution of the amplitude and area of the modes of the ester and formate degradation products; their increase follows a single exponential behaviour. Qualitatively the results are quite similar to the results for the SAMs exposed to air. However, the quantity of degradation is significantly lower. The results are indicating a much higher stability of the SAMs in the dark compared to the exposure to natural light, which is consistent with literature [34] considering photo-oxidation of the ethylene glycol part as the major process of SAM degradation at room temperature, see also Fig. 4.4.7.

4.4.3 Degeneration effects in air at 60 °C

In Sec. 2.3.5 a overview over oxidative degeneration effects of PEG molecules is given. In addition to oxidation activated by light exposure, there are also oxidation effects activated by elevated temperatures. In chapter 4.5 conformational changes of EG_6OMe at elevated temperatures up to 65 °C were investigated. Since oxidative effects will play a role in this temperature regime [33] they should be studied at a fixed temperature. The SAM was heated up to 62 °C and its long time behaviour was studied at this temperature (data not shown). There was only a small change in the OEG moiety, which is supposed to be due to the high disorder at elevated temperature even for fresh SAMs. However, an increase of absorption modes of products could be monitored, especially the band indicating esters at 1260 cm^{-1} . After 5 days the sample were rinsed with water. In contrast to the longtime degeneration experiments under the influence of natural light, the rinsing had only a small effect on the modes indicating the OEG moiety and indicating the degeneration products, suggesting that the thiol bonds are mostly intact and that most of the degeneration products are still covalently bound to the substrate, indicating the reaction to esters.

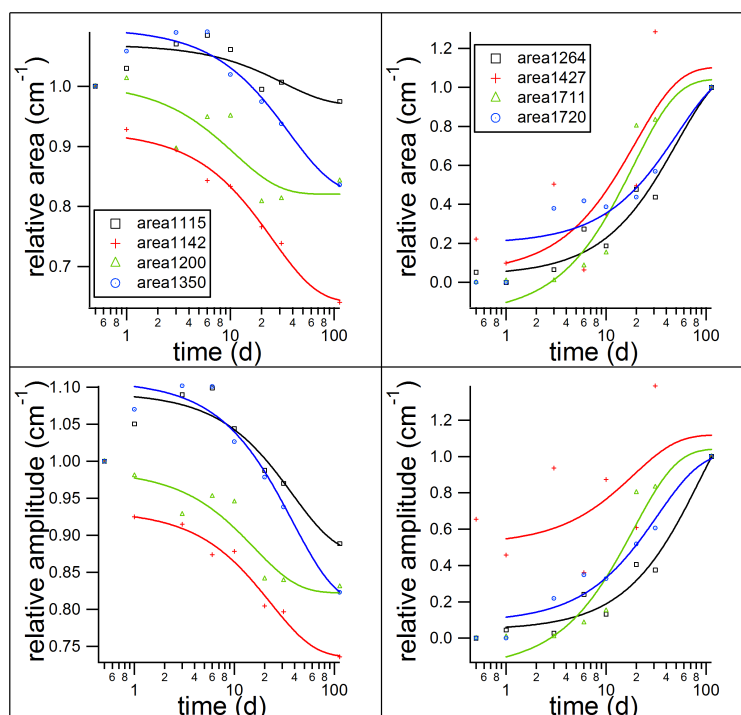


Figure 4.4.6: Kinetic fit of spectral characteristics, from the spectra shown in Fig. 4.4.5 as a function of time. For visualisation in one graph the values are normalized to the magnitudes at the start for the modes arising from the intact OEG moiety and long time for the modes indicating the degeneration products. The amplitude and area of the Gaussian fits of the modes follow an exponential behaviour. The modes indicating a helical conformation of the OEG moiety, as well as the CH_3 rocking mode indicating the presence of the CH_3 end group and the part of the C-O-C mode indicating amorphous structure decreased in area and intensity. The time constants for the decrease of the modes indicating amorphous structure are bigger, than the one for the modes indicating helical structure. The intensities of the spectral modes which can be assigned to ester and formate groups increased. The time constants of the of the modes indicating ester groups are smaller than the time constants of the mode indicating formate groups.

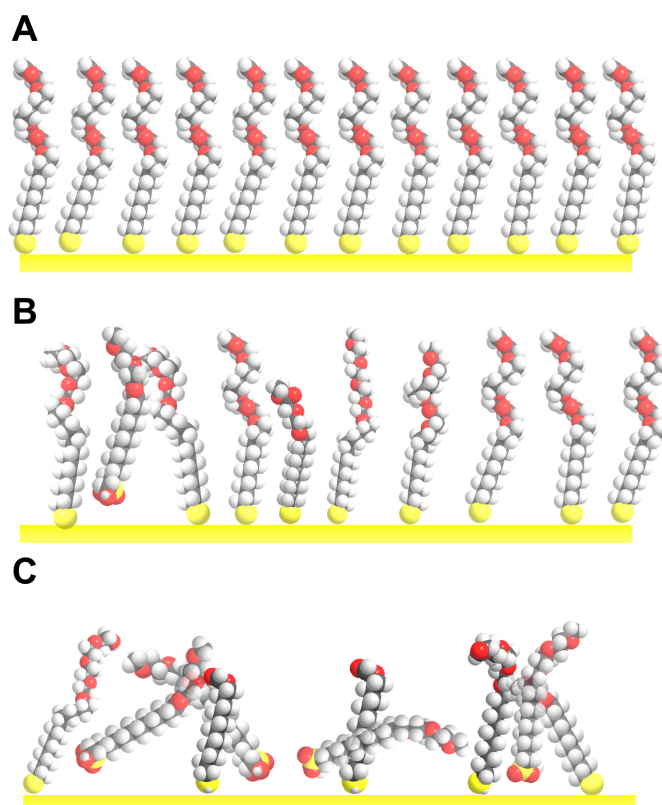


Figure 4.4.7: Degeneration effects during the longtime storage of EG₆OMe in air under exposure to natural light are shown, starting with a very high coverage SAM (A), after two weeks significant changes in the absorption spectra can be seen (B). Due to formation of esters and formates a big fraction of molecules is no longer stabilized in the helical conformation. The chains of molecules reacting to formates are truncated (see Fig. 2.3.3). Additionally, the UV part in the natural light is inducing a oxidation of sulfur atoms. Therefore, a significant fraction of the SAM molecules is only physisorbed on the surface and can be removed by rinsing with solvent. With progressing exposure time an increasing number of molecules in the SAM is affected (C) by degradation and due to a lack of orientation of the molecules, spectral modes are nearly vanishing.

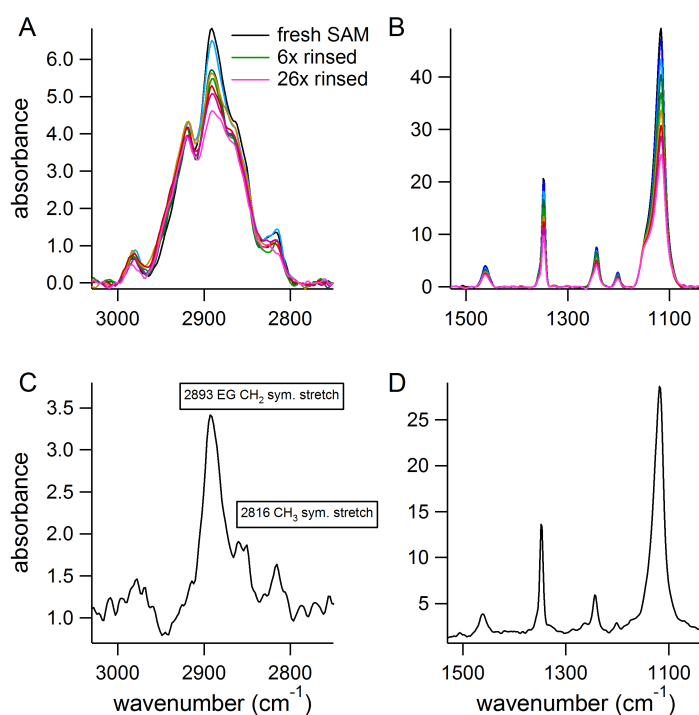


Figure 4.4.8: Spectra of EG₆OMe SAM measured in air after repeated reimmersion in EtOH and successively drying. Figures A and B show the evolution of the spectra in the CH region and the fingerprint region respectively. With the increasing number of immersion cycles the modes indicating a crystalline OEG moiety decreased successively, indicating an increasing disorder. Figures C and D represents difference spectra of the spectrum of the fresh SAM and the SAM after 26 reimmersion cycles. Note especially, that the absorption bands indicating a helical structure and indicating the presence of the CH₃ head group decreased in intensity, whereas the absorption modes indicating an ordered alkane spacer are not affected. This is suggesting, that mainly the OEG moiety is disordered during repeated reimmersion.

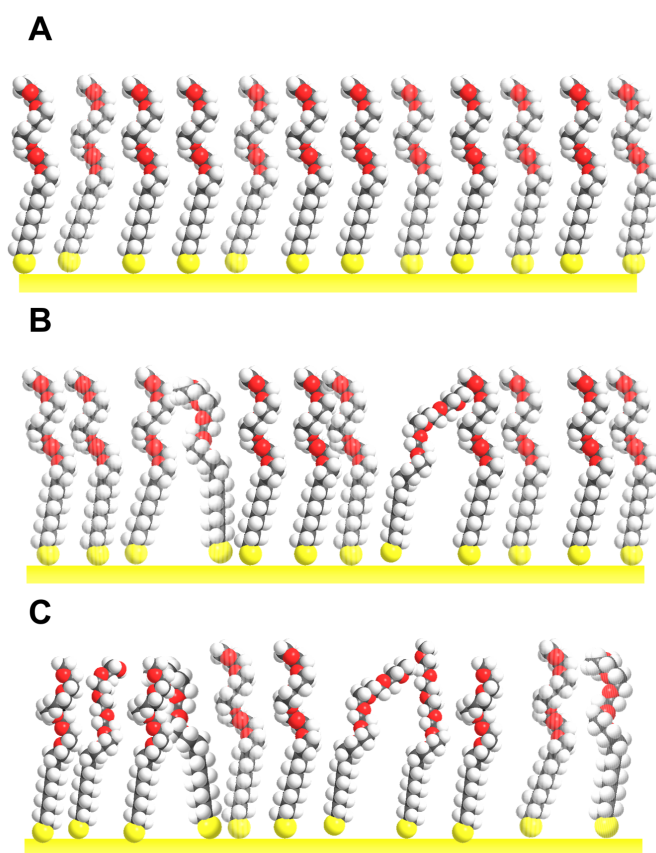


Figure 4.4.9: The effect of repeated immersion and drying of a SAM is shown. After a couple of cycles a significant number of molecules, do no longer adopt an crystalline structure. The starting points of this process may be defect sites or phase boundaries (B). With an increasing number of cycles more and more molecules are no longer in helical crystalline structure. Since only the modes indicating helical structure are decreasing it is assumed that the molecules themselves remain on the SAM, their OEG moieties, however, become more and more disordered.

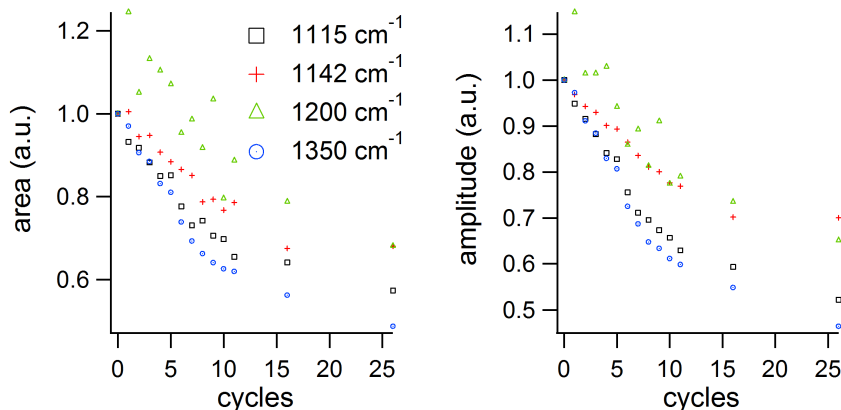


Figure 4.4.10: Plot of the area and amplitude of characteristic modes of the spectra of the EG₆OMe SAM measured in air after repeated reimmersion in EtOH and successively drying. The modes indicating a ordered OEG moiety decrease exponentially, suggesting a decreasing order of this part of the SAM.

4.4.4 Stability during repeated drying and reimmersion

A substantial part of this thesis focuses on the effects of water on the structure of OEG SAMs. Therefore, it is crucial to compare the SAM structure with and without surrounding solvent. As described in Sec. 4.2.3, OEG SAMs undergo a conformational change on exposure to an aqueous environment. Due to SAM water interactions OEG moieties in helical conformation become amorphous if water molecules are able to penetrate the SAM. For the comparison of the spectra of SAMs in different environments it is important to know if OEG SAMs partly dissolve, degrades or change its structure during repeated immersion in solvents. To investigate this behaviour, again a model system is used, an EG₆OMe SAM grown in a 500 μ M ethanolic EG₆OMe solution over night. First, the SAM was rinsed repeatedly with EtOH for about 3 seconds, dried successively and a spectrum was measured after each cycle. The intensity of the absorption modes of the SAM indicating a helical structure subsequently decreased, indicating that the SAM is altered, compare to Fig. 4.4.8. Figure 4.4.10 shows the area, amplitude, width and peak position as a function of the number of reimmersion in EtOH. The decrease of the area and the amplitude of the modes follows an exponential behaviour, for the first 10 steps a linear behaviour can be approximated. Additionally, the decrease in intensity is the same for the modes associated with the helical conformation and the CH₃ rocking mode. The intensity of the part of the C-O-C peak indicating an amorphous structure does not decrease, which is discussed in the next paragraph. The width and peak position are not changing significantly suggesting no substantial structural and conformational change in the remaining OEG molecules. In Fig. 4.4.8C the difference spectrum of the EG₆OMe SAM prior to the rinsing process and that after 25 rinsing steps is shown. It reveals in the C-O-C region modes indicating helical conformation and the CH₃ rocking mode, however

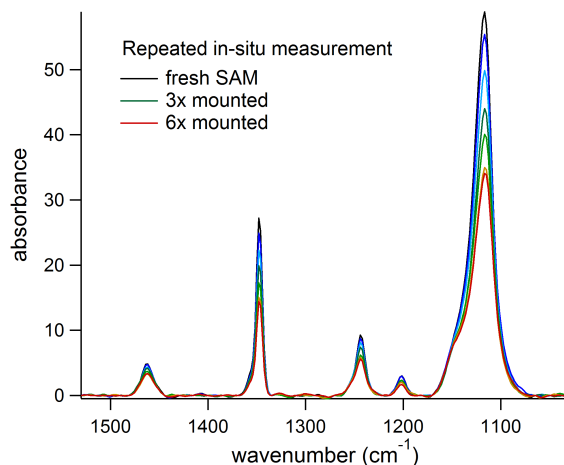


Figure 4.4.11: Spectra of EG₆OMe SAM measured in air after repeated measurements in an aqueous environment in our thin liquid cell. The change of the intensity of the spectral modes is qualitatively very similar to the change for repeated rinsing with EtOH, suggesting a similar degeneration mechanism.

not the part of the C-O-C peak indicating an amorphous structure. This supports our results from the spectral mode fit: the number of molecules of the OEG moiety adopting a crystalline structure and a helical conformation continuously decrease with each reimmersion and drying step. The difference spectrum shows in the CH₃ region virtually only modes of the OEG moiety and of the CH₃ rocking vibration, indicating that the alkane linkers of the OEG molecules are largely still on the surface and oriented as before the reimmersion cycles. The amphiphilic character of the OEG molecules may help to explain these findings. These molecules exhibit a polar OEG part, which interacts with polar molecules as water (compare to [47] and Sec. 4.2.3) and EtOH and a non polar alkane part close to the substrate, whose interaction with polar solvents is so weak that it could not be detected with Sum frequency spectroscopy [28, 29]. From the literature it is known that there are also desorption effects from thiol SAMs in solution [1, 118]. The rate of desorption further depends on the crystallinity of the SAM: the higher the crystallinity the slower the rate of desorption. However, these effects take part on a time scale of hours rather than seconds and cannot be accounted for the monitored large alteration of spectra after short immersion times. Even so, they may contribute to the small decrease of the modes indicating alkanes in the CH₃ region. The fraction of molecules in crystalline structure and helical conformation decreased gradually which each rinsing step, this may support the idea that in dense packed defect free regions helical conformation, being in water free condition the energetically most favorable state [57], is restored after drying, while near defect sites the well ordered structure is irreversibly lost. It implies further, that these amorphous regions spread with increasing number of reimmersion cycles.

Additionally, alternating measurements in air and in water, using our thin liquid layer cell were performed, compare to Fig.4.4.11. The results are comparable with our findings

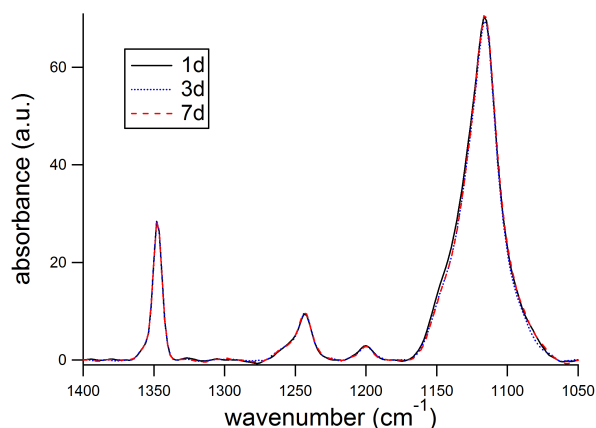


Figure 4.4.12: Spectra of EG₆OMe SAM after growth in aqueous environment; the times (1 day, 3 days, 7 days) are times after start of the growth. No significant changes are observed, providing good evidence for long-term stability under these conditions.

for the experiments where SAMs were rinsed briefly with EtOH, if one estimates two reimmersion events per *in-situ* measurement. The sample is dried when it is removed from the cell and dried again after cleaning. These results indicate that the reason for the decreasing order in subsequently *in-situ* measurements is the amorphization of the OEG part of the SAM due to repeated drying and reimmersion. For a visualisation of the results see Fig. 4.4.9.

4.4.5 Stability in solution over long time period

The stability of OEG SAMs in solution is a very important point for many applications. To figure out possible structural changes in solution SAMs grown in solution in a home-built thin liquid cell over long periods of time, were monitored. The sample was at room temperature and not exposed to light during and in between the measurements. There was no drying and reimmersion in between the measurements. Fig.4.4.12 shows spectra taken over the range of 6 days after the complete growth of the SAM. As one can see, there is no significant change in SAM structure, indicating a high stability. The results of the kinetic fit, regarding area, amplitude, with and position of the modes shown in Fig(4.4.13) underline this result. Interestingly, the spread of the values around the mean value has a difference variance, indicating a different error of the mode fits. Following this argumentation the wagging mode is fitted with the lowest error and CH₃ rocking peak with the highest one. Considering the small area of the CH₃ rocking mode and the fact, that the C-O-C peak consists of multiple absorption modes this ranking seems to be reasonable. It was also studied whether the storage of SAMs in high concentrated SAM solution (2 mM EG₆OMe in H₂O) affects its structure, also here no significant changes were observed, compare to Fig.(4.4.14). These findings are consistent with long term biofouling experiments, showing that surfaces functionalized with OEG SAMs preserve

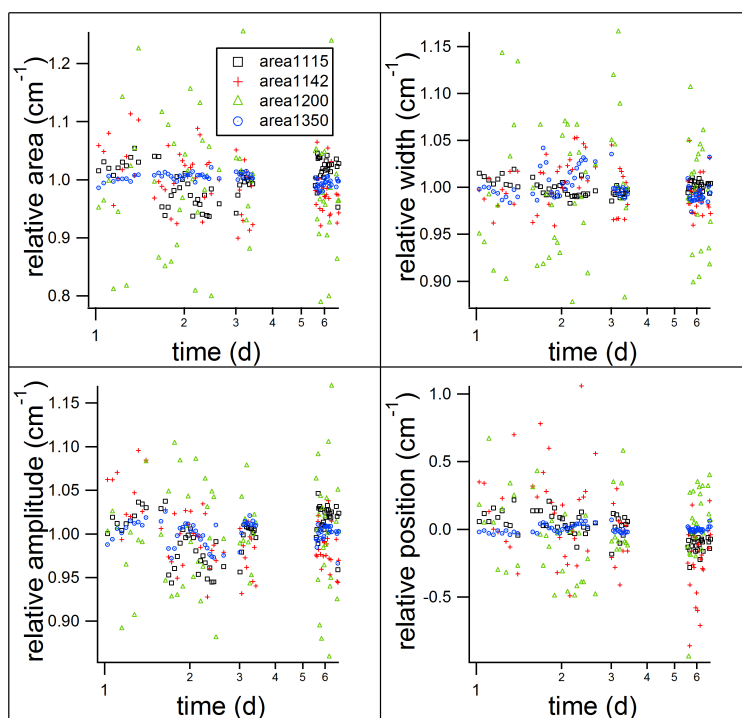


Figure 4.4.13: Kinetic fit of spectral characteristics of a EG₆OMe SAM after growth in aqueous environment as a function of time after start of the growth. For visualisation in one graph the values are normalized to the mean magnitudes. One can see that amplitude, area, width and position of the modes are spreading around the mean value. There is no difference in this behaviour regarding the modes indicating a helical conformation (low frequency C-O-C mode and wagging mode), all-*trans* conformation (high frequency C-O-C mode) and the CH₃ rocking mode indicating the presence of a CH₃ end group. This is indicating a stable SAM in the monitored time window. However, the spread of the values around the mean value has a difference variance, indicating a different error of the mode fits.

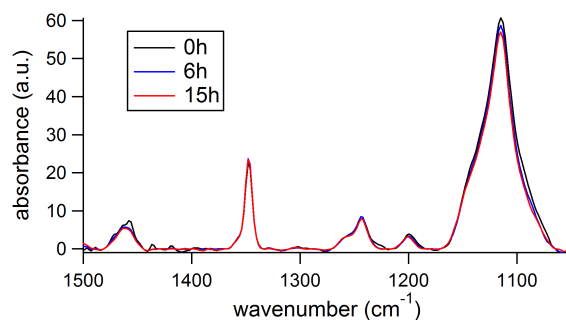


Figure 4.4.14: Spectra in aqueous environment of EG₆OMe SAM grown over night in bulk solution. The times refer to the immersion time in 2 mM EG₆OMe after growth. No significant changes are observed, providing good evidence for long-term stability under these conditions.

their non fouling properties in protein solutions over weeks at temperatures up to 37 °C [36]. They are also consistent with the results that *poly*(ethylene glycol) oxidizes less readily in solution than in air, due to the dissolution and diffusion of radicals in solution [1, 36], compare to the long time stability of OEG SAMs in the dark (4.4.2).

4.4.6 Conclusion

Our experiments show that OEG SAMs are fairly stable over time if they are stored and treated under appropriate conditions regarding light exposure, reimmersion and temperature. OEG SAMs degrade predominantly via exposure to light, especially UV light, by repeatedly drying and reimmersion and at temperatures higher than 40 °C (see Sec. 4.5.2). By avoiding the exposure of OEG SAMs to such conditions they can be stabilized over weeks without serious structural degradation. These findings underline the importance of *in-situ* measurements for dynamical processes such as SAM growth in solution and may help to understand longtime biofouling properties of OEG SAMs.

4.5 Temperature behaviour of EG₆OMe SAMs in solution

An important application of OEG SAMs are biological experiments, which are usually performed at temperatures higher than room temperature. Therefore, it is of great interest if the SAMs structure and the properties are altered at elevated temperature, especially concerning the biofouling properties. Moreover, there are mixed SAMs whose protein resistant properties can be switched by a temperature change [117, 123]. The understanding of immersion effects of OEG SAMs may contribute to a understanding of those systems. For this reason, after the interaction of EG₆OMe SAMs with water as a function of surface coverage was studied, an interesting point was to analyze changes of this interaction at elevated temperatures. The same vibrational modes in the fingerprint region were monitored as for the *in-situ* growth of EG₆OMe SAMs (for an overview see section 4.2.1). The measurements were started at room temperature (about 22 °C) and the temperature was increased in steps of 2.5 K. In order to obtain an equilibration of the system, the measurement was performed 10 min after reaching the temperature for each measurement. For an evaluation of structural changes, the behaviour of the modes indicating a helical structure was monitored, the low frequency component of the C-O-C stretching mode, the CH₂ twisting mode and the EG CH₂ wagging mode as well as the high frequency component of the of the C-O-C mode indicating an all-*trans* structure.

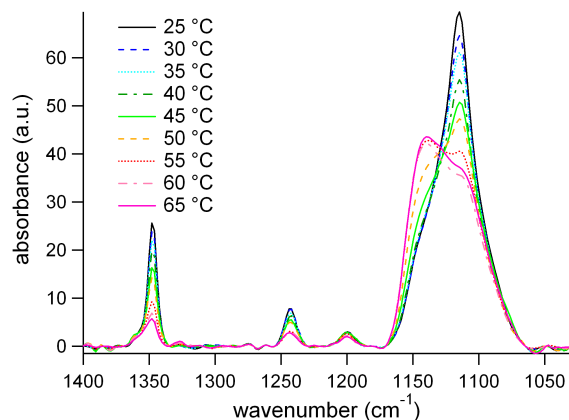


Figure 4.5.1: Spectra of an EG₆OMe SAM in aqueous environment as a function of temperature up to 65 °C. The intensity of the low frequency part of the C-O-C stretching mode, the EG CH₂ twisting mode and the EG CH₂ wagging mode are decreasing with rising temperature, while the intensity of the high frequency part of the C-O-C stretching mode is increasing. This is indicating a change from predominant helical to mixed helical all-*trans* conformation.

4.5.1 Temperature range up to 40 °C

First, the focus is on the temperature region of 22 °C to 40 °C. Fig.4.5.1 shows the spectra of a SAM grown in the sample cell as described in Sec. 4.2 and then monitored at elevated temperatures without changing the environment apart from the temperature. As can be seen, there is a gradual decrease of the modes indicating helical structure with increased temperature, while the mode indicating all-*trans* structure is increasing. The width and position of the helical modes is not changing, implying that there are no substantial structural changes (see Fig.4.5.2). The conformational change may be due to a change of the intra- and intermolecular interaction of the OEG molecules or a change of the interaction with water. Valiokas et al. [37] measured the conformational changes of hexa (ethylene glycol) thiol SAMs on gold containing amide groups, under vacuum conditions. At elevated temperatures, they observed a change from helical to all-*trans* conformation. However, the transition occurred at higher temperatures (around 60 °C) compared to our experiments. A reason for this behaviour may be due to the different molecules used, those containing an amide group in between the alkane spacer and the OEG moiety of the molecules, may be able to form intermolecular hydrogen bridges and stabilize the structure.

Another argument may be the interaction between the SAM and water molecules in our experiment. Considering a higher degree of freedom of the ethylene glycol moiety at elevated temperature, it might be easier for water to penetrate the SAM. Its interaction with the lone-pairs of the oxygen atoms in the ethylene-glycol moiety may ease conformational changes. Additionally, further gauche defects could be introduced due to hydrogen bridging of water molecules.

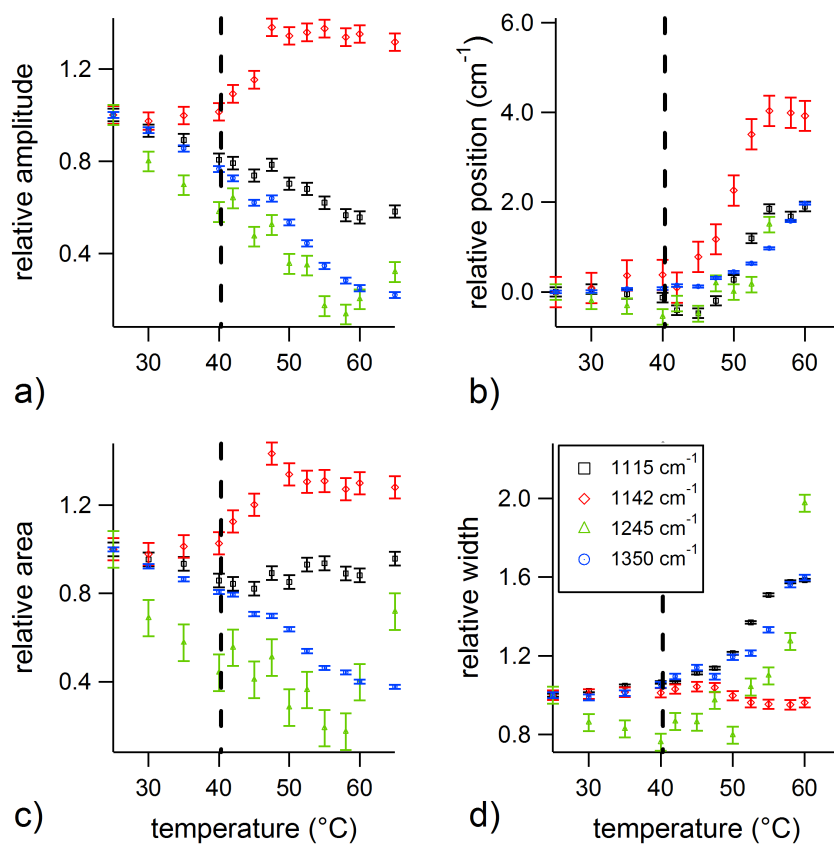


Figure 4.5.2: Spectral characteristics as a function of temperature up to 65 °C. For visualization in one graph, the values are normalized to the magnitudes at 25 °C. The error bars show the combined uncertainties related to the measurement and fitting. In A and C one can see that the Gaussian fits of area and amplitude of the modes indicating a helical conformation are decreasing, whereas the values of the high frequency mode of the C-O-C peak are increasing slightly indicating a decrease in helical structure. In B and D it becomes obvious that there are two temperature regimes - below and above 45 °C. It can be seen that there is an increase in width and a shift in mode position starting at about 45 °C, indicating structural changes.

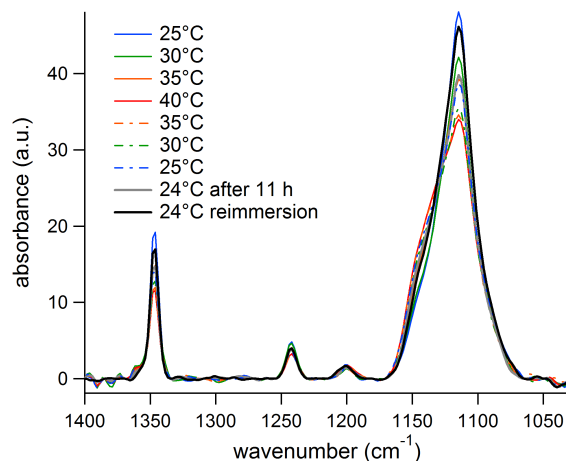


Figure 4.5.3: Evolution of the spectral modes of an EG₆OMe SAM in aqueous environment during heating from 25 °C up to 40 °C and cooling down to 25 °C. The conformational changes are not reversible in solution, even after 11 h. However, after drying and reimmersion, the predominantly helical conformation is restored.

It is hard to distinguish the destabilising effects caused by the lack of amide groups on the one hand and water at the other hand, since both exhibit a quite similar result - a decrease in order and an decrease of the fraction of molecules in helical conformation. To shed light into this issue, the reversibility of this conformational change was investigated. The transition monitored by Valiokas et al. [45] was completely reversible and the reordering occurred on a five minutes timescale. In Fig.4.5.3, *in-situ* spectra of a EG₆OMe SAM being heated up from 25 °C to 40 °C and cooled down to 25 °C again are shown. Our measurements show that the transition from helical to mixed helical all-*trans* conformation takes place on a similar timescale as described in Valiokas et al. [45], however the changes were not reversible within minutes when cooling down the system. After decreasing the temperature again to room temperature, the molecules stayed in the conformation they adopted at higher temperature and even after several hours there was no substantial change. Drying the SAMs in an argon stream after the *in-situ* temperature scans and monitoring under water after reimmersion led to a return to a conformation close to the initial, see Fig.4.5.3. The reversibility is virtually complete, degeneration effects described in Sec. 4.4.4 hinder absolute reversibility. This leads to the conclusion that more water molecules were able to penetrate into the SAM at elevated temperature which induces a conformational change of the OEG moiety. Further, this may support the idea that these water molecules are tightly bound to the OEG-layer [20]. Only drying in air is able to release the water enabling the OEG molecules to adopt their original conformation. This is another indication for the relatively strong binding of water molecules to the ethylene glycol moiety and its importance for OEGs biofouling properties.

This result is only in apparent conflict with the observations during SAM growth in Sec. 4.2. There, an increase of the fraction of the OEG moiety in helical conformation

and an improved crystallinity over time was observed. Drying and reimmersion of the OEG SAMs after *in-situ* growth did not lead to an additional increase in order. However, there is an important difference between these experiments. During SAM growth, the binding of more thiol molecules to the surface is a driving force for a structural change and may press water out of the OEG moiety. When decreasing the temperature, there is no such driving force, being able to disrupt the water-SAM interaction in the OEG moiety once the water molecules have penetrated the SAM. In addition to energetic effects, also entropic aspects may be considered. In Ref. [124] the change in entropy due to the binding of water molecules to the ethylene glycol moiety and their relation to the change in energy is discussed. Since the entropy gain due to water molecules leaving the SAM in the bulk solution is partly compensated by the loss of entropy of the SAM due to higher crystallinity, energetic effects are believed to play a more prominent role [124].

4.5.2 Temperature range above 40 °C

In a next step, the behaviour of OEG SAMs at temperatures up to 65 °C was investigated. As can be seen in Fig. 4.5.1, there is a change in the ratio of the absorbance of the modes indicating a helical structure and the mode indicating an all-*trans* structure. In addition, there is a change in mode position and width, starting at a temperature between 40 and 50 °C, see Fig.4.5.2. This suggests an increase of disorder within the OEG moiety and therefore an increase in amorphous structure. Further, those changes of the SAM conformation and structure are no longer reversible. Neither cooling the SAMs down to room temperature nor drying and successive reimmersion them were able to restore their initial conformation. This strongly implies that parts of the OEG moiety are changed irreversibly. It is known from the literature [36] that OEG SAMs are very stable in solution at temperatures up to 37 °C. Qin et al. reported that OEG SAMs stored for 4 weeks in PBS solution at 37 °C were still protein resistant. However, bulk phase experiments monitoring the stability of *poly*(ethylene glycols) in solution at elevated temperatures revealed that at 50 °C, the molecules are oxidized [33]. Therefore, the irreversible change in structure of the OEG moiety at temperatures above 50 °C may be attributed to oxidation. For the mechanism of the oxidation of PEG see Sec. 2.3.5 and for a discussion of the reaction in our experiment see Sec. 4.5.4 and Sec. 4.4.2.

4.5.3 Temperature dependence for different coverage

In Sec. 4.2.3 it was shown, that the OEG SAM conformation in aqueous conditions strongly depends on coverage, related to the SAMs growth state. In this section the influence of SAM coverage on the conformational transition behaviour should be elucidated. To this end, SAMs of different coverage, apparent in a different ratio of the intensities of the high- and low-frequency mode of the C-O-C band, were monitored at elevated temperatures. As can be seen by comparing Fig. 4.5.1 and Fig. 4.5.4, at room temperature,

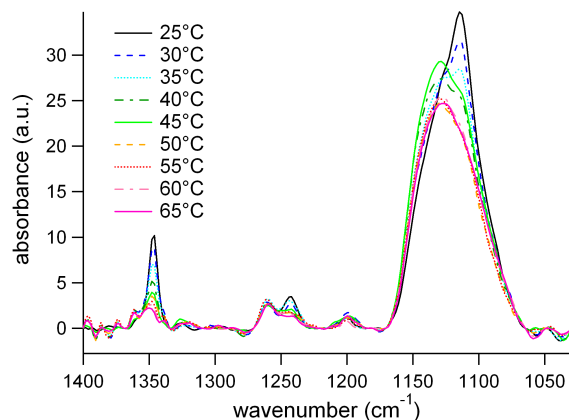


Figure 4.5.4: Spectra of an EG₆OMe SAM in aqueous environment as a function of temperature up to 65 °C. Due to a lower coverage compared to the SAM in Fig.4.5.1 the conformational and structural change takes place in a lower temperature regime, the spectrum at 65 °C is indicating an amorphous structure.

SAMs have different fractions of helical structure depending on the surface coverage. For all SAMs, the modes indicating a helical structure are decreasing with rising temperature, starting at 30 °C. For high coverage SAMs, however, the conformational change starts at lower temperatures and the structure gets amorphous at 40 °C, whereas the structure remains crystalline and only the conformation is changing up to a temperature of 40 °C for very high coverage SAMs. This suggests that the higher the SAMs surface coverage, the higher its stability towards temperature induced changes in conformation. The reasons for this behaviour may be an interplay of interaction of SAM molecules with each other and its change with increasing temperature. Water may have easier access to the OEG moiety at higher temperatures due to an enhanced conformational freedom. The effect of decreasing crystallinity especially for not very high coverage SAMs may be based on a deeper penetration of water molecules and their stronger interaction with the SAM.

4.5.4 Measurements in air

To learn more about the influence of water, information about the structural change in air is needed. Since a direct comparison with literature concerning the behaviour of EG₆OMe in air is not possible, see Sec. 4.5.1, reference measurements in air were performed. In order to exclude effects of different surface coverage, measurements in air and water using SAMs grown for the same time in bulk solution were compared. Figure 4.5.4 shows the temperature dependent behaviour of EG₆OMe SAMs grown in bulk solution over night under aqueous conditions, Fig.4.5.5 shows the corresponding spectra of a SAM grown at the same conditions in air. There are two findings: First, when comparing the SAMs in aqueous environment and in air, it is obvious that there is an interaction between SAM and water in aqueous environment, resulting in a decrease

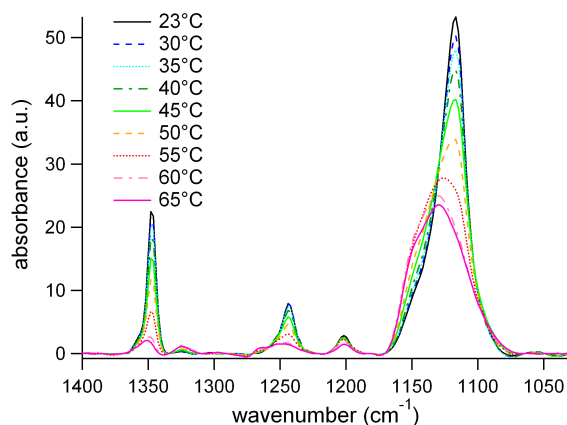


Figure 4.5.5: Spectra of an EG₆OMe SAM in air as a function of temperature up to 65 °C. The conformational change occurs at higher temperature than in aqueous environment, indicating that a amorphization induced by the penetration of water molecules into the OEG moiety of the SAM promotes a structural change at higher temperature. At about 65 °C the SAM adopts an amorphous structure, additionally the CH₃ rocking mode is decreasing indicating degeneration effects, presumably by thermal oxidation.

in the SAMs order at room temperature, compare to Sec. 4.2.3. Second, it can be seen that the conformational change of the SAM in aqueous environment is starting at a lower temperature than the one of the SAM in air. At 40 °C the SAMs vibrational modes under water indicate a virtually amorphous structure while the spectra in air still show a predominantly crystalline structure in helical conformation. This is further evidence for the enhancing influence of water molecules penetrating the SAM on the transition process.

4.5.5 Reversibility of conformational change in air

To test whether the conformational transition of the OEG moiety in air is reversible disregarding oxidation effects, an experiment involving a very short time period at high temperatures was performed. The temperature was increased in the water bath to 65 °C and then pumping of the hot water into the sample cell was started, resulting in a heating from 25 °C to 62 °C within 5 min. The temperature was kept constant for 5 min, to attain an equilibrium and then another 7 min for the measurement. Afterwards, the cell was cooled down to 25 °C with cold water within 10 min. A comparison of the spectra before and after heating showed a conformational change in the SAM from predominantly helical to mixed all-*trans* and helical (data not shown). The successive cooling led to a reordering to a predominantly helical conformation. The intensity of the modes indicating a helical conformation was only slightly weaker after the temperature step, than before the heating. This indicates only minor degradation effects, likely to occur during the short period at elevated temperature. It further suggests that disregarding degeneration

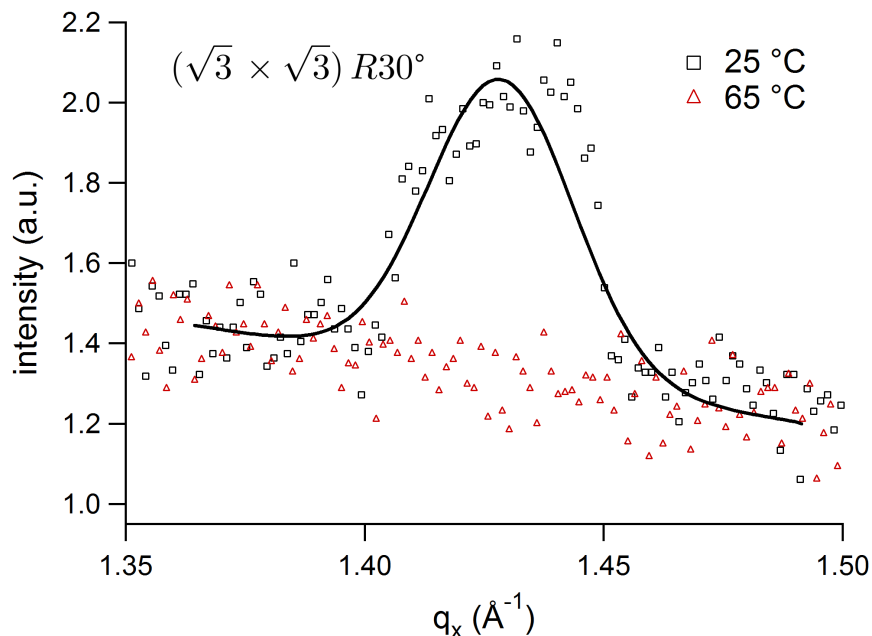


Figure 4.5.6: The plot shows Bragg peaks of the EG₆OMe thiol SAM grown on top of a thin polycrystalline Au layer measured with GIXD. At a temperature of 25 °C, the $(\sqrt{3} \times \sqrt{3})$ peak of the thiol SAM can be seen, indicating a crystalline structure. After increasing the temperature to 65 °C the $(\sqrt{3} \times \sqrt{3})$ thiol peak disappears, indicating a loss in crystalline structure.

effects, the conformational changes on EG₆OMe SAMs in air are reversible within a few minutes, similar to the findings of Valiokas et al. [37].

4.5.6 In plane structure measured with grazing incidence X-ray scattering

Complementary to the infrared experiments in plane grazing incidence X-ray diffraction measurements were performed to monitor the influence of rising temperature on the crystalline structure of EG₆OMe thiol SAMs. In the following section a proof of principle measurement done during a commissioning experiment at beamline I07 at the Diamond synchrotron facility is described. As substrates, silicon wafers coated with a 20 nm thick polycrystalline but (111) textured Au layer on top of a 5 nm thick Cr adhesion layer were used. The SAM was grown in a 500 μm ethanolic solution of EG₆OMe thiol over night. The scattering profile was measured along the q_x (i.e. in-plane) coordinate with an area detector. First, a measurement was performed at 25 °C. The measurements were performed at a light incidence angle θ of 0.17° (compare to Fig. 3.5.1), well below the total reflectivity edge of Au which for 20 keV is at 0.228°. It was possible to identify the Au in-plane peak of the (10L) crystal truncation rods at $q_x = 2.51\text{\AA}^{-1}$ (see Fig. 4.5.6 and compare to Ref. [125]). It was used for a calibration of the setup. Using Eq. 3.5.3,

Eq. 3.5.4 and the lattice plane distance $d = 2.50\text{\AA}$ the exact distance between sample and detector could be calculated to $L = 1231\text{mm}$, consistent with the specification of the setup. Additionally, a peak at $q_x = 1.44\text{\AA}^{-1}$ could be detected. Alkane thiols adopt a $(\sqrt{3} \times \sqrt{3})R30^\circ$ structure on top of the Au lattice [3, 59], so the (11) thiol peak in q_x direction should be at a position with the factor $1/\sqrt{3}$ lower with respect to the position of the Au in-plane peak, coincident with the peak found. This suggests, that also OEG thiols adopt the structure found for alkanethiols on Au (111) [3, 126]. EG₆OMe has an alkane linker segment between the thiol group and the OEG moiety. Additionally, there is a nearly perfect match between the cross-section area of the OEG helix and the thiol packing density [127]. Thus, a similar alignment of alkane- and OEG-thiols on a Au(111) surface is reasonable. An other peak at $q_x = 1.24\text{\AA}^{-1}$ could not be assigned, neither to a structural feature of the Au layer, nor to a one arising from the thiol SAM. The measurement was repeated several times on the same spot, in order to elucidate if there is any beam damage. A comparison of the diffraction curve of the first measurement and the last measurement of this series shows no disturbance of the crystalline structure could be detected under the conditions employed.

After measuring the in-plane structure at 25 °C the temperature was increased to 65 °C which led to the disappearance of the Bragg reflection peak, indicating a loss of crystallinity at 65 °C (or below) for this SAM. Note, though, that the temperature stability is expected to depend on the coverage [3] and therefore these data should not be taken as an intrinsic equilibrium melting curve as in Ref. [128]. For alkane thiol SAMs the loss of hexagonal order occurs at temperatures, which depend on chain length and on surface coverage. For a full coverage alkane C₁₀ alkane SAM this loss in crystalline structure occurs at about 100 °C, the alkane spacer of EG₆OMe SAMs contains 11 carbon atoms so a loss in hexagonal order at a temperature of 65 °C (well below the melting point of a full coverage decane thiol SAM) may indicate an incomplete surface coverage. A loss in crystalline structure of the EG₆OMe SAM at 65 °C has also been observed in the infrared studies.

It could be shown that EG₆OMe thiol SAMs exhibit at 25 °C an in-plane peak indicating a crystalline structure on Au(111), according to a $(\sqrt{3} \times \sqrt{3})R30^\circ$ structure, in accordance with the literature values for alkane SAMs [3, 127], for OEG SAMs no GIXD data is available, yet. At a temperature of 65 °C, this peak disappeared, suggesting a melting of the crystalline order. To characterize the temperature dependence of this melting, a series of measurements would be necessary. Additionally, measurements under aqueous conditions could complement our *in-situ* infrared measurements in Sec. 4.5.1 and Sec. 4.5.2. In order increase the signal to noise ratio further experiments may be done with SAMs grown on a single crystalline Au(111) substrate.

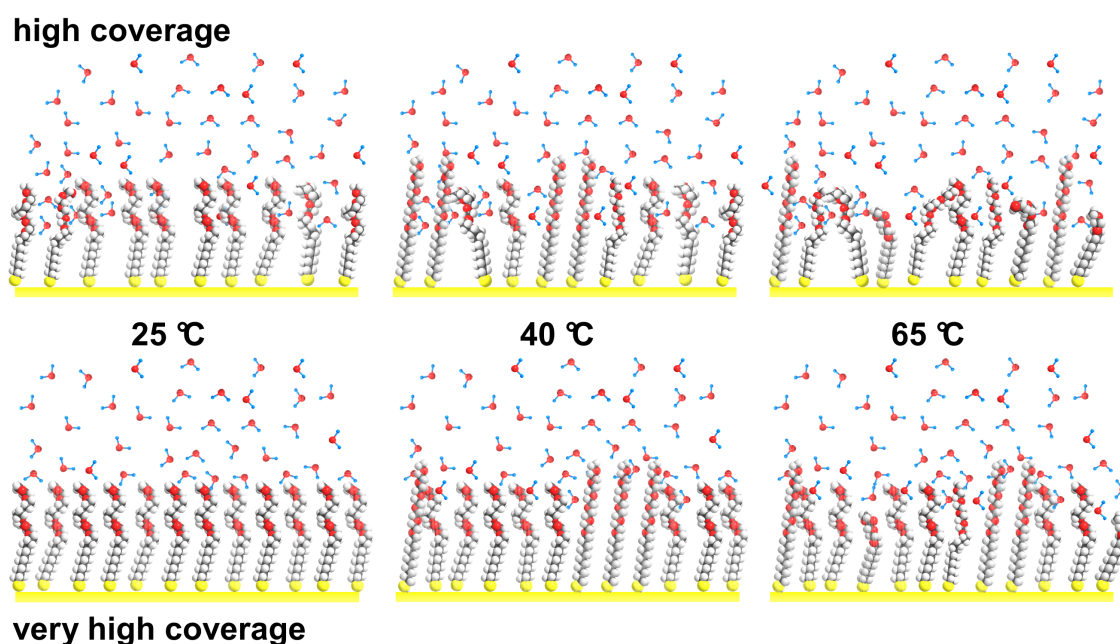


Figure 4.5.7: Schematic of the temperature behaviour of EG₆OMe SAMs in aqueous environment for different surface coverage. In A SAMs are shown at a temperature of 25 °C. While the OEG moiety of the high coverage SAM is interacting with water molecules, in case of the very high surface coverage water molecules are not able to penetrate the SAM, expressing in a higher crystalline order of the latter one at 25 °C. In B the behaviour of the SAMs at a temperature of about 40 °C is shown. While the OEG moiety of the high coverage SAM strongly interacts with water molecules giving rise to an increasing amorphization of the SAM additional to a transformation in a mixed helical all trans formation, the structure of the SAM with very high surface coverage remains crystalline and the interaction with water rather weak. In C the behavior above temperatures of 50 °C are shown. Additionally, to the change in structure a degradation occurs with irreversibly changes to the SAM and an increasing amorphization.

4.5.7 Conclusion

In this section the conformational change of EG₆OMe in aqueous environment at elevated temperatures was investigated. A conformational change, indicated by a decrease of modes arising from helical structure and an increase of the high frequency C-O-C stretching mode suggesting all-*trans* structure could be observed. Under aqueous conditions, the process is not reversible even after several hours. However, after a drying and reimmersion of the SAM, the conformational change was almost reversible for $T \leq 40$ °C. At $T > 40$ °C the conformational changes proceed and a broadening and shifting of the vibrational modes indicating structural changes could also be monitored. It is assumed, that oxidative degeneration is responsible for this behaviour. Indeed, the conformational change is not reversible for $T > 40$ °C neither under aqueous conditions nor after drying and reimmersion. The conformational change is dependent on the surface coverage. Whereas the SAM remains in crystalline order and only changed its conformation for nearly complete coverage, for high coverage structural changes could also be observed at high temperatures, as revealed by an amorphization of the SAM. Our results can give important clues about the stability of SAMs and the strength of their interaction with water. Further, they can help to explain the behaviour of SAMs regarding biofouling and structural integrity at elevated temperatures.

Chapter 5

Outlook

This part of the thesis is dedicated to give perspectives and ideas for future work, based on the present results. A strength of the *in-situ* studies presented in this thesis is the presence of thin, confined liquid layers. The samples are prepared with a thin liquid layer and not touched for the period of the measurements. This is perfect in terms of stability of the setup and for comparison of relative changes in spectral modes. However, for some kinds of experiments this may also be an restriction. It has been shown that it is also possible to prepare the sample in a different way (see Sec. 3.3.7.1) and to vary the thickness of the water layer in a reproducible way. This offers the possibility to use of our thin liquid layer cell as a “quasi flow-cell”. During measurements, the thickness of the water layer can be changed by moving the stage. It can be directly controlled by analyzing the PMIRRAS spectrum and comparing it to calculations. In between the measurements the gap can be increased allowing a exchange of the solvent. This allows measurement under different conditions regarding ionic strength, pH value as well as a test of protein resistance and protein interaction with the SAM under *in-situ* conditions. In case of a change in surface coverage as for SAM growth and protein adsorption these “bulk” measurements could be complemented by SPR measurements of the interaction of identically functionalized surfaces and so structural information can be interpreted quantitatively as a function of surface coverage.

A second point regards the variation of the OEG molecules. In this work *in-situ* measurements with the model system EG₆OMe thiols on gold were established. The terminal group of the thiols has an effect on the OEG structure and its biofouling properties, while the chain length of OEG molecules and the introduction of stabilising groups in between the alkane linker and the OEG moiety have a big impact on their conformation. A systematic variation of these structural parameters could complement the picture of SAM solvent interaction.

Another very interesting point is the in-plane structure of OEG SAMs. Using single crystalline gold substrates, it could be determined with grazing incidence X-ray scattering. The effect of increasing temperature, changing pH value, etc. on the in-plane structure

would also be an interesting objective. This data would nicely complement the structural data measured with PMIRRAS. It is also known that PEG thiol SAMs grow in islands. It would be exciting to know if OEG SAMs also grow in islands and how grain boundaries and regions containing molecules with different structure and conformation are distributed in-plane. A suitable technique to elucidate this point is tip enhanced Raman spectroscopy, measuring characteristic spectral modes and providing a sufficient lateral resolution.

Chapter 6

Conclusion

The aim of this work was to characterize the interaction of *oligo*(ethylene glycols) with water molecules under *in-situ* conditions. The results for the model system EG₆OMe contribute to a general understanding of protein resistance and may be adopted for other protein resistant SAMs. Together with the optimization of the experimental setup and the data analysis for this kind of measurements, they form a fundament for the development and understanding of more complex and specialized experiments.

First, the technical improvements are summarized. With the help of the Fresnel coefficients, it is possible to calculate the intensity change of light passing a layered system. This calculation was included in a Igor Pro routine in form of Hansen's matrix formalism. The theoretical calculations were validated with experimental results from PMIRRAS measurements in air and in aqueous environment. Therefore, an EG₆OMe SAM grown on a gold sample was used as a model system. The measurements in aqueous environment were carried out using a home-built thin liquid cell. The measured signal strength were conform with the calculated ones over a broad angular range for measurements in air as well as in aqueous environment.

In order to compare the signal strength of the *in-situ* measurements at different angles with each other and with the calculated values, it was necessary to control the thickness of the thin water layer above the substrate. To this end, ellipsometric measurements were used. However, it would be much more convenient to deduce the signal strength directly from the PMIRRAS spectra. It could be shown that the results gained by comparison of the PMIRRAS average signal ($\frac{1}{2}(R_s + R_p)$) with the corresponding calculated signal are in agreement with the ellipsometric data and the IRRAS data. This enables the determination of the thickness of the water layer during real time measurements without changing the setup.

A further important tool for comparing spectral data quantitatively is its normalization. A normalization procedure from literature was adapted and it was shown that the correction spectra needed for this method are not substrate specific, allowing to utilize the method with only one additionally measurement instead of five. Additionally, it was shown that

the procedure is also valid for substrates with rather thin metal layers and differences in the reflection of s- and p-polarized light.

When performing real time measurements with PMIRRAS, large quantities of spectra which have to be baseline corrected, compared and fitted in terms of mode strength are generated. To this end, a routine in Igor Pro for automatically importing spectra and carrying out reproducible baseline correction and spectral mode fitting was developed. The program can easily be adapted to different spectral regions and different modes and proved to be a valuable tool for our real time *in-situ* measurements.

Finally, in the technical section the development of substrates was reported, enabling PMIRRAS measurements of silane SAMs on silicon oxide surfaces. The PMIRRAS principle is based on the surface selection rule for polarised light on conducting surfaces, which is basically valid only for metal surfaces. However, simulations performed with the simulation program described above showed, the attenuation of the signal by a thin dielectric layer to be small, as long as its thickness is small compared to the range of the evanescent field above the surface. The range of this field is about some 100 nm. In cooperation with I. Dunlop, a thin silica layer was sputtered on top of a thick titanium layer and functionalized with PEG2000-biotin silanes. Parts of the fingerprint region were shadowed by the strong SiO and SiO₂ absorption bands arising from the thin SiO layer. Nevertheless, the PEG2000 layer could be identified by characteristic absorption modes with a good signal to noise ratio. Moreover, a resistant behaviour of the SAM against unspecific protein adsorption while specifically binding streptavidin could be monitored, indicating a complete coverage of the SAM and biotin linkers to be available. Further experiments in cooperation with N. Schweizer with PEG chains of different length showed, that the binding capacity of PEG-biotin strongly decreased for long PEG6000 chains in comparison to shorter PEG2000 and PEG900 chains, presumably due to a burying of the biotin linkers inside the PEG moiety due to a collapsed structure of long PEG chains.

The PMIRRAS spectra of PEG2000 on Si-Ti-SiO_x substrates were compared with transmission spectra of silicon substrates functionalized with PEG2000 silanes, showing a much better signal to noise ratio for the new substrates. The characteristic PEG modes were only slightly above the noise level in the transmission measurements. Moreover a subtraction of H₂O vibration rotation bands had to be performed. This underlines the practical use of the Si-Ti-SiO_x substrates.

Using this technical framework, it was possible to design complex real time *in-situ* experiments to broaden the understanding of the interaction of OEG SAMs with water. The growth and reordering behaviour of EG₆OMe thiols on gold was investigated for the first time with PMIRRAS under *in-situ* conditions. It is known from literature, that it was not possible to describe the conformational evolution during growth of EG₆OMe SAMs quantitatively, when applying *ex-situ* infrared spectroscopy. The deviations in growth constants for different samples were too big for meaningful time series. This problem was bypassed by monitoring the SAM growth process on one and the same sample, measured in real time under aqueous conditions. The growth and reordering of the SAM was mon-

itored starting at an intermediate growth state and the evolution of modes attributed to different conformations was analyzed. Starting with a mixed helical and all-*trans* conformation, the number of molecules in helical-*trans* conformation increased over time and the crystalline order of the SAM improved resulting in a red shift of the absorption modes and a narrowing of the width of their width. A kinetic fit revealed a single exponential behaviour of the reordering.

Also the interaction of the OEG moiety with water molecules was monitored qualitatively as a function of surface coverage, by stopping the growth at different stages and measuring reference spectra of the SAMs in air. For low coverage, the SAM structure was rather unordered in air as well as under aqueous conditions. High coverage SAMs, adopt in air a crystalline structure and a helical conformation. However, measurements under aqueous conditions revealed a structure with many gauche defects indicating a penetration of water molecules interacting with the OEG moiety. Interestingly, for OEG SAMs with a very high coverage no difference between the modes measured in air and under water was observed. This indicates that the water molecules cannot penetrate the SAM and interact with the OEG moiety when the surface coverage is very high. Experiments of Vanderah et al. [31], showed that OEG SAMs are protein resistant for high coverage, but not for very high coverage. In combination with our results, this illustrates the high importance of water molecules bound in the interior of the OEG moiety for the prevention of unspecific biofouling.

It was assumed, that the surface coverage changes only slightly during the monitored reordering of the molecules. This view is supported by the fact, that the CH₃ rocking mode, being independent of the SAMs conformation, did not change significantly. In cooperation with S. Jäger this assumption could be verified by SPR measurements, monitoring the change in surface coverage of the SAM during growth and comparing infrared spectra of the so grown SAMs. Mixed SAMs produced by incubating EG₆OMe SAMs with different growth times in amid thiol solution also showed a indirect proportionality between the amid absorption modes indicating the ratio of vacant binding positions as a function of growth time of the SAM and the intensity of the CH₃ rocking mode as a function of the SAMs surface coverage. This also supports the assumption, that the reordering occurs at nearly full surface coverage of the SAM.

A reason for many conflicting reports concerning protein resistant behaviour of *oligo* (ethylene glycols) which can be found in literature are degradation effects and different conditions regarding SAM preparation and storage. In order to shed light into this field, a systematic study of degradation and long time stability of OEG SAMs was performed, using the model system EG₆OMe. The cleaning of gold substrates using ozone producing UV light was investigated and it could be shown that the number of cleaning cycles has no commensurable impact on the growth of EG₆OMe SAMs on these substrates, indicating perfectly clean surfaces. Further, structural changes of EG₆OMe SAMs exposed to ambient atmosphere and natural light were investigated. The intensity of the vibrational modes associated with the OEG moiety decreased exponentially, simultaneously the ab-

sorption modes of the degradation products, esters and formates, increased. Successive rinsing of the substrates led to a further decrease of modes associated with the OEG moiety and to a decrease of the intensity of absorption modes assigned to the degradation products as well. This implies that thiol groups are oxidized by the UV part of natural light additionally to the degradation of the SAMs OEG moiety. EG₆OMe SAMs stored at ambient atmosphere but in the dark exhibited only a small decrease in the intensity of the absorption modes assigned to the OEG moiety. This suggests that light exposure is a driving force for SAM degradation at room temperature. Finally, the stability of EG₆OMe SAMs under aqueous conditions was investigated. SAMs stored in solution turned out to be very stable against degradation effects. A SAM grown in our thin liquid cell showed not even a small structural change after six days, consistent with previous findings, reporting OEG SAMs to be stable resistant against unspecific protein adsorption for one month if stored in Buffer solution at 37 °C. However, SAMs are very sensitive to repeated reimmersion and drying. Even after a single drying and reimmersion cycle the structural effect is visible. After 10 cycles a large-scale distortion of the spectra occurs. Our result suggest an amorphization of the SAM as a consequence of repeated reimmersion. Long time experiments showed that the effect is not reversible.

Often, protein resistant SAMs are used above room temperature. Therefore, in the last part of this work the temperature behaviour of EG₆OMe SAMs under aqueous conditions is monitored. With increasing temperature, the number of the molecules in helical conformation is getting smaller and the crystallinity of the SAM is decreasing. For the temperature region below 40 °C, the change in structure is reversible. Interestingly, it is not reversible in solution. Only after drying and reimmersion the conformational status before temperature elevation can be recovered. This suggests that the water molecules are strongly bound in the OEG moiety and a driving force is needed to remove them. This can be a chemisorption of additional thiol molecules during grow or drying in air. At temperatures above 40 °C, a further decrease of the molecules in helical conformation takes place, along with the crystallinity of the structure decreasing quickly. The loss of crystalline structure measured by PMIRRAS could be confirmed by GIXD results. The transition is rather abrupt than continuous. Further the conformational change is not reversible, neither by cooling down nor by drying and reimmersion. This suggests an oxidation of the SAM at temperatures above 40 °C, consistent with literature. SAMs measured in air have a higher stability towards the temperature induced conformational change, underlining the interaction of the SAM with H₂O molecules.

List of abbreviations

Molecules

OEG	<i>Oligo</i> (ethylene glycols)
PEG	<i>Poly</i> (ethylene glycols)
EG	Ethylene glycols
BSA	Bovine serum albumin
DNA	Desoxyribonucleic acid
GOPTS	3-Glycidyloxypropyl-trimethoxysilane
DIC	Diisopropylcarbodiimide
DAPEG	Di-amino- <i>poly</i> (ethylene glycol)
TBTU	Tetra methyluronium tetrafluoroborate
Amidethiol	11-Mercaptoundecanamide

Experimental techniques

IR	Infrared
FTIR	Fourier transform spectroscopy
IRRAS	Infrared reflection absorption spectroscopy
PMIRRAS	Polarization modulation infrared reflection absorption spectroscopy
SPR	Surface plasmon resonance
XRR	X-ray reflectivity
XPS	X-ray photoelectron spectroscopy

GIXD	Grazing incidence X-ray diffraction
SFG	Sum frequency generation
RifS	Reflectometric onterference spectroscopy
QCM	Quarz micro balance
TEM	Transmission electron microscopy
STEM	Scanning transmission electron microscopy
HAADF	High-angle annular dark field
STEM	Scanning transmission electron microscopy
EELS	Electron energy-loss spectroscopy

Miscellaneous

SAM	Self assembled monolayer
EtOH	Ethanol
PEM	Photo elastic modulator
PM	Polarization modulated
DFT	Density functional theory
FWHM	Full width at half maximum
DLVO	Derjaguin Landau Verwey Overbeek
DF	Dark field

Bibliography

Bibliography

- [1] J. C. Love, L. A. Estroff, J. K. Kriebel, R. G. Nuzzo, and G. M. Whitesides, *Chem. Rev.* **105**, 1103 (2005): *Self-Assembled Monolayers of Thiolates on Metals as a Form of Nanotechnology.*
- [2] M. Mrksich and G. M. Whitesides, *Annu. Rev. Biophys.* **25**, 55 (1996): *Using Self-Assembled Monolayers to Understand the Interactions of Man-made Surfaces with Proteins and Cells.*
- [3] F. Schreiber, *Prog. Surf. Sci.* **65**, 151 (2000): *Structure and Growth of Self-Assembling Monolayers.*
- [4] F. Schreiber, *J. Phys. Condens. Matter* **16**, R881 (2004): *Self-assembled monolayers: from 'simple' model systems to biofunctionalized interfaces.*
- [5] A. Ulman, *Chem. Rev.* **96**, 1533 (1996): *Formation and Structure of Self-Assembled Monolayers.*
- [6] B. Ratner and S. Bryant, *Annu. Rev. Biomed. Eng.* **6**, 41 (2004): *Biomaterials: Where we have been and where we are going.*
- [7] J. Sagiv, *J. Am. Chem. Soc.* **102**, 92 (1980): *Organized monolayers by adsorption. 1. Formation and structure of oleophobic mixed monolayers on solid surfaces.*
- [8] R. G. Nuzzo and D. L. Allara, *J. Am. Chem. Soc.* **105**, 4481 (1983): *Adsorption of bifunctional organic disulfides on gold surfaces.*
- [9] S. T. Patton, K. C. Eapen, J. S. Zabinski, J. H. Sanders, and A. A. Voevodin, *J. Appl. Phys.* **102**, 024903 (2007): *Lubrication of microelectromechanical systems radio frequency switch contacts using self-assembled monolayers.*
- [10] M. Péter, X.-M. Li, J. Huskens, and D. N. Reinhoudt, *J. Am. Chem. Soc.* **126**, 11684 (2004): *Catalytic Probe Lithography: as Catalyst-Functionalized Scanning Probes as Nanopens for Nanofabrication on Self-Assembled Monolayers, .*
- [11] C. A. Mirkin and M. A. Ratner, *Annu. Rev. Phys. Chem.* **43**, 719 (1992): *Molecular Electronics.*

- [12] H. Lang, C. Duschl, and H. Vogel, *Langmuir* **10**, 197 (1994): *A new class of thiolipids for the attachment of lipid bilayers on gold surfaces.*
- [13] C. Boozer, S. Chen, and S. Jiang, *Langmuir* **22**, 4694 (2006): *Controlling DNA Orientation on Mixed ssDNA/OEG SAMs.*
- [14] S. Dobretsov, H. U. Dahms, and P. Y. Qian, *Biofouling* **22**, 43 (2006): *Inhibition of biofouling by marine microorganisms and their metabolites.*
- [15] Y. Guo, M. Li, A. Mylonakis, J. Han, A. G. MacDiarmid, X. Chen, P. I. Lelkes, and Y. Wei, *Biomacromolecules* **8**, 3025 (2007): *Electroactive Oligoaniline-Containing Self-Assembled Monolayers for Tissue Engineering Applications, .*
- [16] I. E. Dunlop, S. Zorn, G. Richter, V. Srot, M. Kelsch, P. A. van Aken, M. Skoda, A. Gerlach, J. P. Spatz, and F. Schreiber, *Thin Solid Films* **517**, 2048 (2009): *Titanium-silicon oxide film structures for polarization-modulated infrared reflection absorption spectroscopy.*
- [17] J. Mehne, G. Markovic, F. Pröll, N. Schweizer, S. Zorn, F. Schreiber, and G. Gauglitz, *Anal. Bioanal.Chem.* **391**, 1783 (2008): *Characterisation of morphology of self-assembled PEG monolayers: a comparison of mixed and pure coatings optimised for biosensor applications.*
- [18] K. A. Marx, *Biomacromolecules* **4**, 1099 (2003): *Quartz crystal microbalance: A useful tool for studying thin polymer films and complex biomolecular systems at the solution-surface interface.*
- [19] R. G. Chapman, E. Ostuni, S. Takayama, R. E. Holmlin, L. Yan, and G. M. Whitesides, *J. Am. Chem. Soc.* **122**, 8303 (2000): *Surveying for Surfaces that Resist the Adsorption of Proteins.*
- [20] R. L. C. Wang, H. J. Kreuzer, and M. Grunze, *Phys. Chem. Chem. Phys.* **2**, 3613 (2000): *The interaction of oligo(ethylene oxide) with water: a quantum mechanical study.*
- [21] S. Herrwerth, W. Eck, S. Reinhardt, and M. Grunze, *J. Am. Chem. Soc.* **125**, 9359 (2003): *Factors that Determine the Protein Resistance of Oligoether Self-Assembled Monolayers - Internal Hydrophilicity, Terminal Hydrophilicity, and Lateral Packing Density.*
- [22] S. Zorn, N. Martin, A. Gerlach, and F. Schreiber, *Phys. Chem. Chem. Phys* **12**, 8985 (2010): *Real-time PMIRRAS studies of in situ growth of C11Eg6OMe on gold and immersion effects.*
- [23] M. Skoda, R. Jacobs, S. Zorn, and F. Schreiber, *J. Electron. Spectrosc. Relat. Phenom.* **172**, 21 (2009): *Optimizing the PMIRRAS signal from a multilayer system and application to self-assembled monolayers in contact with liquids.*

-
- [24] W. Hansen, *J. Opt. Soc. Am* **58**, 380 (1968): *Electric Fields Produced by the Propagation of Plane Coherent Electromagnetic Radiation in a Stratified Medium*.
- [25] T. Buffeteau, B. Desbat, D. Blaudez, and J.-M. Turllet, *Appl. Spectrosc.* **54**, 1646 (2000): *Calibration procedure to derive PM-IRRAS spectra from IRRAS spectra*.
- [26] T. Buffeteau, B. Desbat, and J. M. Turllet, *Appl. Spectrosc.* **45**, 380 (1991): *Polarization Modulation Ft-Ir Spectroscopy of Surfaces and Ultra-Thin Films - Experimental Procedure and Quantitative-Analysis*, .
- [27] V. Tolstoy, I. Chernyshova, and V. Skryshevsky, *Handbook of Infrared Spectroscopy of Ultrathin Films* (2002).
- [28] M. Zolk, F. Eisert, J. Pipper, S. Herrwerth, W. Eck, M. Buck, and M. Grunze, *Langmuir* **16**, 5849 (2000): *Solvation of Oligo(ethylene glycol)-Terminated Self-Assembled Monolayers Studied by Vibrational Sum Frequency Spectroscopy*.
- [29] R. Y. Wang, M. Himmelhaus, J. Fick, S. Herrwerth, W. Eck, and M. Grunze, *J. Chem. Phys.* **122**, 164702 (2005): *Interaction of self-assembled monolayers of oligo(ethylene glycol)-terminated alkanethiols with water studied by vibrational sum-frequency generation*.
- [30] J. Fick, R. Steitz, V. Leiner, S. Tokumitsu, M. Himmelhaus, and M. Grunze, *Langmuir* **20**, 3848 (2004): *Swelling Behavior of Self-Assembled Monolayers of Alkanethiol-Terminated Poly(ethylene glycol): A Neutron Reflectometry Study*, .
- [31] D. J. Vanderah, H. La, J. Naff, V. Silin, and K. A. Rubinson, *J. Am. Chem. Soc.* **126**, 13639 (2004): *Control of Protein Adsorption: Molecular Level Structural and Spatial Variables*.
- [32] H. Ron, S. Matlis, and I. Rubinstein, *Langmuir* **14**, 1116 (1998): *Self-Assembled Monolayers on Oxidized Metals. 2. Gold Surface Oxidative Pretreatment, Monolayer Properties, and Depression Formation*.
- [33] S. Morlat and J.-L. Gardette, *Polymer* **42**, 6071 (2001): *Phototransformation of water-soluble polymers. I: photo- and thermooxidation of poly(ethylene oxide) in solid state*.
- [34] M. Donbrow, in *Stability of the polyoxyethylene chain*, Vol. 23 of *Surfactant Science Series*, nonionic surfactants: physical chemistry ed., edited by M. J. Schick (1987), pp. 1011–1067.
- [35] C. Wilhelm and J.-L. Gardette, *Polymer* **39**, 5973 (1998): *Infrared analysis of the photochemical behaviour of segmented polyurethanes: aliphatic poly(etherurethane)s*.

- [36] G. Qin and C. Cai, Chem. Commun. **105**, 5112 (2009): *Oxidative degradation of oligo(ethylene glycol)-terminated monolayers.*
- [37] R. Valiokas, M. Ostblom, S. Svedhem, S. C. T. Svensson, and B. Liedberg, J. Phys. Chem. B **104**, 7565 (2000): *Temperature-Driven Phase Transitions in Oligo(ethylene glycol)-terminated Self-Assembled Monolayers.*
- [38] C. Joachim, J. K. Gimzewski, and A. Aviram, Nature **408**, 541 (2000): *Electronics using hybrid-molecular and mono-molecular devices.*
- [39] D. M. Yebra, S. Kiil, and K. Dam-Johansen, Prog. Org. Coat. **50**, 75 (2004): *Antifouling technology - past, present and future steps towards efficient and environmentally friendly antifouling coatings.*
- [40] N. K. Chaki and K. Vijayamohanan, Biosens. Bioelectron. **17**, 1 (2002): *Self-assembled monolayers as a tunable platform for biosensor applications.*
- [41] R. Murugan, P. Molnar, R. Koritala Panduranga, and J. J. Hickman, Int. J. Biomed. Eng. Technol. **2**, 104 (2009): *Biomaterial surface patterning of self-assembled monolayers for controlling neuronal cell behaviour.*
- [42] D. Falconnet, D. Pasqui, S. Park, R. Eckert, H. Schiff, J. Gobrecht, R. Barbucci, and M. Textor, Nano Lett. **4**, 1909 (2004): *A Novel Approach to Produce Protein Nanopatterns by Combining Nanoimprint Lithography and Molecular Self-Assembly.*
- [43] E. Ostuni, R. G. Chapman, R. E. Holmlin, S. Takayama, and G. M. Whitesides, Langmuir **17**, 5605 (2001): *A Survey of Structure-Property Relationships of Surfaces that Resist the Adsorption of Protein.*
- [44] H. Rieley, G. K. Kendall, F. W. Zemicael, T. L. Smith, and S. Yang, Langmuir **14**, 5147 (1998): *X-ray Studies of Self-Assembled Monolayers on Coinage Metals. 1. Alignment and Photooxidation in 1,8-Octanedithiol and 1-Octanethiol on Au.*
- [45] R. Valiokas, L. Malysheva, A. Onipko, H.-H. Lee, Z. Ruzele, S. Svedhem, S. C. Svensson, U. Gelius, and B. Liedberg, J. Electron. Spectrosc. Relat. Phenom. **172**, 9 (2009): *On the quality and structural characteristics of oligo(ethylene glycol) assemblies on gold: An experimental and theoretical study.*
- [46] P. Harder, M. Grunze, R. Dahint, G. M. Whitesides, and P. E. Laibinis, J. Phys. Chem. B **102**, 426 (1998): *Molecular Conformation in Oligo(ethylene glycol)-Terminated Self-Assembled Monolayers on Gold and Silver Surfaces Determines Their Ability To Resist Protein Adsorption.*
- [47] M. W. A. Skoda, R. M. J. Jacobs, J. Willis, and F. Schreiber, Langmuir **23**, 970 (2007): *Hydration of Oligo(ethylene glycol) Self-Assembled Monolayers Studied Using Polarization Modulation Infrared Spectroscopy.*

-
- [48] D. K. Schwartz, *Annu. Rev. Phys. Chem.* **52**, 107 (2001): *Mechanisms and kinetics of self-assembled monolayer formation.*
- [49] R. K. Smith, P. A. Lewis, and P. S. Weiss, *Prog. Surf. Sci.* **75**, 1 (2004): *Patterning self-assembled monolayers.*
- [50] T. Wink, S. J. van Zuilen, A. Bult, and W. P. van Bennekom, *Analyst* **122**, 43R (1997): *Self-assembled Monolayers for Biosensors.*
- [51] M. Zharnikov and M. Grunze, *J. Phys. Condens. Matter* **13**, 11333 (2001): *Spectroscopic characterization of thiol-derived self-assembling monolayers.*
- [52] I. M. Tidswell, T. A. Rabedeau, P. S. Pershan, S. D. Kosowsky, J. P. Folkers, and G. M. Whitesides, *J. Chem. Phys.* **95**, 2854 (1991): *X-ray grazing incidence diffraction from alkylsiloxane monolayers on silicon wafers.*
- [53] S. I. Jeon, J. H. Lee, J. D. Andrade, and P. G. de Gennes, *J. Coll. Int. Sci.* **142**, 149 (1990): *Protein-Surface Interactions in the Presence of Polyethylene Oxide.*
- [54] K. Prime and G. Whitesides, *Science* **252**, 1164 (1991): *Self-assembled organic monolayers: model systems for studying adsorption of proteins at surfaces.*
- [55] K. L. Prime and G. M. Whitesides, *J. Am. Chem. Soc.* **115**, 10714 (1993): *Adsorption of proteins onto surfaces containing end-attached oligo(ethylene oxide): a model system using self-assembled monolayers.*
- [56] J. Lahiri, L. Isaacs, J. Tien, and G. M. Whitesides, *Anal. Chem.* **71**, 777 (1999): *A Strategy for the Generation of Surfaces Presenting Ligands for Studies of Binding Based on an Active Ester as a Common Reactive Intermediate: A Surface Plasmon Resonance Study.*
- [57] A. J. Pertsin, M. Grunze, and I. A. Garbuzova, *J. Phys. Chem. B* **102**, 4918 (1998): *Low-Energy Configurations of Methoxy Triethylene Glycol Terminated Alkanethiol Self-Assembled Monolayers and Their Relevance to Protein Adsorption.*
- [58] M. W. A. Skoda, F. Schreiber, R. M. J. Jacobs, J. R. P. Webster, M. Wolff, R. Dahint, D. Schwendel, and M. Grunze, *Langmuir* **25**, 4056 (2009): *Protein Density Profile at the Interface of Water with Oligo(ethylene glycol) Self-Assembled Monolayers.*
- [59] M. Yu, H. Ascolani, G. Zampieri, D. P. Woodruff, C. J. Satterley, R. G. Jones, and V. R. Dhanak, *J. Phys. Chem. C* **111**, 10904 (2007): *The Structure of Atomic Sulfur Phases on Au(111).*
- [60] N. Camillone, C. E. D. Chidsey, G. Yu Liu, and G. Scoles, *J. Chem. Phys.* **98**, 3503 (1993): *Superlattice structure at the surface of a monolayer of octadecanethiol self-assembled on Au(111).*

- [61] E. Delamarche, B. Michel, C. Gerber, D. Anselmetti, H.-J. Guentherodt, H. Wolf, and H. Ringsdorf, *Langmuir* **10**, 2869 (1994): *Real-Space Observation of Nanoscale Molecular Domains in Self-Assembled Monolayers*.
- [62] R. G. Nuzzo, L. H. Dubois, and D. L. Allara, *J. Am. Chem. Soc.* **112**, 558 (1990): *Fundamental studies of microscopic wetting on organic surfaces. 1. Formation and structural characterization of a self-consistent series of polyfunctional organic monolayers*.
- [63] P. Fenter, P. Eisenberger, and K. S. Liang, *Phys. Rev. Lett.* **70**, 2447 (1993): *Chain-length dependence of the structures and phases of $CH_3(CH_2)_{n-1}SH$ self-assembled on Au(111)*.
- [64] S. White and W. Wimley, *Biochim. Biophys. Acta, Biomembr.* **1376**, 339 (1998): *Hydrophobic interactions of peptides with membrane interfaces*.
- [65] M. K. Skinner, *Endocr. Rev.* **12**, 45 (1991): *Cell-Cell Interactions in the Testis*.
- [66] C. M. Roth and A. M. Lenhoff, *Langmuir* **9**, 962 (1993): *Electrostatic and van der Waals contributions to protein adsorption: computation of equilibrium constants*.
- [67] C. M. Roth, B. L. Neal, and A. M. Lenhoff, *Biophys. J.* **70(2)**, 977 (1996): *Van der Waals interactions involving proteins*.
- [68] R. A. Latour, in *Encyclopedia of biomaterials and biomedical engineering*, edited by G. L. Bowlin (2005).
- [69] E. Alm and D. Baker, *PNAS* **96**, 11305 (1999): *Prediction of protein-folding mechanisms from free-energy landscapes derived from native structures*.
- [70] V. Zamlynyy, Ph.D. thesis, University of Guelph, Canada, 2002.
- [71] R. Heeb, S. Lee, N. V. Venkataraman, and N. D. Spencer, *ACS Appl. Mater. Interfaces* **1**, 1105 (2009): *Influence of Salt on the Aqueous Lubrication Properties of End-Grafted, Ethylene Glycol-Based Self-Assembled Monolayers*.
- [72] J. Als-Nielsen and D. McMorrow, *Elements of modern X-ray physics* (2000).
- [73] L. G. Parratt, *Phys. Rev.* **95**, 359 (1954): *Surface studies of solids by total reflection of X-rays*.
- [74] Parratt32, Version 1.5.2: www.hmi.de/bensc/instrumentation/instrumente/v6/refl/parratt_en.htm.
- [75] D. Spanjaard and M. C. Desjonqueres, *Concepts in Surface Physics* (1996).
- [76] R. Feidenhans'l, *Surf. Sci. Rep.* **10**, 105 (1989): *Surface structure determination by X-ray diffraction*.

-
- [77] R. M. A. Azzam and N. M. Bashara, *Ellipsometry and polarized light* (1977).
- [78] J. A. W. Co., *WVASE32 Manual*.
- [79] U. Heinemeyer, Ph.D. thesis, Tübingen, 2009.
- [80] S. Busche, Ph.D. thesis, Tübingen, 2005.
- [81] U. Albrecht, Ph.D. thesis, Konstanz, 1992.
- [82] H. Räter, *Surface Plasmons on Smooth and Rough Surfaces and on Gratings* (1988).
- [83] D. B. Williams and C. B. Carter, *Transmission Electron Microscopy: A Textbook for Materials Science* (1996).
- [84] L. Reimer and H. Kohl, *Transmission Electron Microscopy: Physics of Image Microscopy: Physics of Image Formation* (2008).
- [85] S. Hüfner, *Photoelectron Spectroscopy: Principles and Applications* (1995).
- [86] M. Born and E. Wolf, *Principles of Optics: Electromagnetic Theory of Propagation, Interference and Diffraction of Light* (1997).
- [87] F. Abeles, *Ann. Phys.* **5**, 596 (1950).
- [88] F. Abeles, *Advanced Optical Techniques* (1967).
- [89] R. M. Corn, <http://corninfo.ps.uci.edu/writings/Ref4txt.html> .
- [90] C. G. Hu, L. D. Sun, Y. N. Li, M. Hohage, J. M. Flores-Camacho, X. T. Hu, and P. Zeppenfeld, *J. Opt. Soc. Am. A* **25**, 1240 (2008): *Retardation correction for photoelastic modulator-based multichannel reflectance difference spectroscopy*.
- [91] J. E. Bertie, M. K. Ahmed, and H. H. Eysel, *J. Phys. Chem.* **93**, 2210 (1989): *Infrared Intensities of Liquids. 5. Optical and Dielectric Constants, Integrated Intensities, and Dipole Moment Derivatives of H₂O and D₂O at 22 °C*.
- [92] I. H. Malitson, *J. Opt. Soc. Am.* **54**, 628 (1964): *Refractive Properties of Barium Fluoride*.
- [93] *Handbook of optical constants of solids*, edited by E. Palik (1985).
- [94] *CRC Handbook of Chemistry and Physics*, 87th ed., edited by D. Lide (2006).
- [95] I. Zawisza, G. Wittstock, R. Boukherroub, and S. Szunerits, *Langmuir* **23**, 9303 (2007): *PM IRRAS investigation of thin silica films deposited on gold. Part 1. Theory and proof of concept*.

- [96] L. A. J. Garvie, A. J. Craven, and R. Brydson, *Am. Mineral.* **79**, 411 (1994): *Use of Electron-Energy-Loss near-Edge Fine-Structure in the Study of Minerals*, .
- [97] L. A. J. Garvie and P. R. Buseck, *Am. Mineral.* **84**, 946 (1999): *Bonding in silicates: Investigation of the Si L-2,L-3 edge by parallel electron energy-loss spectroscopy*, .
- [98] J. Moulder, W. Stickle, P. Sobol, and K. Bomben, *Handbook of X-ray photoelectron spectroscopy* (1992).
- [99] H. Ebel, M. F. Ebel, R. Svagera, and A. Hofmann, *Surf. Interface Anal.* **18**, 821 (1992): *An Electron Spectroscopic Investigation of Attenuation Lengths of Electrons in SiO₂ in the Energy-Range 450 Ev Less-Than-or-Equal-to E_{kin} Less-Than-or-Equal-to 3100 Ev*, .
- [100] J. Bluemmel, N. Perschmann, D. Aydin, J. Drinjakovic, T. Surrey, M. Lopez-Garcia, H. Kessler, and J. P. Spatz, *Biomaterials* **28**, 4739 (2007): *Protein repellent properties of covalently attached PEG coatings on nanostructured SiO₂-based interfaces*.
- [101] A. A. Brown, N. S. Khan, L. Steinbock, and W. T. S. Huck, *Eur. Polym. J.* **41**, 1757 (2005): *Synthesis of oligo(ethylene glycol) methacrylate polymer brushes*, .
- [102] S. Sharma and T. A. Desai, *J. Nanosci. Nanotechnol.* **5**, 235 (2005): *Nanostructured antifouling poly(ethylene glycol) films for silicon-based microsystems*, .
- [103] A. Papra, A. Bernard, D. Juncker, N. B. Larsen, B. Michel, and E. Delamarche, *Langmuir* **17**, 4090 (2001): *Microfluidic networks made of poly(dimethylsiloxane), Si, and Au coated with polyethylene glycol for patterning proteins onto surfaces*, .
- [104] D. E. Hyre, I. Le Trong, E. A. Merritt, J. F. Eccleston, N. M. Green, R. E. Stenkamp, and P. S. Stayton, *Protein Sci.* **15**, 459 (2006): *Cooperative hydrogen bond interactions in the streptavidin-biotin system*, .
- [105] S. W. Metzger, M. Natesan, C. Yanavich, J. Schneider, and G. U. Lee, *J. Vac. Sci. Technol. A* **17**, 2623 (1999): *Development and characterization of surface chemistries for microfabricated biosensors*, .
- [106] N. P. Huang, J. Voros, S. M. De Paul, M. Textor, and N. D. Spencer, *Langmuir* **18**, 220 (2002): *Biotin-derivatized poly(L-lysine)-g-poly(ethylene glycol): A novel polymeric interface for bioaffinity sensing*, .
- [107] R. Gunawan, J. King, B. Lee, P. Messersmith, and W. Miller, *Langmuir* **23**, 10635 (2007): *Surface presentation of bioactive ligands in a nonadhesive background using DOPA-tethered biotinylated poly(ethylene glycol)*.
- [108] Y. H. Jang, S. Y. Oh, and J. K. Park, *Enzyme Microb. Technol.* **39**, 1122 (2006): *In situ electrochemical enzyme immunoassay on a microchip with surface-functionalized poly(dimethylsiloxane) channel*, .

-
- [109] T. Miyazawa, K. Fukushima, and Y. Ideguchi, *J. Chem. Phys.* **37**, 2764 (1962): *Molecular Vibrations and Structure of High Polymers. III. Polarized Infrared Spectra, Normal Vibrations, and Helical Conformation of Polyethylene Glycol.*
- [110] S. J. McClellan and E. I. Franses, *Colloids Surf. A* **260**, 265 (2005): *Adsorption of bovine serum albumin at solid/aqueous interfaces, .*
- [111] A. Barth and C. Zscherp, *Q. Rev. Biophys.* **35**, 369 (2002): *What vibrations tell about proteins.*
- [112] M. Kobayashi and M. Sakashita, *J. Chem. Phys.* **96**, 748 (1992): *Morphology dependent anomalous frequency shifts of infrared absorption bands of polymer crystals: Interpretation in terms of transition dipole–dipole coupling theory.*
- [113] L. Malysheva, Y. Klymenko, A. Onipko, R. Valiokas, and B. Liedberg, *Chem. Phys. Lett.* **370**, 451 (2003): *Ab initio calculations of equilibrium geometries and vibrational excitations of helical ethylene-glycol oligomers: application to modeling of monolayer infrared spectra.*
- [114] L. Malysheva, A. Onipko, R. Valiokas, and B. Liedberg, *Appl. Surf. Sci.* **246**, 372 (2005): *First-principles modeling of oligo(ethylene glycol)-terminated and amide group containing alkanethiolates, .*
- [115] M.-T. Lee, C.-C. Hsueh, M. S. Freund, and G. S. Ferguson, *Langmuir* **14**, 6419 (1998): *Air Oxidation of Self-Assembled Monolayers on Polycrystalline Gold: The Role of the Gold Substrate.*
- [116] M. Cerruti, S. Fissolo, C. Carraro, C. Ricciardi, A. Majumdar, and R. Maboudian, *Langmuir* **24**, 10646 (2008): *Poly(ethylene glycol) Monolayer Formation and Stability on Gold and Silicon Nitride Substrates.*
- [117] H. M. Zareie, C. Boyer, V. Bulmus, E. Nateghi, and T. P. Davis, *ACS Nano* **2**, 757 (2008): *Temperature-Responsive Self-Assembled Monolayers of Oligo(ethylene glycol): Control of Biomolecular Recognition.*
- [118] J. B. Schlenoff, M. Li, and H. Ly, *J. Am. Chem. Soc.* **117**, 12528 (1995): *Stability and Self-Exchange in Alkanethiol Monolayers.*
- [119] J. R. Vig, *J. Vac. Sci. Technol., A* **3**, 1027 (1985): *UV/ozone cleaning of surfaces.*
- [120] Y. Zhang, R. H. Terrill, and P. W. Bohn, *Chem. Mater.* **11**, 2191 (1999): *Ultraviolet Photochemistry and ex Situ Ozonolysis of Alkanethiol Self-Assembled Monolayers on Gold.*
- [121] H. Günzler and H.-U. Gremlich, *IR Spectroscopy: An Introduction* (2002).

- [122] K. Kurita, J. Amemiya, T. Mori, and Y. Nishiyama, *Polym. Bull.* **42**, 387 (1999): *Comb-shaped chitosan derivatives having oligo(ethylene glycol) side chains.*
- [123] S. Balamurugan, L. K. Ista, J. Yan, G. P. Lopez, J. Fick, M. Himmelhaus, and M. Grunze, *J. Am. Chem. Soc.* **127**, 14548 (2005): *Reversible Protein Adsorption and Bioadhesion on Monolayers Terminated with Mixtures of Oligo(ethylene glycol) and Methyl Groups.*
- [124] A. Rosenhahn, S. Schilp, H. J. Kreuzer, and M. Grunze, *Phys. Chem. Chem. Phys.* **12**, 4275 (2010): *The role of "inert" surface chemistry in marine biofouling prevention.*
- [125] A. R. Sandy, S. G. J. Mochrie, D. M. Zehner, K. G. Huang, and D. Gibbs, *Phys. Rev. B* **43**, 4667 (1991): *Structure and phases of the Au(111) surface: X-ray-scattering measurements.*
- [126] P. E. Laibinis, C. D. Bain, R. G. Nuzzo, and G. M. Whitesides, *J. Phys. Chem.* **99**, 7663 (1995): *Structure and Wetting Properties of .omega.-Alkoxy-n-alkanethiolate Monolayers on Gold and Silver.*
- [127] D. J. Vanderah, R. S. Gates, V. Silin, D. N. Zeiger, J. T. Woodward, C. W. Meuse, G. Valincius, and B. Nickel, *Langmuir* **19**, 2612 (2003): *Isostructural Self-Assembled Monolayers. 1. Octadecyl 1-Thiaoligo(ethylene oxides).*
- [128] F. Schreiber, A. Eberhardt, T. Y. B. Leung, P. Schwartz, S. M. Wetterer, D. J. Lavrich, L. Berman, P. Fenter, P. Eisenberger, and G. Scoles, *Phys. Rev. B* **57**, 12476 (1998): *Adsorption mechanisms, structures, and growth regimes of an archetypal self-assembling system: Decanethiol on Au(111).*

List of publications

- 12. S. Zorn, et. al. Longtime stability of C₁₁EG₆OMe SAMs as a function of light exposure, temperature and immersion. In preparation
- 11. S. Zorn, M. Skoda, R. Jacobs, A. Gerlach, F. Schreiber. Conformational change of C₁₁EG₆OMe SAMs on gold at elevated temperature under aqueous conditions. In preparation
- 10. S. Zorn, N. Martin, A. Gerlach, F. Schreiber. Real-time PMIRRAS studies of in situ growth of C₁₁EG₆OMe on gold and immersion effects. *Phys. Chem. Chem. Phys.*, 2010, 12, 8985 - 8990
- 9. F. Roosen-Runge, M. Hennig, T. Seydel, F. Zhang, M.W.A. Skoda, S. Zorn, R.M.J. Jacobs, M. Maccarini, P. Fouquet and F. Schreiber. Protein diffusion in crowded electrolyte solutions. *Biochimica et Biophysica Acta - Proteins & Proteomics* 1804 (2010), Issue 1, 68
- 8. M. Skoda, R. Jacobs, S. Zorn, and F. Schreiber. Optimizing the PMIRRAS signal from a multilayer system and application to self-assembled monolayers in contact with liquids. *J. Electron. Spec. Rel. Phen* 172 (2009) 21
- 7. I. E. Dunlop, S. Zorn, G. Richter, V. Srot, M. Kelsch, P. Van Aken, M. Skoda, A. Gerlach, J. Spatz, and F. Schreiber. Titanium-silicon oxide film structures for polarization-modulated infrared reflection absorption spectroscopy. *Thin Solid Films* 517 (2009) 2048
- 6. F. Zhang, M. W. A. Skoda, R. M. J. Jacobs, S. Zorn, R. A. Martin, C. M. Martin, G. F. Clark, S. Weggler, A. Hildebrandt, O. Kohlbacher, and F. Schreiber. Reentrant condensation of proteins in solution induced by multivalent counterions. *Phys. Rev. Lett.* 101 (2008) 148101
- 5. J. Mehne, G. Markovic, F. Pröll, N. Schweizer, S. Zorn, F. Schreiber, and G. Gauglitz. Characterization of morphology of self assembled PEG monolayers: A comparison of mixed and pure coatings optimized for biosensor applications. *Anal. Bioanal. Chem.* 391 (2008) 1783

- 4. F. Zhang, D. G. Dressen, M. W. A. Skoda, R. M. J. Jacobs, S. Zorn, R. A. Martin, C. M. Martin, G. F. Clark, and F. Schreiber. Gold nanoparticles decorated with oligo (ethylene glycol) thiols: Kinetics of colloid aggregation driven by depletion forces. *Eur. Biophys. J.* 37 (2008) 551
- 3. F. Zhang, M. W. A. Skoda, R. M. J. Jacobs, S. Zorn, R. A. Martin, C. M. Martin, G. F. Clark, G. Goerigk, and F. Schreiber. Gold nanoparticles decorated with oligo (ethylene glycol) thiols: protein resistance and colloidal stability. *J. Phys. Chem. A* 111 (2007) 12229
- 2. E. Leipold, H. DeBie, S. Zorn, B. Adolfo, B. M. Olivera, H. Terlau and S. H. Heinemann. μ O-Conotoxins Inhibit NaV Channels by Interfering with their Voltage Sensors in Domain-2. *Channels* 1 (2007), Issue 4 253
- 1. S. Zorn, E. Leipold, A. Hansel, G. Bulaj, B.M. Olivera, H. Terlau and S.H. Heinemann. The μ O-conotoxin MrVIA inhibits voltage-gated sodium channels by associating with domain-3. *FEBS Lett* 580 (2006) 1360-4.

Danksagung

Diese Arbeit wäre ohne die vielen Menschen, die mich dabei unterstützt haben nicht möglich gewesen.

Mein besonderer Dank gilt Prof. Dr. Frank Schreiber für das interessante Thema dieser Arbeit und die Einbindung in ein spannendes wissenschaftliches Umfeld. Ich erinnere mich immer wieder gern an seine erfrischenden Tutorials. Ich danke ihm für das stete Interesse an meiner Arbeit, vor allem für das Vertrauen und die Geduld, die er mir entgegenbrachte.

Prof. Dr. Günter Gauglitz möchte ich für die Begutachtung meiner Arbeit danken und für die gute wissenschaftliche Zusammenarbeit mit seiner Arbeitsgruppe.

Mein großer Dank gilt meinem Betreuer Dr. Alexander Gerlach, ohne ihn und seine stete Unterstützung wäre vieles nicht möglich gewesen.

Mein Dank gilt auch Dr. Iain Dunlop, der mich mit seiner Begeisterung immer wieder ansteckte und mit dem kein Experiment langweilig wurde. Ebenfalls möchte ich Dr. Maximilian Skoda danken für die kurzweiligen Schichten während zahlreicher Experimente und seine Unterstützung bei vielen Fragestellungen dieser Arbeit.

Dr. Robert Jacobs, Dr. Fajun Zhang und Felix Roosen-Runge danke ich für die gute Zusammenarbeit in zahlreichen Projekten und für die unzähligen fachlichen Diskussionen, die maßgeblich zum Gelingen dieser Arbeit beitrugen.

Ein großer Dank gilt auch Dr. Stefanie Jäger und Nina Schweizer für die gute Zusammenarbeit und die vielen lustigen Gespräche.

Weiterhin danke ich allen Mitgliedern der Arbeitsgruppe Schreiber und dem Sekretariat für den freundlichen kollegialen Umgang und die fachliche Unterstützung. Ich danke meinen studentischen Mitarbeitern Alexander Müller, Mirco Zachmann und Dominik Vogel für die gute Zusammenarbeit und ihre interessanten Fragen. Ganz besonders danke ich auch meinen Austauschstudenten Nathan Martin und Donald Dressen, die mich im Rahmen des RISE-Programmes unterstützten und mit ihrer Forschungsarbeit wichtige Grundsteine für diese Arbeit legten.

Nicht zuletzt möchte ich mich auch bei den Mitarbeitern der feinmechanischen Werkstatt und der Elektronikwerkstatt bedanken. Mein besonderer Dank gilt hier Frau Antje Treftz, die durch ihre tolle Unterstützung und ihre guten Ideen viele Experimente erst ermöglicht hat.

Ich danke Herrn Klaus Hagdorn für die vielen kleinen Dinge mit denen er mich immer wieder unterstützt hat und für die vielen interessanten Gespräche rund um das Leben außerhalb der Wissenschaft.

Ein herzlicher Dank gilt meinen Freunden, die mir immer wieder Kraft und Freude gaben, danke André, Matze, Thomas, Johanna, Astrid, Verena, Daniel, Carsten, Oliver, Sabine und danke an viele andere, die hier nicht alle genannt werden können.

Meiner Freundin Nora danke ich für ihren Zuspruch, ihr Verständnis und viele schöne Stunden auf der Tanzfläche.

Mein größter Dank gilt meinen Eltern, sie haben sich mit mir gefreut und mitgelitten, ihre große Liebe hat mich auf all meinen Wegen begleitet und mir Kraft gegeben. Ich möchte ihnen diese Arbeit widmen. Danke für Alles!

Curriculum vitae

Stefan Zorn

born on the 3rd of May 1981 in Plauen

Since 08 / 2006 Ph.D studies at the Eberhard Karls University of Tübingen, Institute of applied physics. Supervisor: Prof. Dr. Frank Schreiber Title of thesis: “*In-situ* studies of protein-resistant self-assembling monolayers”

09 / 2000 - 05 / 2006 Diploma in Physics, Friedrich Schiller University Jena, Center for molecular biomedicine. Supervisor: Prof. Dr. Stefan H. Heinemann Title of thesis: “Interaction of voltage dependent ion channels with Neurotoxins”

